Highly stable laser for space gravitational wave detector: DECIGO

Ph.D Thesis

Aru Suemasa

March 9, 2019

UNIVERSITY OF ELECTRO-COMMUNICATIONS
GRADUATE SCHOOL OF INFORMATICS AND ENGINEERING
DEPARTMENT OF ENGINEERING SCIENCE

Acknowledgments

First of all, I would like to thank to my supervisor associate Prof. Dr. Mitsuru Musha for his enormous amount of support. I have received his instruction for more than 6 years.
Another special acknowledge goes to Prof. Ken ' ichi Nakagawa and Prof. Hitoki Yoneda for giving me a fruitful science and technical suggestions and advices.
And I show special thanks to Prof. Masaki Ando, Univ. of Tokyo for discussion about gravitational wave detection.
I would like to thank my following colleagues, Eiji Kajikawa, Yurina Michine, Shotaro Kitajima. They have spent doctor course with me.
For promoting my study, I collaborate with Ayumi Shimo-oku and Shunsuke Otsuka who help me for the experiments and discussions.
The time I spent with them in the laboratory would be my lifetime treasure.
I Thank the Japan Society for the Promotion of Science for giving me a financial support.
I immensely grateful to my mother and farther. They always supported me, believed my success and never let me give up. Without them not being what I am now.

Ph.D publication list

Journal publications

1. Aru Suemasa, Ayumi Shimo-oku, Ken'ichi Nakagawa, Mitsuru Musha 「Developments of high frequency and intensity stabilized lasers for space gravitational wave detector DECIGO/B-DECIGO」 CEAS Space Journal, vol.9 pp.485-491(2017)

Conference contributions

International conferences

1. Aru Suemasa, Ayumi Shimo-oku, Mitsuru Musha, DECIGO working group " Developments of highly-stabilized lasers for DECIGO/Pre-DECIGO " 11th International LISA symposium, p-24,), ETH Zurich, Zurich, Switzerland, Sep 5, 2016

2. Aru Suemasa, Ayumi Shimo-oku, Ken'ichi Nakagawa, Mitsuru Musha ' Developments of highly frequency and intensity stabilized lasers for gravitational wave detector DECIGO/B-DECIGO ' International Conference on Space Optics (ICSO) 2016, 2c-35, Biarritz, France, Oct 18, 2016

3. Aru Suemasa, Mitsuru Musha " Highly stabilized lasers for space gravitational wave detector " CIAiS International Symposium,10, Tokyo University, Tokyo, Japan, Feb 7, 2017

4. Aru Suemasa, Ayumi Shimo-oku, Mitsuru Musha " Developments of highly frequency and intensity stabilized lasers for space gravitational wave detector ", 4th MIPT-LPI-UEC Joint Workshop on Atomic, Molecular, Optical Physic, Univ. of Electro-Commun. Chofu, Japan, Mar 3, 2017

5. Aru Suemasa, Ayumi Shimo-oku, Ken'ichi Nakagawa, Mitsuru Musha "Developments of highly frequency and intensity stabilized lasers for gravitational wave detector DECIGO" CLEO Europe-EQEC 2017, CJ 12.5, Munich, Germany, June 6, 2017

6. Aru Suemasa, Shunsuke Ohtsuka, Ayumi Shimo-oku, Mitsuru Musha "Developments of the stable lasers for Gravitational Wave detector" CIAiS International Symposium, Tokyo University, Tokyo, Japan, May 8, 2018

7. Aru Suemasa, Shunsuke Ohtsuka, Ayumi Shimo-oku, Ken'ichi Nakagawa, Mitsuru Musha "Stable and high power lasers for the space gravitational wave detector DECIGO" International Conference on Space Optics (ICSO) 2018, 3c-3, Crete, Greece ,Oct 8, 2018

Domestic conferences

1. 下奥あゆ美、末正有、武者満 「宇宙重力波望遠鏡 (DECIGO) のための高出力・高安定光源の開発」第 60 回宇宙科学技術連合講演会,3J15, 函館アリーナ, 2016 年 09 月 8 日

2. 末正有、下奥あゆ美、中川賢一、武者満 「スペース重力波アンテナ DECIGO 計画 (75):安定化光源」日本物理学会 2016 年秋季大会,24aSR-10 宮崎大学, 2016 年 9 月 24 日

3. 末正有「DECIGO のための安定化光源」15th DECIGO Workshop, 京都大学, 2016 年 11 月 5 日

4. 下奥あゆ美、末正有、中川賢一、武者満 「スペース重力波アンテナ DECIGO 計画 (80):安定化光源」日本物理学会第 72 回年次大会, 18pK25-3, 大阪大学, 2017 年 3 月 18 日

5. 末正有、下奥あゆ美、中川賢一、武者満 「宇宙重力波検出器 DECIGO のための周波数・強度安定化光源の開発」第 78 回応用物理学会秋季学術講演会,5p-C14-1, 福岡国際会議場, 2017 年 9 月 5 日

6. 末正有、下奥あゆ美、中川賢一、武者満 「スペース重力波アンテナ DECIGO 計画 (85):安定化光源」日本物理学会 2017 年秋季大会, 宇都宮大学,14aU11-2, 2017 年 09 月 14 日

7. 赤見恵、末正有、武者満「スペース重力波アンテナ DECIGO 計画 (86): 音響光学素子を用いた衛星捕捉システムの開発」日本物理学会 2017 年秋季大会, 宇都宮大学,14aU11-3, 2017 年 9 月 14 日

8. 下奥あゆ美、末正有、武者満「宇宙重力波検出器 DECIGO/B-DECIGO のための高出力・高安定光源の開発」第 61 回宇宙科学技術連合講演会,1A06, 朱鷺メッセ, 2017 年 10 月 25 日

9. 赤見恵、末正有、武者満「音響光学偏向子を用いた衛星ポジショニングシステムの開発」第 61 回宇宙科学技術連合講演会, 1A12, 朱鷺メッセ, 2017 年 10 月 25 日

10. 下奥あゆ美、末正有、武者満、中川賢一「スペース重力波アンテナ DECIGO 計画 (92):安定化光源」日本物理学会第 73 回年次大会, 25aK308-10, 東京理科大学, 2018 年 3 月 25 日

11. 中森真輝、末正有、下奥あゆ美、大塚俊介、中川賢一、武者満「スペース重力波アンテナ DECIGO 計画 (95)：高出力・安定光源」日本物理学会 2018 年秋季大会, 信州大学, 2018 年 09 月 16 日

12. 赤見恵、末正有、武者満「スペース重力波アンテナ DECIGO 計画 (96)：音響光学偏向子を用いた衛星位置決定システムの開発」日本物理学会 2018 年秋季大会, 信州大学, 2018 年 9 月 16 日

13. 大塚俊介、末正有、赤見恵、中森真輝、下奥あゆ美、武者満「宇宙重力波検出器 DECIGO/B-DECIGO のための光源と光学技術の開発」第 62 回宇宙科学技術連合講演会、1G11、久留米シティプラザ、2018 年 10 月 24 日

Contents

1 Introduction **1**

2 Gravitational Wave detector **3**

2.1 Gravitational wave 3

2.2 Space gravitational wave detectors 4

2.2.1 DECIGO Pathfinder 4

2.2.2 DECIGO and B-DECIGO 6

2.2.3 Light source for space gravitational wave detector . . . 8

2.2.4 Light source for other space missions 13

3 Saturation spectroscopy of Iodine absorption line **16**

3.1 Signal detection 16

3.1.1 Saturated absorption spectroscopy 17

3.1.2 Frequency modulation spectroscopy 20

3.1.3 Modulation transfer spectroscopy 24

3.2 Selection of frequency reference 26

3.3 Linewidth broadening effect 28

3.3.1 Pressure broadening 28

3.3.2 Transit time broadening 29

3.4 Precision spectroscopy of iodine absorption lines 30

3.4.1 Pressure broadening of saturated absorption line 35

3.4.2 Selection of transition 38

3.4.3 The hyperfine structure of the iodine absorption line . 39

4 Development of iodine-stabilized lasers **43**

4.1 Concept of breadboard model 43

4.2 Experimental setup of BBM1 and BBM2 43

4.3 The performance of the frequency-stabilized laser 47

4.4 Evaluation of frequency stability 51

5 Improvement of the short-term frequency stability **55**

5.1 Intensity stabilization at modulation frequency of 200 kHz . . 55

5.1.1 Intensity stabilization at 200 kHz (normal feed back) . 56

5.1.2 Experimental result (normal feed back) 59
5.1.3 Intensity stabilization at 200 kHz (forced oscillation) . 60
5.1.4 Experimental result (self-oscillation) 60
5.1.5 Intensity stabilization at 200 kHz (feed forward) 63
5.1.6 Experimental result (feed forward) 66
5.2 Balanced detection 69
5.2.1 Experimental result of balanced detection 72

6 Intensity stabilization at observation band 74
6.1 Free-space experiment 77
6.2 Fiber components experiment 81

7 Further improvement of frequency stability 86

8 Conclusion 88

9 Future prospects 90

A The investigation of breadboards for BBM 92

B Servo circuit for the frequency stabilization 97

C Servo circuit for intensity stabilization at 200 kHz by using normal feedback 98

D Phase shifter of the feedforward servo for intensity stabilization at 200 kHz 99

E Electrical circuit of the auto-balanced detector 100

F Electric servo filter for the intensity stabilization of the laser at 1 Hz 101

List of Figures

2.1 Schematic of DPF and the specification of the satellite; left is the frequency-stabilized laser and the interferometer, right is the small satellite for DPF 5
2.2 Road map of the space GW detectors in Japan: the vertical axis indicates the two lower digits of the dominical year 6
2.3 Conceptual design of DECIGO. Triangle-shaped Fabry-Perot interferometer with the arm length of 1000 km. The left is the two overlapped units of DECIGO for improving the strain sensitivity by correlation observations. 7
2.4 Strain sensitivity of DECIGO and B-DECIGO, and that of science targets are also marked 9
2.5 Designed strain sensitivity of DECIGO (solid trace) at laser power of 10 W (blue) and 30 W (red). Dashed traces and dots indicate shot-noise limit and radiation pressure noise limit, respectively 14
3.1 Schematic of saturated absorption spectroscopy 17
3.2 Boltzmann distribution in the thermal equilibrium and absorption of molecules 18
3.3 Schematic of saturated absorption spectroscopy 18
3.4 Schematic of saturated absorption spectroscopy 19
3.5 (a)Saturated population distribution of lower and upper state with two counter-propagated beam, (b)Intensity of the transmitted laser beam through the molecular cell. At the center of the linear absorption, a narrow saturated absorption peak is appeared. 19
3.6 Experimental diagram of Frequency modulation spectroscopy . 21
3.7 System of four-wave mixing 25
3.8 Linear absorption signal (blue trace) and the saturated absorption signal (red trace) of iodine at 515 nm. It is shown that at the center of the linear absorption, the absorption is saturated and the saturated absorption signals become weak. . 31
3.9 Schematic diagram of precision spectroscopy system 32

3.10 Picture of the precision spectroscopy system 33
3.11 I_2-saturated absorption lines, the hyperfine components, a_{19}, a_{20}, a_{21} in the linear absorption line of P29(43-0) which is obtained from the I_2-cell-2 34
3.12 Iodine-absorption lines which are obtained from the frequency stabilization part and the signal acquisition part (I_2-cel-1 and I_2-cell-2), respectively 35
3.13 Pressure broadening of HWHM 36
3.14 1^{st} derivative of absorption line at 1Pa 37
3.15 1^{st} derivative of absorption line. The temperature in the I_2 cell is changed between -15 °C and 15 °C 38
3.16 Linear absorption lines and saturated absorption lines 40
3.17 Linear absorption line of P29(43-0) and P79(53-1) near 515.0291 nm, and 42-saturated absorption lines. 41
3.18 Linear absorption signal of R72(45-0), and 15-saturated absorption lines. 42
4.1 Schematic of BBM 45
4.2 BBM1 (first model of BBM) 46
4.3 BBM2(Improved BBM) 47
4.4 Schematic diagram for measurement of the open loop AG . . 48
4.5 Measured total open loop transfer function T_{total} 48
4.6 Simulated and measured total open loop transfer function Ttota (red: gain-left, blue: phase-right), measured (solid traces) and simulated by using equivalent circuit (dotted traces). . . . 49
4.7 Frequency spectra evaluated from the error signal; the blue trace and the red trace indicate the frequency noise at free-running state and at the stabilized state, respectively. (the left is BBM1, the right is BBM2). 50
4.8 Schematic of the absolute frequency evaluation 51
4.9 Allan-deviation of 40-MHz beat note between two lasers at free-running state (green dots), at stabilized state measured in March 2017 (blue dots) and September 2017 (red dots). . . 52
4.10 Allan deviation of the beat note frequency 53

4.11 Absolute frequency noise spectrum of the frequency-stabilized laser which is evaluated from the beat note between two stabilized lasers, which reaches 50 Hz/$\sqrt{}$ Hz below 500 Hz. 54
4.12 Frequency noise level from the noise of the signal which is converted from the intensity noise of the frequency discrimination signal [red]. Black trace indicates the in-loop frequency noise spectrum, and the absolute frequency noise [Fig.4.11] is sum of the SNR and residual frequency noise of the laser. 54
5.1 RIN of the fiber DFB laser, ECLD1 and ECLD2 55
5.2 Schematic diagram of the active intensity stabilization by using feedback method. AOM driver consist of a voltage-controlled actuator and a power amplifier, and the output power can be controlled by using the applied control signal 57
5.3 Transfer function of the AOM diver and voltage control attenuators (VCATT). Compared with VCATT, the AOM driver shows less phase delay at 200 kHz. 58
5.4 Transfer function of the operational amplifier (OP27, AD829) 58
5.5 RIN of the signal beam at the free-running state (blue) and the stabilized state (red) 59
5.6 Schematic of the intensity stabilization at 200 kHz by using low noise amplifier (LNA) 60
5.7 RIN spectrum; the blue and the red lines indicate the stabilized state and free-running state, respectively. At 800 kHz the servo system is oscillated, and the intensity noise suppression around this oscillation peak is observed. 61
5.8 Demodulated RIN spectrum; the blue and the red lines indicate the stabilized state and free-running state, respectively. . 62
5.9 Schematic diagram of intensity stabilization at 200 kHz by feed forward method 63
5.10 Transfer function of the two stage phase shifter 64

5.11 Measured open loop transfer function of our hand-made phase shifter. The solid and dashed traces indicate gain and phase, respectively, and blue lines represent those of 1 phase shifter, and red lines represent those of 2-stage phase shifter. Red bar indicates the frequency at 200 kHz. 65
5.12 Intensity noise spectra of the laser at feed forward control; free running (black), and feed forward controlled as the shifted phase is increasing (green to blue), and at the appropriate phase (red), RIN at 200 kHz (red bar) is narrowly suppressed by mode than 15 dB. 66
5.13 Intensity noise spectra in the demodulated frequency discrimination signal; blue and red indicate the intensity noise at the free-running and the stabilized state, respectively. 67
5.14 Expanded frequency discrimination signals at free-running state (yellow trace) Blue trace indicates the applied voltage to the PZT terminal of the laser. 68
5.15 Expanded frequency discrimination signals at stabilized state . 68
5.16 Schematic of the passive intensity noise cancellation system . . 69
5.17 Intensity noise spectrum obtained from the auto-balanced PD with various local powers. As the local power increases (V_{mon} decreases), the noise suppression ratio increases up to 25 dB. . 70
5.18 Noise spectrum from the auto-balanced PD without local beam (black trace), local in with off resonance (blur trace), and local in with on resonance (red trace) 71
5.19 Demodulated signal from the single PD (blue) and from the auto-balanced PD 72
5.20 Frequency noise of the beat signal between two BBMs. By using the auto-balanced detector (red trace) the frequency noise is improved from the single PD detection (blue) 73
6.1 Schematic diagram of our intensity-stabilization system at the observation band around 1 Hz. 74
6.2 Transfer function of A (red: gain-left, blue: phase-right), measured (solid traces) and simulated by using equivalent circuit (dotted traces) 76

6.3 Total open loop transfer function $T_{open} = AG$ 77
6.4 Experimental set up of the free-space intensity-stabilization by using NBS 78
6.5 Intensity spectra of RIN at free-running state (blue trace), at the stabilized state evaluated from in-loop (green trace) and from out-of-loop (red trace) 78
6.6 Polarization dependency of NBS (originated from the datasheet of Thorlab Inc 79
6.7 Tilting the incident angle of NBS to have equal reflectance for both p and s polarized light 80
6.8 Out-of-loop RIN at free-space experiment ; red line: before improving , purple line: improved by tilting NBS 80
6.9 Schematic of the intensity stabilization by using a 3-dB fiber coupler 81
6.10 Picture of the intensity stabilization by using a 3-dB fiber coupler 82
6.11 RIN spectra obtained from fiber components experiments; the black line indicates the RIN evaluated from in-loop, the red line indicates that evaluated from out-of-loop (not fixed), the blue line indicates that evaluated from out-of-loop (fixed by epoxy), the dashed purple line indicates the stability of the voltage reference (LTC6655) 83
6.12 Schematic of the experimental setup which is covered by a polystyrene box, and a 5 kg-aluminum board is put as a weight on the box. 84
6.13 Improved RIN spectra obtained from the fiber components experiments. The blue line: the RIN evaluated from the in-loop, the red line: the RIN evaluated from out-of-loop whose experimental setup is covered by the box, and whose voltage reference is replaced to more stable reference. 85
7.1 Experimental setup for the combination of FM and MT 86
7.2 Frequency discrimination signals obtained from MT technic and FM technic which are detected synchronously 87
A.1 Aluminum breadboard 92
A.2 Carbon breadboard 92

A.3 Experimental setup of the asymmetric Michelson interferometer 93
A.4 Temporal variations of the interference fringe (aluminum breadboard) 93
A.5 Temporal variations of the interference fringe (carbon breadboard) 93
A.6 Experimental setup of the asymmetric Michelson interferometer heated by the ribbon heater 94
A.7 Thermal variations of the interference fringe (aluminum breadboard) 95
A.8 Thermal variations of the interference fringe (carbon breadboard) 96
E.1 Electrical circuit of the auto-balanced detector 100
E.2 The picture of the auto-balanced detector 100

List of Tables

1 Requirements for the light sourced of DPF and DECIGO . . . 5
2 Main parameter of DECIGO and B-DECIGO 7
3 Requirements of the light source for DECIGO and B-DECIGO 8
4 Carbon and aluminum breadboards 92

1 Introduction

Since the lasers have high temporal and spatial coherence, they have been widely used in many fields such as material processing, spectroscopy, length measurement or optical communications. For the precise spectroscopy or frequency standards, further frequency stabilization of the lasers have been studied whose frequencies are stabilized in reference to a resonance of the Fabry-Perot cavity or an absorption line of the molecules, atoms and ions at various frequencies, such as the iodine-stabilized He-Ne lasers at 633 nm [1][2], the acetylene-stabilized laser diode at 1543 nm [3] or the iodine-stabilized Nd:YAG laser at 1064 nm [4],[5],[6]. Especially, Fabry-Perot-stabilized lasers reache the short-term frequency stability of $df/f = 10^{-17}$ levels [7], and also Strontium optical lattice clock reaches $df/f = 10^{-18}$ levels [8]. Ultra-high frequency-stabilized lasers make it possible to verify fundamental physics such as temporal variation of fundamental constant [9], violation of Lorentz invariance [10] or detection of gravitational-wave (GW) [11]. In recent years, frequency-stabilized lasers are required in many space projects; not only for the laser ranging, but also spectroscopy, remote sensing, the optical communications, highly stable frequency reference, the precision measurement in space and so on.

In our laboratory to which I belong from the undergraduate student, the frequency-stabilized lasers and its applications have been studied, and the highly stable and high power light sources for Japanese GW detector have been developed [12][13][14] since the Japanese prototype GW detector: TAMA 300 [15]. Currently, besides construction of a terrestrial GW detector named KAGRA [16], Japan has also promoted a space GW detector named DECIGO [17], and I have devoted myself into the development of the light source for DECIGO. In my doctor thesis, developments of space-borne frequency- and intensity-stabilized lasers for DECIGO are reported. As a space-borne stabilized laser, I have developed two breadboard models (BBM1, BBM2) whose frequency is stabilized in reference to the hyperfine structure of the iodine saturated absorption line at 515 nm. Since the linewidth of the iodine saturated absorption line at 515 nm is narrower than that at 532 nm, higher short-term frequency stability is expected. I have evaluated the absolute

frequency stability of the lasers from the beat note between two BBMs. In order to improve the short-term frequency stability, the intensity noise at modulation frequency (200 kHz) is suppressed by active and passive noise reduction method. We also try intensity stabilization at observation band of DECIGO at around 1 Hz by two methods, and the intensity noise is successfully suppressed. For space-borne laser, the consumption power, the robustness and the tolerance against cosmic ray exposure are considered. In DECIGO project, the observation band is from 0.1 to 1 Hz which is much lower than that of the terrestrial gravitational wave detectors, and for the light source, highly frequency and intensity stabilities in this frequency band are required. Usually, for obtaining high short-term frequency stability around 1 Hz, optical resonance of a Fabry-Perot cavity is utilized as the frequency reference because it shows higher frequency stability than that of the molecular absorption line. I dare to use the absorption line of the iodine molecules as a frequency reference for obtaining frequency stability around 1 Hz, in the reasons that DECIGO also requires the long-term frequency stability to the light source for the reference of the arm length and it shows higher robustness than Fabry-Perot cavity. I try to obtain short-term frequency stability from using the iodine molecules, which no one has ever tried.

2 Gravitational Wave detector

2.1 Gravitational wave

Gravitational-wave (GW), which has been predicted by A. Einstein in his general theory of relativity [18], is slight temporal variation of space distortions which propagates as a transvers wave at the speed of light. It have been predicted that GW would be generated from the anti-symmetric enormous mass motions such as inspiral and merger of neutron star binaries or black hole binaries, explosion of supernovae, and inflation in early universe. However, the expected strain of GW is extremely small as low as $dL/L < 10^{-23}$ even from the merger of heavy black-hole binaries, and no one had imagine of direct detection of GW. Since GW is tidal force to the free masses, the direct detection of GW by using a long-baseline laser interferometer had been proposed in 1980s [19], and from 1990, many research institutes around the world have tried to observe GW directly by using large-scale laser interferometers, such as LIGO in US [20] , VIRGO in Italy [21], GEO600 in Germany [22], TENKO100 [23] and TAMA300 in Japan [15]. And, after a long struggle for improving the strain sensitivity of the detectors, the first direct observation of GW has been achieved by Adv.LIGO team in 2015 [24] which is generated from the inspiral and merger of black-hole binaries with the mass of 30 $M_{\odot}$ ($M_{\odot}$: Solar Mass). The establishment of new GW astronomy has been just kicked off, which will give us much information from those obtained by the conventional elector-magnetic wave observations. Followed by the first direct detection of GW called GW150914, the successive direct detections of GW are reported from Advanced LIGO and Advanced VIRGO term ([25], [26], [27]) from the black-hole binaries, and GW from the merger of Neutron star binaries is also reported [28]. In Japan, a km-class laser interferometric GW detector named KAGRA [29] is now under construction in Kamioka mine, and, after test running in 2016, the observation run will be started in late 2019 for catching up and starting the GW astronomy.

2.2 Space gravitational wave detectors

Though km-class laser interferometric GW antenna (terrestrial GW detectors) succeeded in detecting GW, the strain sensitivity below 100 Hz is limited by seismic noise from the ground and its finite arm length (the detection band of terrestrial GW detector is 10 Hz - 1 kHz). In order to access GW at lower frequency range where many attractive targets are expected such as inspiral and merger of intermediate mass black hole binaries (IMBH) [30] or the inflation from early universe [31], space GW antenna is proposed. Since space GW detector can have much longer arm length and can be operated in the seismic noise free condition, the detection band is expanded to mHz. There are two missions are now undergoing, LISA in US and Europe [32], and DECIGO [33][34] in Japan. LISA is a triangle-shaped laser transponder with the arm length of 500000 km, whose observation band is around 10 mHz. In 2016, a milestone mission of LISA named LISA pathfinder (LPF) have been launched, and required acceleration noise level of LISA was successfully achieved [35]. On the other hand, DECIGO is a Fabry-Perot Michelson interferometer space gravitational wave detector, which is first proposed by Seto et.al. in 2001 [17]. In the following section, Japanese space gravitational detector project is overviewed.

2.2.1 DECIGO Pathfinder

The first space gravitational wave detector operating in spase is SWIM$\mu\nu$ which had been developed by Kokuyama et.al. in University of Tokyo. SWIM$\mu\nu$ consists of a torsion-bar antenna (TOBA) and satellite to ground communication bas, and was launched in 2009 carried by JAXA's small satellite, SDS-1, [36]. After successful 1-year operation of SWIM$\mu\nu$, a milestone mission of DECIGO named DECIGO pathfinder (DPF) was proposed, whose purpose is the feasibility tests of key technologies for DECIGO such as drug-free control, space-bone frequency-stabilized laser, and also has a scientific targets of GW detection and the global gravity field observation [37]. It will be planed to launch in 2019. Fig.2.1 and Fig.2.2 shows the schematic of DPF and the roadmap of space GW detectors, respectively.

DPF consists of a frequency-stabilized laser and one small Fabry-Perot

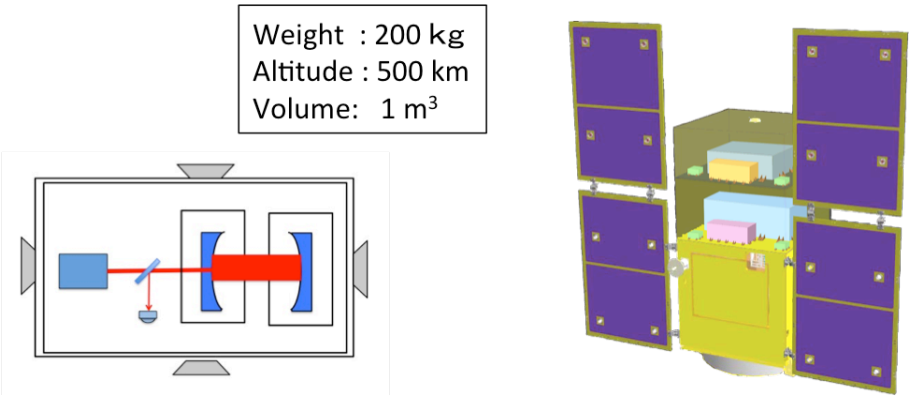

Figure 2.1. Schematic of DPF and the specification of the satellite; left is the frequency-stabilized laser and the interferometer, right is the small satellite for DPF

laser interferometer. Since all of the optical components and electrical instruments should be installed in $1m^3$-small satellite, the light source and another components are designed in accordance with specification of satellite. As shown in table 1, the stable laser at 1030 nm is required for the light source for DPF.

In the initial stage of my study, I have developed a light source for DPF: the frequency and intensity- stabilized laser at the wavelength of 1030 nm with the small output power of 20 mW, under the very strict condition of small size, limited consumption power for operating in a small satellite [38].

Table 1: Requirements for the light sourced of DPF and DECIGO

Project	Wavelength [nm]	Power [W]	frequency noise [Hz/$\sqrt{}$ Hz]@1 Hz	Relative intensity noise [/$\sqrt{}$ Hz @1 Hz]
DPF	1030	0.02	0.5	10^{-8}
DECIGO	515	10	1	10^{-8}

However, after two times rejections from the selection of the small satellite series associated by JAXA, DECIGO working group made a decision of skipping DPF, and concentrated ourselves in the next milestone mission named B-DECIGO (whose provisional name is Pre-DECIGO), and, according to the decision of our working group, the target of my study was moved

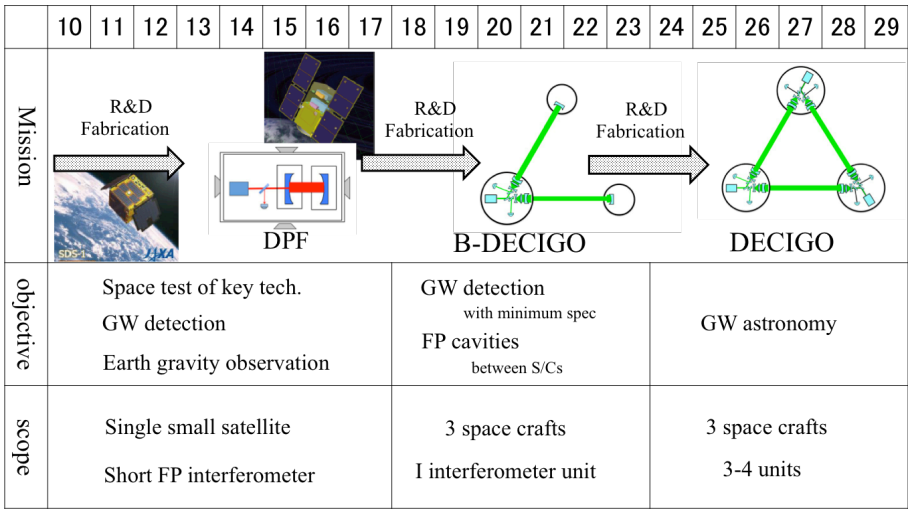

Figure 2.2. Road map of the space GW detectors in Japan: the vertical axis indicates the two lower digits of the dominical year

on to the developing of the light source for B-DECIGO.

2.2.2 DECIGO and B-DECIGO

DECIGO (Decihertz Interferometer Gravitational Wave Observatory) is a space-gravitational wave detector which has been promoted in Japan. The schematic is shown in Fig.2.3

The basic configuration of DECIGO is an equilateral triangle-shaped laser interferometer which includes three 1000-km Fabry-Perot Michelson interferometers with the including angle of 60 degree. Each satellite has two drag-free test mass mirrors, one stable light source, and two photo detectors [39]. One of DECIGO's targets is GW from inspiral and merger of intermediate-mass black hole binaries (IMBH) which will give us the formation mechanism of super massive black holes (SMBH) observed at the center of the galaxy. Most interesting target of DECIGO is stochastic background GW from the early universe which only DECIGO can detect. The stochastic background GW is originated from the inflation, and will give us the information about the secret of the birth of universe [40]. Before launching DECIGO in mid

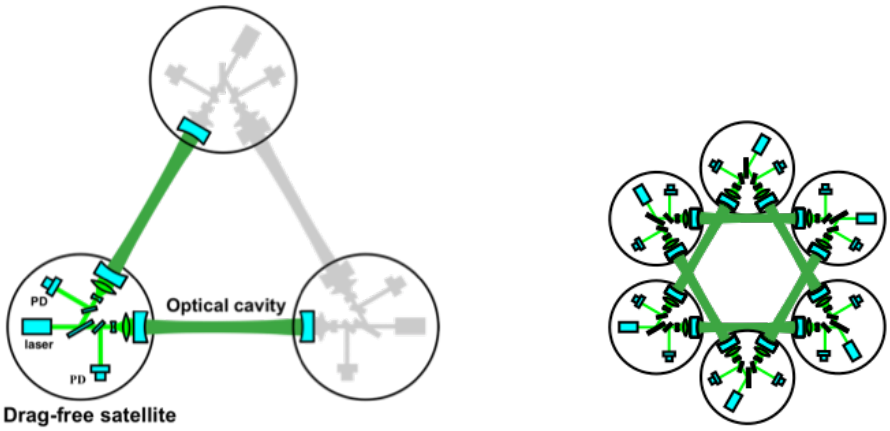

Figure 2.3. Conceptual design of DECIGO. Triangle-shaped Fabry-Perot interferometer with the arm length of 1000 km. The left is the two overlapped units of DECIGO for improving the strain sensitivity by correlation observations.

2030s, the milestone mission named B-DECIGO is also planned. B-DECIGO is downsized mission of DECIGO [41]. Though the strain sensitivity of B-DECIGO is lower than that of DECIGO, B-DECIGO has its original science targets such as gravitational wave originated from intermediate-mass black hole binaries. And one of the important purposes is the feasibility test of key technologies for realizing DECIGO such as drag-free control, formation flight, control of long-baseline interferometer, and the stable operation of the stabilized lasers in space.
The parameters of DECIGO and B-DECIGO are listed in table 2.

Table 2: Main parameter of DECIGO and B-DECIGO

Project	Arm length	mirror diam. [m]	Finesse	Mirror weight [kg]	Configuration
B-DECIGO	100	0.3	30	30	3satellites 1unit
DECIGO	1000	1	10	100	3 satellites/ 1 unite

In order to improve the strain sensitivity, a highly stable light source is essential. The requirements of the light source for DECIGO and B-DECIGO are listed in table3. The derivation of the required frequency and intensity noise are described in section 2.2.3.

Table 3: Requirements of the light source for DECIGO and B-DECIGO

Project	Wavelength [nm]	Frequency noise [Hz/$\sqrt{}$ Hz]@1 Hz	Relative intensity noise [/$\sqrt{}$ Hz @1 Hz]	Power [W]
B-DECIGO	515	1	10^{-8}	2
DECIGO	515	1	10^{-8}	10

The 1000-km optical cavity configuration stores much photons in it to decrease the shot noise limited level of the strain sensitivity at higher frequency range of the observation band. On the other hand, much photon gives the radiation pressure noise to the test mass mirrors which limits the strain sensitivity at lower frequency range. The output power requirements of the laser are determined from the design of the interferometer for optimizing the strain sensitivity curve to detect the science targets of the GW detectors. Fig.2.4 shows the expected strain sensitivity of DECIGO and the expected strain of cosmic phenomena. In case of 1 cluster (3 satellites/1 unite), the highest strain sensitivity of DECIGO is $dL/L = 10^{-23}$ level around 1 Hz. The correlation of the clusters (3 unite) improves the strain sensitivity which reaches $dL/L = 10^{-25}$ level around 1 Hz. In both cases, the sensitivity below 0.1 Hz and above 0.1 Hz are limited by the radiation pressure noise, the shot noise level, respectively.

2.2.3 Light source for space gravitational wave detector

Recently, space-borne lasers play important roles for not only laser ranging or lidar but also for precision measurement or frequency standards. Therefore, there are many plans to launch frequency-stabilized lasers [42], [43], [44]. Compared with these project, DECIGO requires much higher frequency and intensity stability to the light source.

As described in section 2.1 and 2.2.2, a highly stable light source is required for GW detector, and the noises in the interferometer should be suppressed to realize extremely high strain sensitivity. The main noises, which determine the strain sensitivity of Fabry-Perot laser interferometer, are (i)

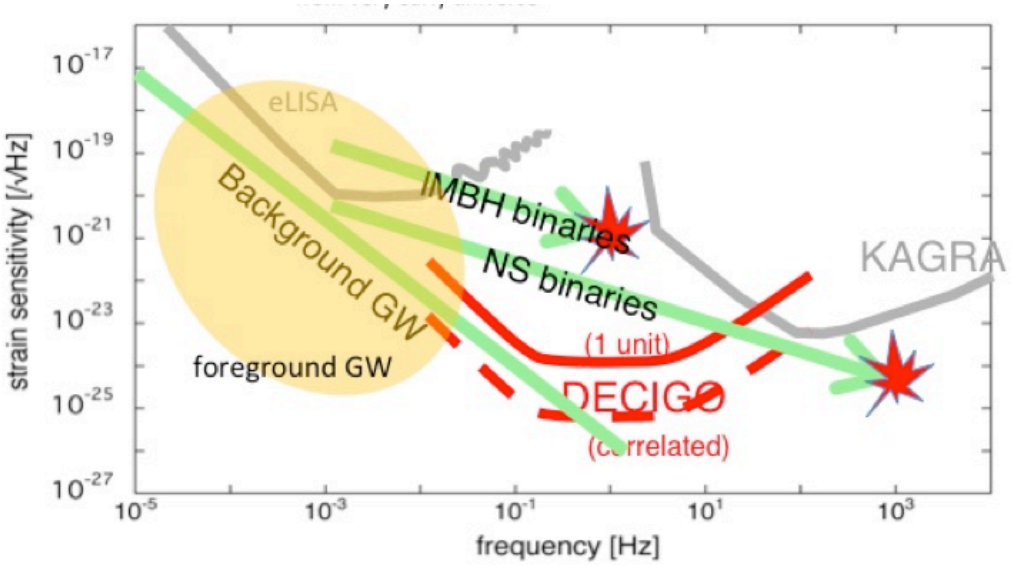

Figure 2.4. Strain sensitivity of DECIGO and B-DECIGO, and that of science targets are also marked

technical noise (frequency noise and intensity noise of the laser, thermal noise etc.) and (ii) theoretical quantum noise (shot noise and radiation pressure noise). The technical noises should be suppressed to be lower than the theoretical quantum noise level which limits the strain sensitivity of the space GW detector. The details of the technical noises of the light source are described below.

The frequency response function of the light source at Fabry-Perot laser interferometer $H_{FM}(\omega)$ is given as [45]

$$H_{FM}(\omega) = \frac{r_1 - r_2((t_1)^2 + (r_1)^2)e^{-2i\omega l/c}}{1 - r_1 r_2 e^{-2i\omega l/c}} \tag{2.1}$$

where r and t are the amplitude reflectance and amplitude transmittance of the mirrors, respectively. l is the cavity length. The subscription '1' and '2' in Eq.(2.1) denote front and end mirrors of the cavity. If each arm length and reflectance of the mirrors in both arms are identical, the frequency noise doesn't couple with the strain noise of GW detector. Actually, the parameters

of the interferometer have asymmetry and the frequency noise of the laser affects to the strain sensitivity of GW detector.
The equivalent strain sensitivity of GW $h(\omega)_{FM}$ limited by the frequency noise of the laser is written as

$$\begin{aligned} < h(\omega)_{FM}{}^2 > &= \left| \frac{H^{(1)}_{FM}(\omega) - H^{(2)}_{FM}(\omega)}{H_{FP}(\omega)} \right|^2 < \phi_n(\omega)^2 > \\ &\simeq \Gamma^2_{CMR} \left| \frac{H_{FM}(\omega)}{H_{FP}(\omega)} \right|^2 < \phi_n(\omega)^2 > \end{aligned} \tag{2.2}$$

where $\phi_n(\omega)$ is Fourier component of the laser phase noise, superscription (1) and (2) in (2.2) denote each arms of the interferometer.
The common-mode noise reduction (CMR), which is determined by the characteristic of each Fabry-Perot cavity, is written as

$$\Gamma_{CMR} = 2 \left| \frac{H^{(1)}_{FM}(\omega) - H^{(2)}_{FM}(\omega)}{H^{(1)}_{FM}(\omega) + H^{(2)}_{FM}(\omega)} \right| \tag{2.3}$$

Since r_1, r_2 of the large mirrors and l, which is used for each arms of Fabry-Perot laser interferometer, is hardly identical, the frequency noise of the laser, df/f, has certain amount of contribution to the strain sensitivity of GW detector.
If CMR=1, for example in the case of DPF with one arm cavity, dL/L is equal to df/f. In the case of DECIGO, CMR is designed to be 10^{-5}, and the frequency of the laser is finally stabilized in reference to the common mode of both arms, whose control gain is $G_{CM} = 10^5$. From these parameters, the frequency stability of the laser introduced into the interferometer, which is written as

$$df/f = \frac{dL/L \cdot CMR}{G_{CM}} \tag{2.4}$$

should be $df/f = 10^{-14}$ to achieve the strain sensitivity of $dL/L = 10^{-24}$. Therefore the requirement of the light source for DECIGO is $df/f = 10^{-15}$ at the observation band, which includes safety factor of 10.

In the interferometric measurement, the interference signal is detected by the photo detector (PD) and is converted into the voltage signal. Therefore,

the intensity noise of the light source should be reduced for improving the strain sensitivity of GW detector.
The photo current which is obtained from the interferometric measurement is written as [45]

$$I(t) \simeq I_{min} + (I_{eff}/2)[1 - J_0(m) + 2J_1(m)\delta\phi \sin\omega_m t - 2J_2(m)\cos 2\omega_m t] \quad (2.5)$$

where I_{min} is the photo current in the dark fringe, $I_{eff} = I_{max} - I_{min}$, $\delta\phi$ is the phase variation of the interference fringe, $J_n(m)$ is the nth Bessel function with the modulation index of m. If the intensity of the light source is varying, 2.5 is written as

$$I(t) = [1 + \delta I(t)/I(0)]I_{min} + (I_{eff}/2)[1 + J_0(m)\cos\phi - 2J_1(m)\sin\phi\sin\omega_m t] \quad (2.6)$$

$\Delta\phi = \Phi_0 + \delta\phi$, and 2.6 is demodulated at $\sin\omega_m t$,

$$\begin{pmatrix} \omega\, components\, of \\ demodulated\, signal \end{pmatrix} = \begin{pmatrix} \omega_m \pm \omega\, components\, of \\ (I/I(0)(I_{min} + (I_{eff}/2)[1 + J_0(m)\cos\Phi_0]) \end{pmatrix} + \begin{pmatrix} \omega\, components\, of \\ I_{eff}J_1(m)[I/I(0)]\sin\Phi_0 + \delta\phi\cos\Phi_0 \end{pmatrix} \quad (2.7)$$

The effect of intensity noise to the strain of the interferometer is written by

$$\delta\phi_{int} = \frac{\delta I}{I_0}\left\langle \Delta\Phi_0 \right\rangle_{rms} \quad (2.8)$$

where $\left\langle \Delta\Phi_0 \right\rangle_{rms}$ is the intensity noise, which is determined by the free-running intensity noise divided by control gain (error signal). Therefore insufficient servo gain causes the coupling of the demodulated signal and the intensity noise at observation band.
Next, theoretical quantum noise (shot noise and radiation pressure noise) is

described. In DECIGO project a green laser at 515 nm is used for the light source because shorter wavelength decrease the diffraction loss of the cavity which is critical for such a long cavity.
After satisfying requirement level of the intensity and frequency noise of the laser, the theoretical limit of the strain sensitivity of DECIGO is determined by quantum noise from the laser power. The quantum noise affects the strain sensitivity of DECIGO in two points, shot-noise and radiation pressure noise. The shot noise is caused from the randomness of input photon timing the to the detector [47], which gives the strain noise to the Fabry-Perot laser interferometer as

$$\delta x_{rad} = \frac{1}{8F}\sqrt{\frac{ch\lambda}{\eta P_L}\left[1+(\frac{f}{f_{cut}})^2\right]} \qquad [m/\sqrt{Hz}] \tag{2.9}$$

where F and f_{cut} are the Finesse and the cut off frequency of the F.P.cavity, respectively. As can be seen from Eq. (2.9), dx is inversely proportional to the square root of the laser power, P_L, and the frequency dependency is flat at lower frequency and is increasing at higher frequency above f_{cut}.
The radiation pressure noise is caused from the momentum of the randomly collided photons to test-mass mirrors, which gives the acceleration noise to the detectors, $delta f_{rad}$,

$$\delta f_{rad} = \frac{8F}{\pi}\sqrt{\frac{hP_L}{c\lambda[1+(\frac{f}{f_{cut}})^2]}} \qquad [N/\sqrt{Hz}] \tag{2.10}$$

The radiation pressure noise is proportional to the square root of the input laser power, P_L. Therefore, in principle, as the laser power increases, the shot-noise limited level is decreased and the radiation pressure noise is increased.
Fig.2.5 shows the designed strain sensitivity of DECIGO (blue solid trace) with the laser power of 10 W, and the noise limitation caused from the shot noise (blue dots) and radiation pressure noise (blue dashed trace).
As can be seen from Fig.2.5, lower frequency range of the strain sensitivity is limited by the radiation pressure noise, and higher frequency range is limited by the shot-noise. Red solid trace in Fig.2.5 is the strain sensitivity of DECIGO with the laser power of 30 W. At lower frequency range, the

strain sensitivity becomes worse due from the radiation pressure noise [46], and at higher frequency range shows the same noise level as that indicated by red trace, because the shot noise limited level at this frequency range is limited by the response function of the cavity. Therefore the profile of the strain sensitivity is designed from not only the laser power but also many other interferometer parameters such as Finesse and length of the cavity, weight and diameter of the test mass mirrors.

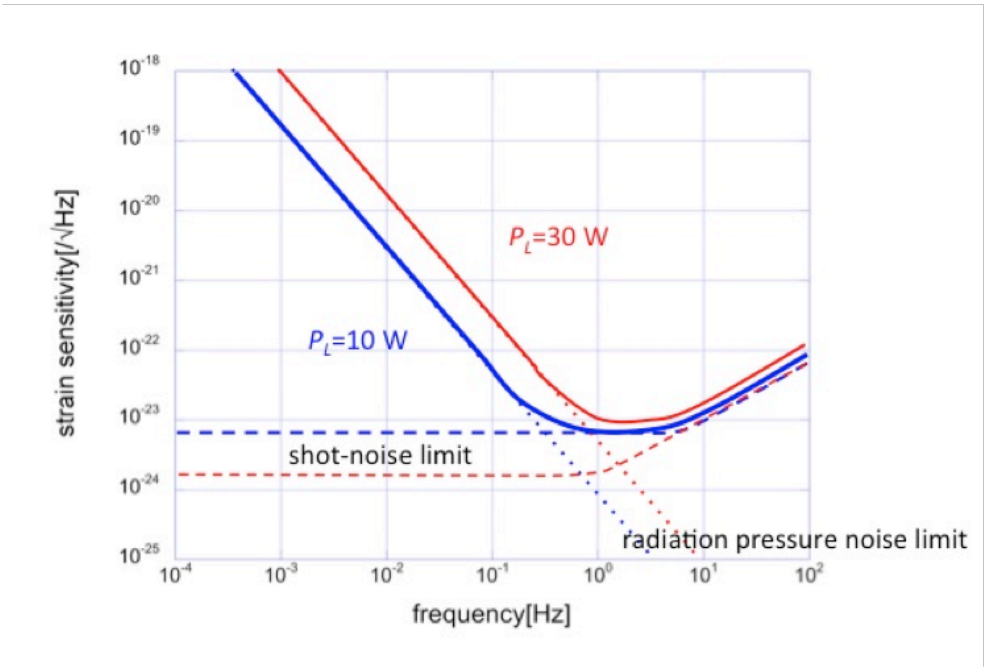

Figure 2.5. Designed strain sensitivity of DECIGO (solid trace) at laser power of 10 W (blue) and 30 W (red). Dashed traces and dots indicate shot-noise limit and radiation pressure noise limit, respectively

The intensity fluctuations of the laser cause acceleration noise to the test mass mirrors. In the case of DECIGO, the required intensity noise of the laser is calculated as follows. In order to achieve the strain sensitivity of $\delta L/L = 10^{-24}$ in the arm length of 1000 km, the displacement noise, δL, should be lower than 10^{-18} m which corresponds to the acceleration noise, δa, of 10^{-18} m/s^2 at 1 Hz. Therefore the force noises on the 100-kg mirrors, δF, should also be lower than $\delta F = M \times \delta a = 10^{-16}$ N/$\sqrt{Hz}$ at 1 Hz.

The theoretical limit of the force noise comes from the radiation pressure fluctuations $\delta P/P$ which is written as $\delta P/P$ is $\frac{1/2\times\delta FC}{P} = 1.5 \times 10^{-10}$. In consideration of the common-mode noise reduction ratio (CMRR) of 10^3, the relative intensity noise should be less than $\delta I/I = 1.5 \times 10^{-8}/\sqrt{Hz}$ to realize the required radiation pressure fluctuations.

2.2.4 Light source for other space missions

In other space GW project, for example LPF, a cavity-stabilized Nd:YAG laser with the wavelength of 1064 nm is used for the light source [44]. The light source for LPF had been launched, and the feasibility tests of key technologies such as the frequency stabilization of the laser has been achieved [35]. In the main mission, LISA, a cavity-stabilized NPRO (standard type) and cavity-stabilized micro NPRO are candidates for the light source, whose wavelengths are 1064 nm. In LISA projects, since the short-term frequency stability is required, the optical cavity resonance is chosen for frequency reference. The engineering model (EM) already have been made in 2018, and it is planed to be launched in 2034 [50].

In pararel with the cavity-stabilized lasers, the EM and the elegant breadboard model (EBB) of the iodine-stabilized Nd:YAG lasers for LISA have also been developed over recent years [48]. The long-term frequency stability of $df/f = 10^{-15}$ level has been achieved by the suppression of the the residual amplitude noise (RAM), and good short-term stability also have been achieved by the improvement of SNR of the frequency reference [49]. The prototype of the these iodine-stabilized laser had performed flying test by using a sounding rokect (JOKARUS) [51].

In another space mission, for the exploration of gravity field, an iodine-stabilized external cavity semiconductor laser (λ =1.5 μm Redfern Integrated Optics (RIO)-OptaSense Inc.[52]) have been developed. They use the 514-nm iodine absorption line for frequency reference. The wavelength of 514 nm for stabilization is obtained from the sum frequency generation between second harmonics 2ω and fundamental ω of the laser at the wavelength of 1.5 μm. The long-term frequency stability of df/f=5.73$\times 10^{-15}$ at 100 s is achieved [53].

3 Saturation spectroscopy of Iodine absorption line

The molecule absorptions are one of the excellent frequency references. Compared with the resonance of the Fabry-Perot cavity, the absolute frequency are fixed (although the frequency is shifted by pressure, collision or external electric and magnetic field). he molecule absorptions show the better long-term frequency stability because the absorption frequency is less sensitive to the external perturbations such as vibrations or temperature variations. On the other hand, the frequency stability, especially short-term frequency stability, is limited by SNR of the frequency discrimination signal obtained from the molecular absorption.
For improving signal to noise ratio (SNR) of the signal, the narrower linewidth and low background noise are essential. Though the theoretical limit of the linewidth is the natural linewidth determined from the upper state lifetime of the transition, some broadening effects expand the linewidth. The dominant broadening effect is Doppler broadening which expands the linewidth by more than a few GHz.
Therefore, in this section, the Doppler free spectroscopy and other low noise signal detection techniques used in my experiments, and the line broadening effects are discussed, which is used for fixing the parameter of our experimental setups.

3.1 Signal detection

We use the molecular saturated absorption signal as a frequency references. In the case of using the absorption of iodine molecules as a frequency reference, the short-term frequency stability is determined by the signal to noise ratio (SNR) of the saturated absorption signal. Therefore, the offset-free frequency discrimination signal with high SNR is essential for obtaining high short-term frequency stability around 1 Hz.
In this section, I will give a brief introduction about the Frequency modulation spectroscopy and modulation transfer technique which are used for detecting the frequency discrimination signal in my study.

3.1.1 Saturated absorption spectroscopy

The linewidth of linear absorption signals such as the molecules or atoms are broadened by Doppler broadening effect inhomogeneously. Narrower saturated absorption signal can be obtained by dispersing specific molecules which has the same velocity. One of the Doppler-free spectroscopy is the saturated absorption spectroscopy which is first applied to He-Ne laser [54][55], and widely utilized with modulation technique [56][61][].
In Fig.3.1, the laser beam is introduced into the glass cell (molecules are enclosed). As the molecules are existed under the Boltzmann distribution in the thermal equilibrium state (Fig.3.2), the Doppler effect is appeared when the molecules are dispersed by the laser sweep. The linear absorption signal is detected by the photo detector (PD) which is proportional to the unabsorbed photon through the cell.

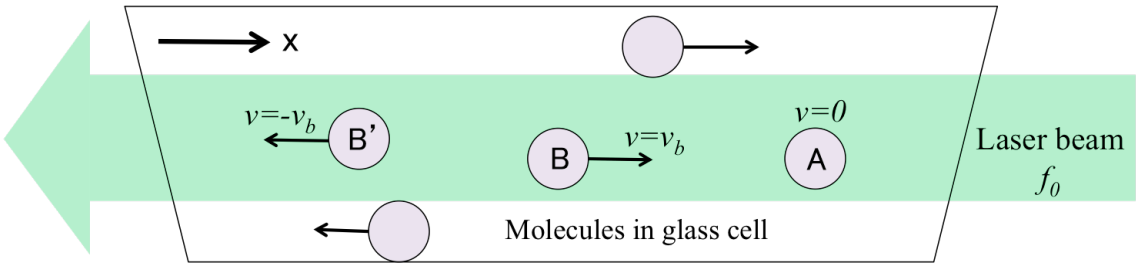

Figure 3.1. Schematic of saturated absorption spectroscopy

In the case of Fig.3.3, two laser beams are counter-propagated collinearly, and the frequency of one beam is fixed (pump beam) and the other is swept (probe beam). The molecules, which resonate with the pump beam, absorb the photon to transit the excited state and the small dip signal is observed at the probe beam. This phenomenon is called spectral hole burning (Fig.3.4).

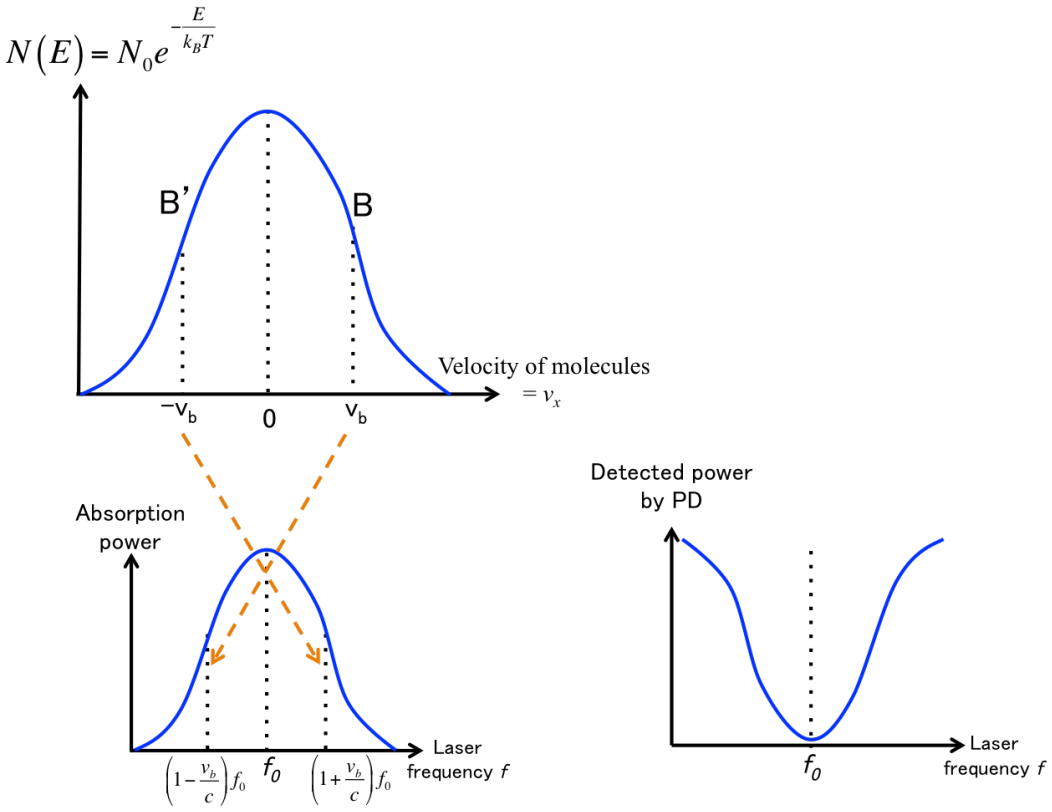

Figure 3.2. Boltzmann distribution in the thermal equilibrium and absorption of molecules

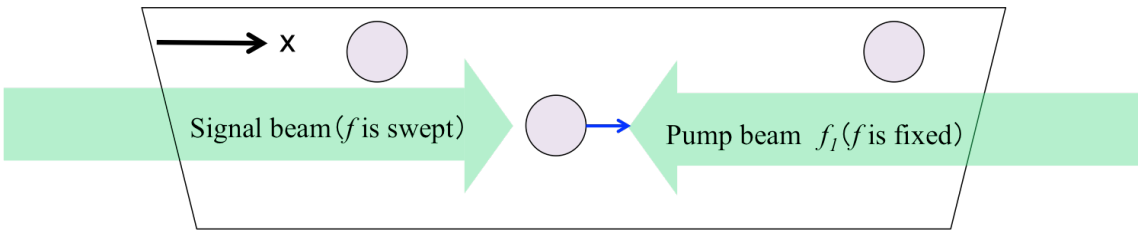

Figure 3.3. Schematic of saturated absorption spectroscopy

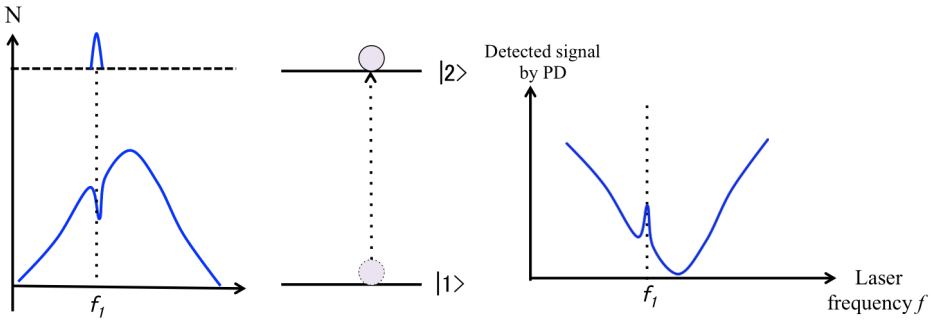

Figure 3.4. Schematic of saturated absorption spectroscopy

Spectral hole burning also can be obtained by two laser beams whose frequency are the same and swept synchronously. In Fig.3.5, one laser beam is divided into two beams and introduced into glass cell in which the molecule with the center absorption frequency of f_0, are filled. When the laser frequency is tuned with the frequency difference of $+\Delta f$ from the $f_0(f_L = f_0 + \Delta f)$, each beam (+ direction and − direction) are absorbed the molecules with the velocity of $\nu_{\pm} \approx \pm(\Delta f / f_0)C$ because of Doppler effect, and the dips are appeared at the velocity distribution of the molecules at the ground state.

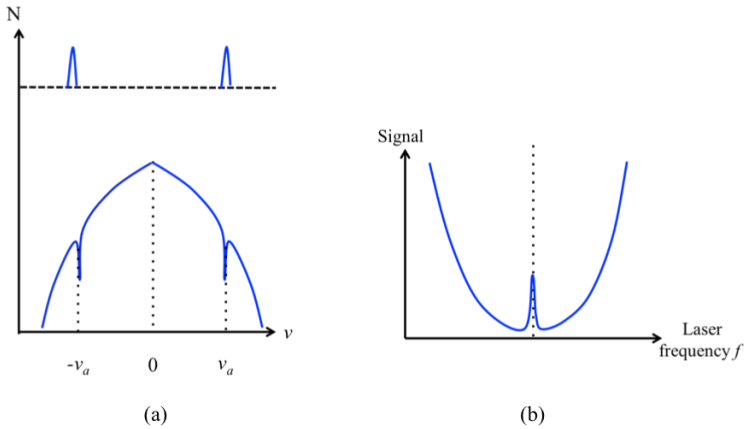

Figure 3.5. (a)Saturated population distribution of lower and upper state with two counter-propagated beam, (b)Intensity of the transmitted laser beam through the molecular cell. At the center of the linear absorption, a narrow saturated absorption peak is appeared.

Therefore the saturated population difference between two states are written as

$$\Delta N(\nu) = [1 - \frac{S_0(\gamma/2)^2}{(2\pi\Delta f - k\nu)^2 + (\gamma_s/2)^2} - \frac{S_0(\gamma/2)^2}{(2\pi\Delta f + k\nu)^2 + (\gamma_s/2)^2}]\Delta N_0(\nu) \tag{3.11}$$

where, $\Delta N_0(\nu)$ is the thermal population difference of the initial thermal distribution between two states without saturation light, S_0, γ, γ_0, v are saturation parameter, homogeneous width of the transition, $\gamma = \gamma_0\sqrt{1+S_0}$, velocity component of molecules along the laser propagation, respectively [70]. In the condition of $f = f_0$, two laser beams resonate with the same molecules whose velocity component is $v = v_0$, and spectral hole burning is observed.
Under these conditions, the absorption coefficient of the molecules with the function of f is written as

$$\alpha_s(f) = [1 - \frac{S_0}{2}(1 + \frac{\gamma_s/2)^2}{[2\pi(f - f_0)k]^2 + (\gamma_s/2)^2}]\alpha_0(f) \tag{3.12}$$

where $\alpha_0(f)$ is the absorption coefficient without saturated light [56]. Fig.3.5(b) shows intensity of the transmitted beam of the two counter-propagated light through the molecular cell, and the narrow peak is appeared at $f = f_0$ in the broad linear absorption profile, which is called saturated absorption signal.

3.1.2 Frequency modulation spectroscopy

By using Doppler free spectroscopy such as the saturated absorption spectroscopy, Doppler-free narrow absorption lines are observed. And from such narrow resonances, steep 1^{st} derivative signals with high SNR can be obtained by using frequency modulation spectroscopy. The basic idea has been proposed by Pound in the microwave region [60], and was expanded to the light frequency region by Drever and Hall [59]. This frequency modulation spectroscopy technique is widely used for obtaining the frequency discrimi-

nation signal of frequency-stabilized lasers, which can be applied to not only Fabry-Perot cavities but also molecular absorptions. The principle of Frequency modulation spectroscopy is as follows.
The schematic of the Frequency modulation spectroscopy is shown in Fig.3.6

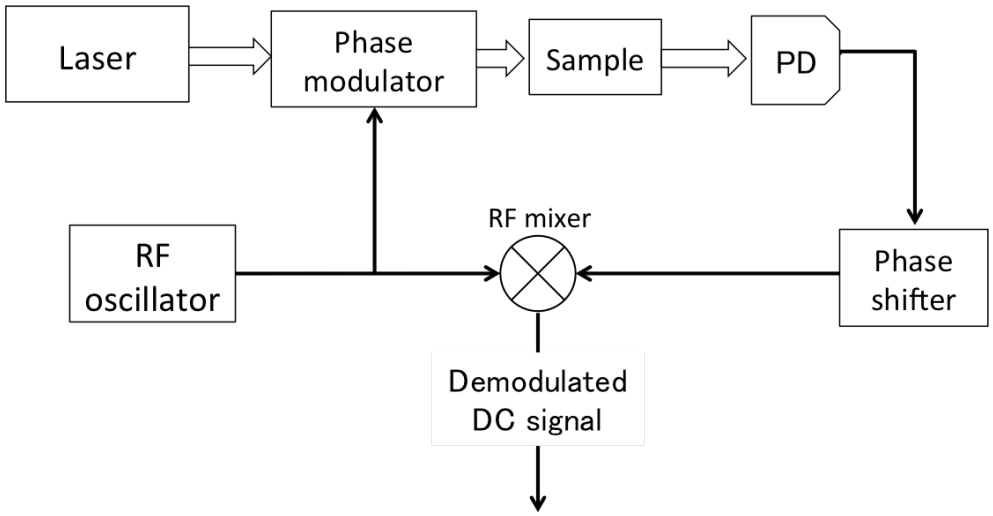

Figure 3.6. Experimental diagram of Frequency modulation spectroscopy

The laser is phase modulated at certain frequency, f_m, to generate frequency sidebands on either sides of carrier frequency with the frequency separation of $f_m(f_L + f_m$ and $f_L - f_m)$ in the opposite polarity. In the case of the Fabry-Perot cavity, the carrier is on resonance to the cavity and the averaging light inside the cavity goes back to a PD which is used as the frequency reference, and both sidebands that is off resonant to the cavity are reflected directly from the cavity to the PD which has the same frequency (phase) fluctuations as the laser. Therefore, the frequency fluctuations of the laser can be detected as the interference between averaged carrier beam and reflected sidebands. The modulation frequency should be higher enough that the laser intensity noise is falling near the shot-noise limited level (typically a few tens MHz), and the noise of the demodulated signal reaches the shot noise limited level.
The phase modulated electric field with the modulation frequency $\omega_m = 2\pi f_m$

by a phase modulator such as an electro-optic modulator (EOM) is written as

$$E = E_0 \exp i(\omega t + m \sin \omega_m t) = E_0 \exp i\omega t \sum_{n=-\infty}^{\infty} J_n(m) \exp(i\omega_m t) \quad (3.13)$$

where $J_n(m)$ is the nth Bessel function with the modulation index of m. $n = -1, 1, 0$ th terms of this equation represent lower and upper sidebands and carrier, respectively. After passing through the molecular sample cell of length L whose absorption coefficient α, and the refraction index η, the transmitted electric field $E_3(t) = 1/2\tilde{E}_3(t) + c.c.$ is written by

$$\tilde{E}_3(t) = E_0 \left[T_0 \exp i\omega t + T_1 \frac{M}{2} \exp i(\omega + \omega_m)t - T_{-1} \frac{M}{2} \exp i(\omega - \omega_m)t \right] \quad (3.14)$$

where T_n is complex amplitude transmittance $T_n = exp(\delta_n - i\phi_n)$, δ_n is the amplitude attenuation $\delta_n = \alpha_n L/2$, $i\phi_n$ is the optical phase shift $i\phi_n = \eta_n L(\omega_c + n\omega_m)/c$. The angler frequency of $\omega+\omega_m$, ω, $\omega-\omega_m$ correspond to the modulation index of $n = -1, 0, +1$, respectively. The electrical signal obtained from PD is given by $I(t) = c|\tilde{E}_3(t)|^2/8\pi$. Since $M^2 \simeq 0$, $I(t)$ is written as

$$\begin{aligned} I(t) = \frac{cE_0^2}{8\pi} e^{-2\delta_0} \{ 1 + [e^{\delta_0 - \delta_1} \cos(\phi_1 - \phi_0) - e^{\delta_0 - \delta_{-1}} \cos(\phi_0 - \phi_{-1})] M \cos \omega_m t \\ + e^{\delta_0 - \delta_1} \sin(\phi_1 - \phi_0) - e^{\delta_0 - \delta_{-1}} \sin(\phi_0 - \phi_{-1})] M \sin \omega_m t \} \end{aligned} \quad (3.15)$$

If $|\delta_0 - \delta_1|$, $|\delta_0 - \delta_{-1}|$, $|\phi_0 - \phi_1|$, $|\phi_0 - \phi_{-1}|$ is small compared with 1, Eq.3.15 is written by

$$I(t) = \frac{cE_0^2}{8\pi} e^{-2\delta_0} [1 + (\delta_{-1} - \delta_1) M \cos \omega_m t + (\phi_1 - \phi_{-1} - 2\phi_0) M \sin \omega_m t] \quad (3.16)$$

The first term in Eq.(3.16) is in-phase signal which indicates the absorption of the molecules, and the second term is the quadrature signal. Each

signals can be obtained by demodulating at $\cos\omega_m t$, and $\sin\omega_m t$, respectively [61].

The detail mechanism for obtaining 1^{st} derivative signals is described below. After passing through the molecular cell which have the frequency-dependent amplitude absorption coefficient of $A(\omega)$, the electric fields of the upper, E_U, lower, E_L, sidebands and carrier, E_C, are also written as

$$\begin{aligned} E_L &= E_0 J_{-1}(m) A(\omega-\omega_m)\exp i(\omega-\omega_m)t = \alpha \exp i(\omega-\omega_m)t \\ E_U &= E_0 J_{+1}(m) A(\omega+\omega_m)\exp i(\omega+\omega_m)t = \beta \exp i(\omega-\omega_m)t \\ E_C &= E_0 J_0(m) A(\omega)\exp i\omega t = \gamma \exp i\omega t \end{aligned} \tag{3.17}$$

where $\beta = E_0 J_{+1}(m)A(\omega+\omega_m)$, $\gamma = E_0 J_0(m)A(\omega)$ and $\alpha = E_0 J_{-1}(m)A(\omega-\omega_m) = -E_0 J_{+1}(m)A(\omega-\omega_m)$ because $J_{-1}(m) = -J_{+1}(m)$

When all these sidebands are detected by a photo detector, the photocurrent from the photo diode is proportional to the square of those electric fields as

$$\begin{aligned} |E|^2 &= (E_C + E_U + E_L)(E_C^* + E_U^* + E_L^*) \\ &= |\alpha|^2 + |\beta|^2 + |\gamma|^2 + 2\alpha\beta\cos\omega_m t + 2\beta\gamma\cos\omega_m t + 2\alpha\gamma\cos(2\omega_m t) \end{aligned} \tag{3.18}$$

The detected voltage signal from PD, $V_{sig} = \frac{1}{2}\varepsilon|E|^2\eta R = C|E|^2$, is demodulated with the local oscillator $V_{LO} = V_L\cos\omega_m t$ into

$$\begin{aligned} V_{dem} &= V_{sig} \times V_{LO} \\ &= V_L C[(\alpha^2+\beta^2+\gamma^2)\cos\omega_m t + 2\gamma(\alpha+\beta)\cos^2\omega_m t + 2\alpha\beta\cos 2\omega_m t\cos\omega_m t] \end{aligned} \tag{3.19}$$

After passing through a low-pass filter, time-averaged demodulated signal is

$$
\begin{aligned}
V_{dem} &= V_L C\gamma(\alpha+\beta) = V_L C E_0^2 J_0(m) J_1(m)(-A(\omega-\omega_m)+A(\omega+\omega_m)) \\
&= V_L C E_0^2 J_0(m) J_1(m) \times 2\omega_m A(\omega)\frac{\partial A(\omega)}{\partial \omega} \\
&= V_L C E_0^2 J_0(m) J_1(m) \times \frac{\partial}{\partial \omega}|A(\omega)|^2
\end{aligned}
\tag{3.20}
$$

$$
(\because \tfrac{\partial}{\partial \omega}|A(\omega)|^2 = 2A(\omega)\tfrac{\partial A(\omega)}{\partial \omega})
$$

Therefore, the demodulated signal, V_{dem}, is proportional to the 1^{st} derivative of the intensity absorption profile, $|A(\omega)|^2$.
From the signal obtained by frequency modulation technique, we can achieve the frequency discrimination signal with the shot-noise limited noise level.

3.1.3 Modulation transfer spectroscopy

As is mentioned above, 1^{st} derivative of the absorption signal is obtained from the frequency modulation technique. However, as can be seen in Fig.3.5(b), the narrow saturated absorption peak is appeared in broad linear absorption profile. Therefore, the 1^{st} derivative of the narrow saturated absorption signal includes large signal offset which caused from the 1^{st} derivative of the broad linear absorption. The large signal offset cases the fluctuations of the locking point, and results in the frequency instability of the frequency-stabilized laser. Therefore the modulation-transfer technique have been proposed to cancel the frequency offset from the saturated absorption signal [62], [63]. In the modulation-transfer technique, the phase (or frequency, intensity) modulation is applied not to the probe beam but to the pump beam. The mechanism of modulation-transfer technique is described below.

In Fig.3.4, the pump beam is phase-modulated at the frequency, δ, and the probe beam is frequency-shifted, Δ, by an acoust-optic modulator (AOM). When the pump and the probe beams are counter-propagated in the molecular sample cell and the signal beam is frequency-shifted by an AOM, the signal wave, ω_4, is generated by the energy conservation which is accounted for by four-wave mixing process [64].
Four-wave mixing in two-level system is shown in Fig.3.7.

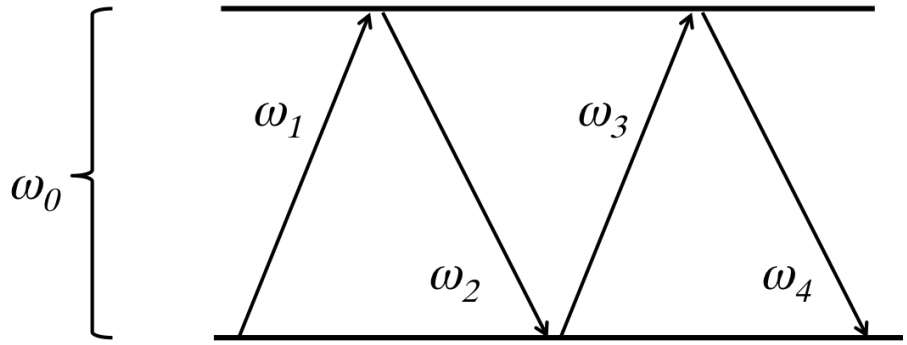

Figure 3.7. System of four-wave mixing

when the laser frequency is ω, ω_1 and ω_2 are the upper and lower sideband of the pump frequency, respectively. ω_3 is the probe frequency. The three frequency of ω_1, ω_2 and ω_3 are interacted each other to produce ω_4. These frequencies are described as

$$\begin{aligned} \omega_1 &= \omega + \Delta + \delta \\ \omega_2 &= \omega + \Delta - \delta \\ \omega_3 &= \omega \\ \omega_4 &= \omega \pm 2\delta \end{aligned} \tag{3.21}$$

When the frequency of the laser is away from the resonant frequency ω_0, each probe and pump beams resonate with the different molecules at the different velocity, (see Fig.3.5(a)), and the demodulated signal from the probe beam is null. When the laser frequency ω is tuned to the resonant frequency, both the probe and the pump beams are on resonance to the molecules with the same velocity component v. In that case, ω_4 is produced by four-wave mixing, and interferes with the probe beam, and generates the heterodyne beat signal of 2δ, whose phenomena is called modulation transfer to the probe beam from the pump beam.

In a Doppler-broadened molecules, in the two-level system, Fig.3.7 can be described below

$$\begin{aligned}
&\omega_1 + kv = \omega_0 \\
&\omega_1 + kv - (\omega_2 + kv) = 0 \\
&\omega_1 + kv - (\omega_2 + kv) + (\omega_3 - kv) = \omega_0
\end{aligned} \tag{3.22}$$

where ω_0 is Doppler shift with the molecule velocity component v. According to Eq.(3.22), these conditions are also written by

$$2\omega_1 - \omega_2 + \omega_3 = 2\omega_0 \tag{3.23}$$

From Eq. (3.21) and (3.23), the center frequency of the Doppler-free resonance is written by

$$\omega = \omega_0 - \frac{\Delta}{2} \pm \frac{3\delta}{2} \tag{3.24}$$

Eq.(3.24) indicates that the laser frequency is shifted by the frequency of AOM by Δ.

Therefore, the combination of frequency modulation technique and modulation transfer technique gives us the offset-free frequency discrimination signal at the center of the saturated absorption signal. Note that the modulation frequency is limited to the linewidth of the molecules for obtaining strong signal because the interaction between the probe and pump beam is activated within the linewidth of the resonance.

3.2 Selection of frequency reference

In Sub-Doppler spectroscopy of the iodine molecules, the relation of resonance frequency and linewidth of the saturated absorption lines are explained by the dissociation limit [65]. Considering $B \rightarrow X$ transition, as a ro-vibrational B state approaches the dissociation limit (499.5 nm), two atoms of iodine molecules act as the separated atoms. In the separated-atom model, atomic state of B and X correspond to ${}^2\mathrm{P}_{\frac{3}{2}} + {}^2\mathrm{P}_{\frac{1}{2}}$ and ${}^2\mathrm{P}_{\frac{3}{2}} + {}^2\mathrm{P}_{\frac{3}{2}}$ atomic state, respectively, and $B \rightarrow X$ transition becomes an electric dipole forbidden transition, $\mathrm{P}_{\frac{1}{2}} \rightarrow {}^2\mathrm{P}_{\frac{3}{2}}$, which results in short lifetime and narrower linewidth. When B state level approaches the dissociation threshold, the effect of predissociation limit also appears in not only ro-vibrational level

but also each hyper fine components. Therefore each linewidth should be examined and compared. The detail discussion about dissociation limit is should be refereed in [65][66]

In our study, the iodine-saturated absorption line at 515 nm is used for frequency reference. In conventional iodine-stabilized lasers, the saturated absorption line of the iodine molecules at 532 nm is used, which shows high long-term frequency stability and is utilized as a frequency standards. On the other hands, the short-term frequency stability is relativity low due to its low SNR of the detected signal. The absorption signal at 515 nm is expected to be narrower because it is near the dissociation limit of the iodine transition and the transition probabilities from the upper state become smaller, which results in the narrower linewidth. The linewidth of I_2-saturated absorption lines between 523 nm and 498 nm is reported by JILA groups [67], and also 514.67 nm absorption of iodine molecule was investigated [68]. In this frequency region, as frequency approaches to the dissociation limit, the effect of linewidth narrowing is larger than that of the signal strength decreasing, and hence, the SNR of the signal is increasing. Therefore the SNR at 515 nm is better than that at 532 nm, and we chose the absorption line at 515 nm instead of using 532 nm absorption line.

The laser with low intrinsic noise and high frequency controllability is important for obtaining the high frequency stability. The second harmonics of the ytterbium-doped solid state lasers at 1030 nm can access to the saturated absorption signal at 515 nm. First, we use the Yb-doped NPRO (LD-pumped non planer ring oscillator) as a light source, because the Nd-doped NPRO is very stable and is used for frequency stabilized lasers or the light source for the current GW detectors [69]. However, compared with the Nd-doped NPRO, the Yb-NPRO is found that the optical characteristics are worse, such as mode-hopping, beam degradation, the frequency drift etc., which are insufficient for using as the light source of the frequency-stabilized laser. Therefore we use an Yb-doped fiber DFB laser at 1030 nm, which shows good performance enough for obtaining the high stability.

We have developed frequency stabilized Yb-fiber DFB lasers in reference to the saturated absorption line of iodine molecules at 515 nm.

3.3 Linewidth broadening effect

As is mentioned above, the natural linewidth of the iodine saturated absorption signal at 515 nm is narrower than that of 532 nm. However, the linewidth of saturated absorption line is broadened by not only inhomogeneous (Doppler broadening) but also homogeneous broadening such as the pressure broadening, transit time broadening etc. [70]. In order to obtain the high SNR signal, we optimize the condition of the signal detection for obtaining the narrower linewidth with strong signal strength. In this section, we discuss about the broadening effect for determine the condition of the signal detection in our experiments.

3.3.1 Pressure broadening

The pressure broadening effect is caused from two reasons ; (i) phase shift caused from the collision between molecules or atoms. (ii) the lifetime of molecules or atoms at excited state is shorten by collision. The main contribution of pressured broadening in our experiments is (ii).
The intensity profile effected by pressure shift is described as [70]

$$I(\omega) = \frac{C*}{(\omega - \omega_0 - \Delta\omega)^2 + (\gamma/2)^2} \tag{3.25}$$

Where $\Delta\omega$ is the absorption shift, which is determined by the density of atoms N_B, the collision cross-section of the absorption shift σ_s, and written as

$$\Delta\omega = N_B \cdot \bar{v} \cdot \sigma_s \tag{3.26}$$

The excited state decay rate caused from the pressure broadening,γ ,is determined by the density of atoms N_B, the collision cross-section of the absorption shift σ_s.

$$\gamma = \gamma_n + N_B \cdot \bar{v} \cdot \sigma_b \tag{3.27}$$

Where γ_n is natural decay rate. Pressure broadening effects are experimentally discussed in section 3.4.1.

3.3.2 Transit time broadening

In the laser spectroscopy, the interaction time of the molecules with the laser light is shorter than the natural lifetime from the excited state. When the diameter of the laser beam is d, and the average thermal velocity is υ, the interaction time T of the molecules with the laser light is written as $T = d/|\upsilon|$, which is much shorter than the natural lifetime by few orders. Under this condition, the linewidth is not determined by the natural linewidth but the transit time T. In the case that the molecules are passing across the laser beam, the amplitude of the oscillator $x(t)$ in the harmonic oscillator $x = x_0 \cos \omega_0 t$ is kept constant during the crossing time of T, and is suddenly drop to zero. The Fourier spectrum of this oscillator is written as

$$A(\omega) = \frac{1}{\sqrt{2\pi}} \int_0^T x_0 \cos(\omega_0 t) \mathrm{e}^{-i\omega t} dt \tag{3.28}$$

The electric field distribution of the single Gaussian beam with the diameter of $2w$ is described as

$$E = E_0 \mathrm{e}^{-r^2/w^2} \cos \omega t \tag{3.29}$$

By substituting the amplitude of the forced oscillator $x = \alpha E$ into Eq.3.28, the Gaussian line profile is obtained as

$$I(\omega) = I_0 \exp(-(\omega - \omega_0)^2 \frac{w^2}{2\upsilon^2}) \tag{3.30}$$

whose linewidth $\Delta\omega$ (FWHM) is limited by the transit time.

$$\delta\omega_{tt} = 2(\upsilon/w)\sqrt{2\ln(2)} \simeq 2.4\upsilon/w \tag{3.31}$$

It is shown that FWHM is limited by the transit time and whose broadening effect (transit time broadening) can be suppressed by cooling the molecules to slow down their velocity or expanding the beam diameter.
In our experiments, transit time broadening effect of the iodine molecules is suppressed by expanding the laser beam diameter. From the law of equipartition of energy,

$$\begin{aligned} \frac{1}{2}mv^2 &= \frac{1}{2}k_B T \\ Nmv^2 &= Nk_B T \end{aligned} \tag{3.32}$$

Where k_B is Boltzmann constant, and N is Avogadro's constant. When temperature T=263 K and molecular weight Nm=254 are substituted into the Eq.(3.32), the velocity of the iodine molecules is v=92.46 m/s. In order to obtain the FWHM of less than 100 kHz, the laser beam diameter should be lager than $2w$=1.4 mm, which is calculated from the Eq. 3.32. Therefore the beam diameter of our experimental setup is expanded to $2w$ =2 mm by a couple of the optical lenses.

3.4 Precision spectroscopy of iodine absorption lines

In order to improve the short-term frequency-stability of the laser, the SNR of the frequency reference should be improved, and the SNR is evaluated precisely.

In this section, our new precision iodine spectroscopy system to evaluate the pressure broadening of I_2-saturated absorption signal is described.

In our initial stage, we investigate the shape of the saturated absorption lines of the iodine molecule where the laser frequency was swept by using a PZT-driven frequency actuator and the frequency was calibrated from the applied voltage to the PZT. The problems of our conventional spectroscopy system described above are (i); low resolution, (ii); uncertainty of the frequency axis and (iii); lower SNR. (i); In the case that we obtain the frequency discrimination signal by using the Yb:fiber DFB laser at free-running state, the frequency resolution of the signal is relatively low that comes from its wide laser linewidth (df=80 kHz). (ii); we used to measure the I_2-saturated absorption signals where the frequency of the laser is swept by using a PZT-driven frequency actuator, and the signal is obtained by the oscilloscope. The time axis in the obtained data should be calibrated into frequency axis by the sweep voltage signal from PZT driver. However, as described in (i), the fluctuations and drift of the laser frequency and hysteresis of a PZT degrade the accuracy of the frequency axis. Therefore, the signal and the

frequency axis should be obtained synchronously. (iii) Due to the multi pass configuration in BBM, the linear absorption of iodine is saturated and the I_2-saturated absorption signals are weakened which comes from the decrease of contrast between the linear absorption and the saturated absorption. In Fig.3.8, it is shown that the frequency axis of the linear absorption signal and the saturated absorption lines are mismatched because of (i) and (ii), and the I_2-linear absorption is saturated and I_2-saturated absorption signals are weakened because of (iii).

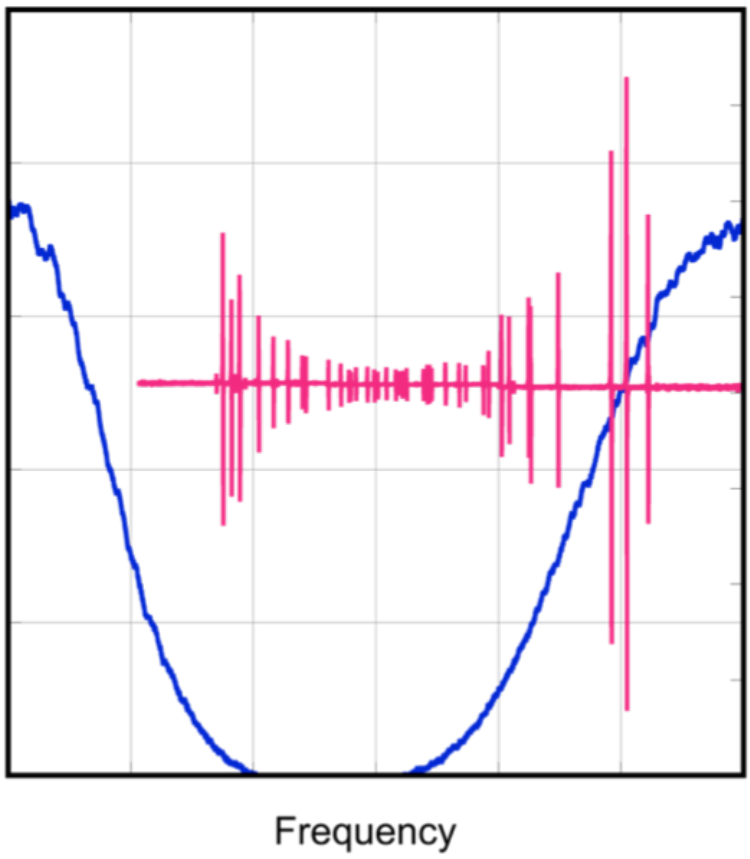

Figure 3.8. Linear absorption signal (blue trace) and the saturated absorption signal (red trace) of iodine at 515 nm. It is shown that at the center of the linear absorption, the absorption is saturated and the saturated absorption signals become weak.

In order to solve these problems, (i) (iii), we have developed a new precision spectroscopy system which consists of the frequency stabilization (light

source) part, the frequency sweeping part, and the signal acquisition part, which is shown in Fig.3.9. The frequency-stabilized laser is obtained from BBM whose frequency is stabilized to the I_2-saturated absorption signal at 515 nm. The frequency-stabilized green light is introduced into the frequency sweeping part. The frequency of the laser is shifted by using Acoust-optic deflector (AOD) which is driven by a microwave signal from a hand-made PC-controlled direct digital synthesizer (DDS). Double-pass configuration cancels the pointing fluctuations of the output beam in frequency sweeping. The frequency-shifted light is introduced into the signal acquisition part to obtain the saturated absorption signal.

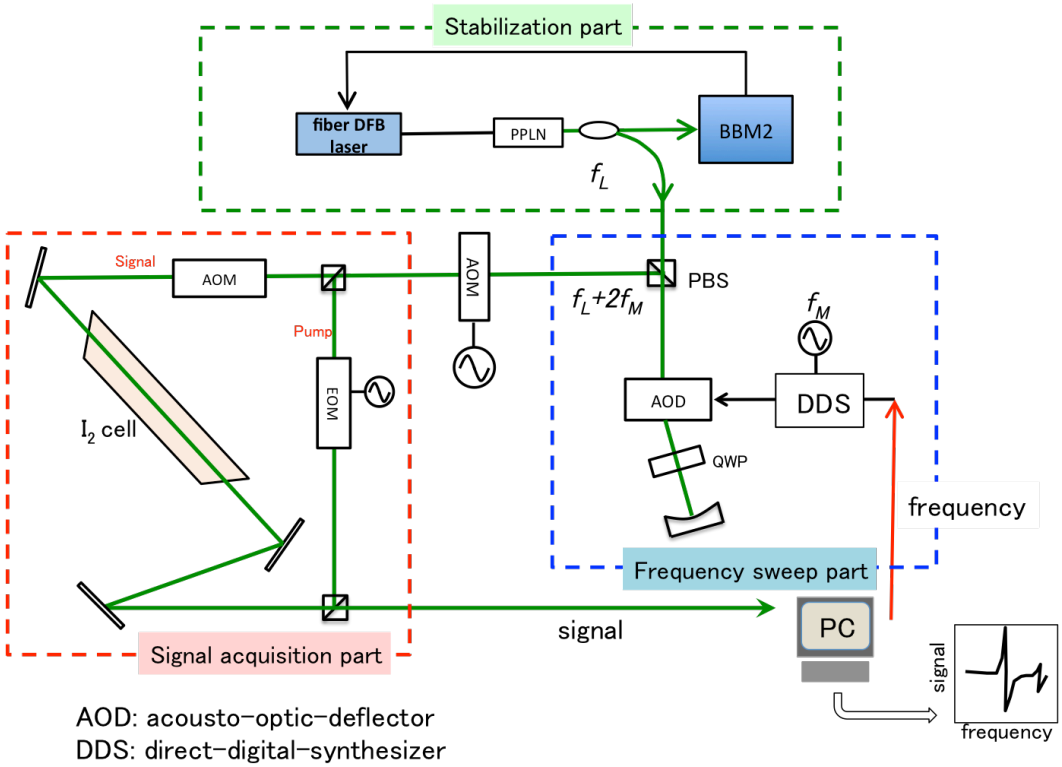

Figure 3.9. Schematic diagram of precision spectroscopy system

At the signal acquisition part, the introduced light is divided into the probe and the pump beam. In the same configuration as that of BBM, the pump beam is phase modulated by the EOM at 200 kHz, and the frequency

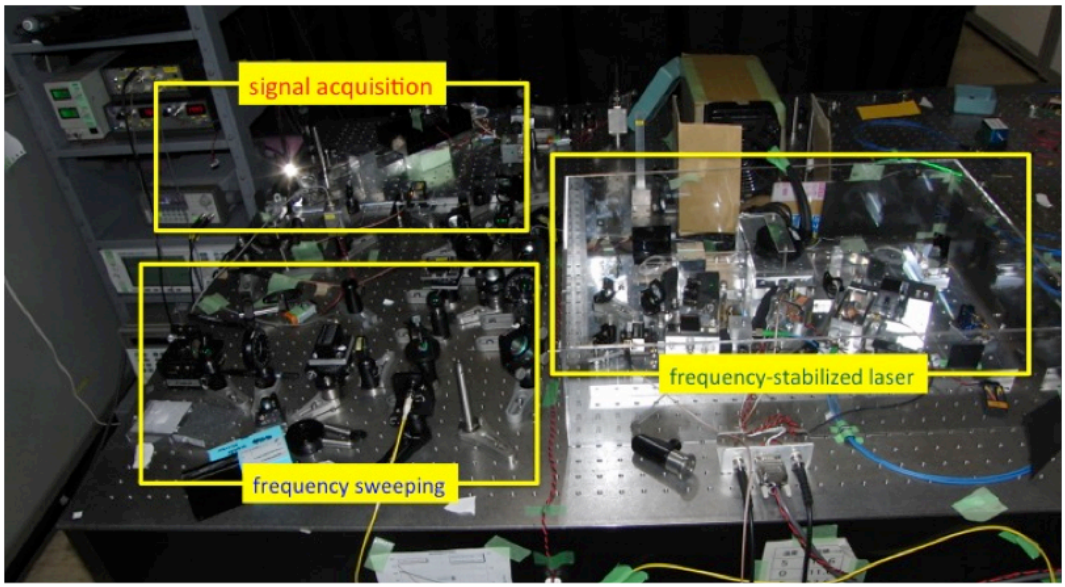

Figure 3.10. Picture of the precision spectroscopy system

of the signal beam is shifted by using another AOM. The probe and pump beams are collinearly counter propagated in another 400-mm-length iodine cell with 1-fold configuration to obtain the I_2-saturated absorption line. The signal beam is detected by a PD, and the saturated absorption signal and the sweeping frequency are synchronously recorded.

In our experiments, the I_2-cell used in BBM (stabilized part) is named I_2-cell-1, and another I_2-cell used in the signal acquisition part is named I_2-cell-2. Fig.3.11 shows I_2-saturated absorption line, the hyperfine components, a_{19}, a_{20}, a_{21} in the ro-vibrational transition of P29(43-0) which is obtained from the I_2-cell-2. In Fig.3.11, the frequency of the frequency stabilization part, the laser frequency is stabilized to the saturated absorption signal at the hyperfine components of a_{20}.

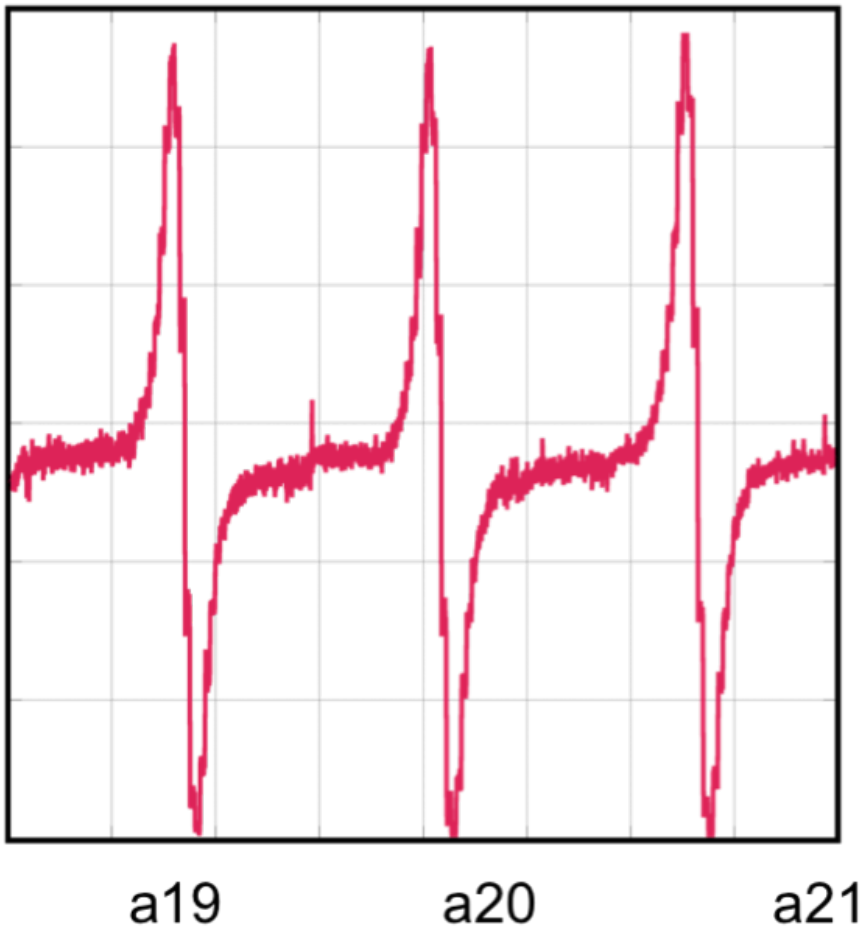

Figure 3.11. I_2-saturated absorption lines, the hyperfine components, a_{19}, a_{20}, a_{21} in the linear absorption line of P29(43-0) which is obtained from the I_2-cell-2

In Fig.3.12, the signals are obtained from the frequency stabilization part and the signal acquisition part (I_2-cell-1 and I_2-cell-2), respectively, and these signals are imported synchronously in the precision spectroscopy system. This experimental result indicates that the frequencies at the stabilized part and the signal acquisition part is identical which can be obtained from the frequency adjusting using AOMs.

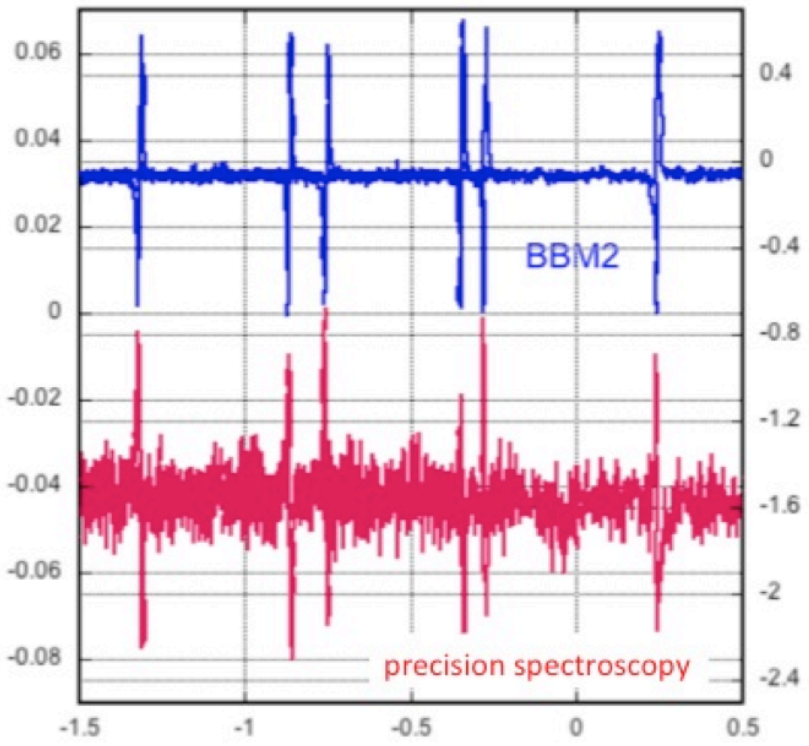

Figure 3.12. Iodine-absorption lines which are obtained from the frequency stabilization part and the signal acquisition part (I_2-cel-1 and I_2-cell-2), respectively

3.4.1 Pressure broadening of saturated absorption line

The saturated vapor pressure in the I_2 -glass cell can be controlled by varying the temperature at the finger of the cell, where the pressure of iodine gas is determined by the saturation vapor pressure. The mean-free pass of the iodine molecules is expected to be shorter as the saturated vapor pressure in the cell is increased, and hence, the linewidth of the saturated absorption signal increases linearly with the pressure caused from the collision-pressured broadening.

In this experiment, the saturated vapor pressure is controlled by using a two-stage Peltier element attached to the housing of the cell finger part, and the

pressure broadening of the saturated absorption signal is observed.
Fig.3.13 shows the pressure broadening of the I_2-saturated absorption lines which are obtained from our previous conventional spectroscopy system (BBM) and our current new precision spectroscopy system. The horizontal axis and the vertical axis indicate the pressure (Pa) of iodine gas and half width at half maximum (HWHM) (kHz) of linewidth, respectively.

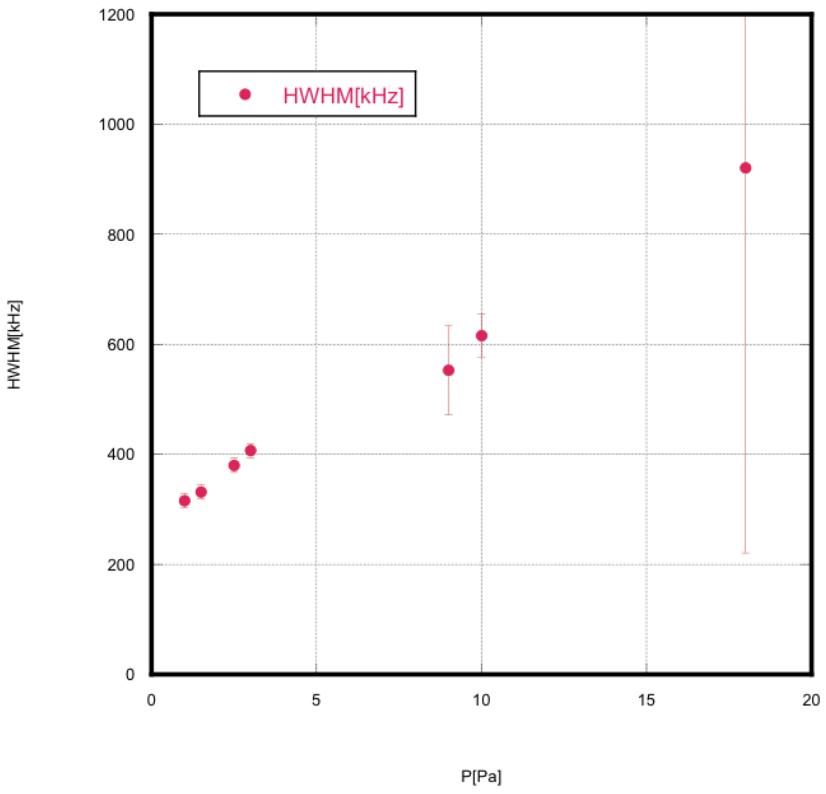

Figure 3.13. Pressure broadening of HWHM

In our conventional spectroscopy system, the uncertainly of the HWHM is the larger due to the frequency fluctuations of the light source, and the relation of the linewidth and the pressure is not linear. Since the laser frequency is stabilized and the linewidth of probe laser is narrowed, in the precision spectroscopy system, the linear relation is appeared. The fitting line of HWHM/pressure is 34.7 kHz/Pa. The large error bar in higher pres-

sure comes from week absorption signal intensity, which caused from low contrast between saturated absorption and the linear absorption line. In the case of 1 Pa in the I_2-glass cell-2 which corresponds to the temperature of -15 °C, the HWHM of I_2-saturated absorption line is 316 kHz, which is shown in Fig.3.14.

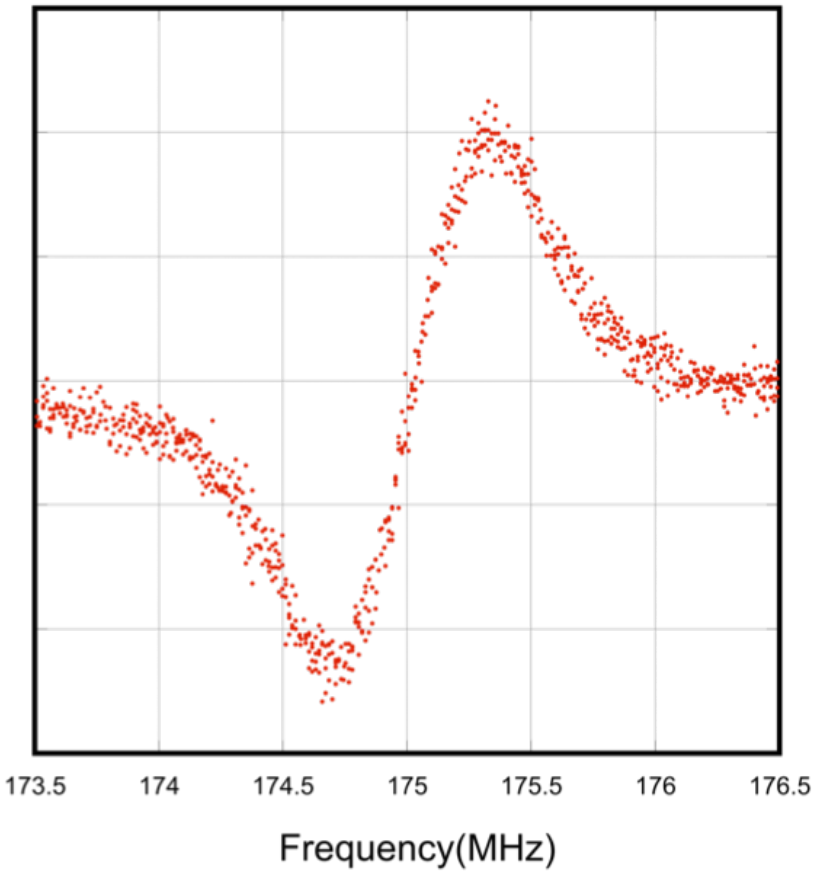

Figure 3.14. 1^{st} derivative of absorption line at 1Pa

Fig.3.15 shows the 1^{st} derivative of the saturated absorption lines which are obtained from I_2-glass cell-2 with the 400-mm interaction length (1 pass). The temperature in the I_2-cell is changed between -15 °C and 15 °C. The variation of the linewidth, shown in Fig.3.15, is observed. As the saturated pressure increases, the strength of the linear absorption line becomes stronger, and the signal contrast becomes weaker. Therefore, signal-to noise of the

saturated absorption line becomes lower as the temperature of the cell goes up.

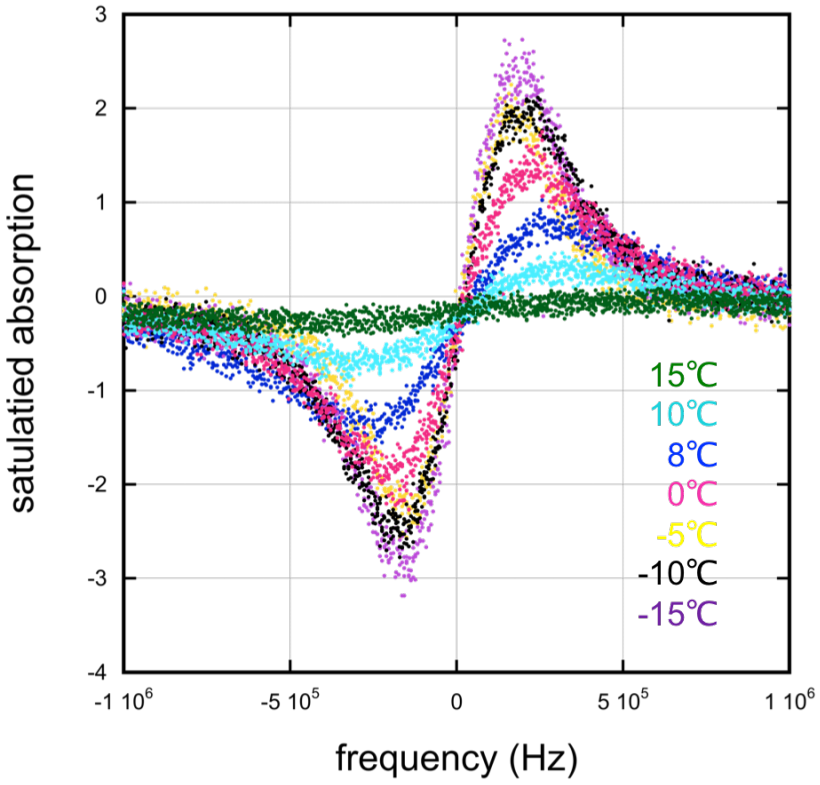

Figure 3.15. 1^{st} derivative of absorption line. The temperature in the I_2 cell is changed between -15 °C and 15 °C

Unfortunately, the pressure shift of the saturated absorption line cannot be observed in this time, because the amount of the pressure shift is too small to detect in our current spectroscopy system. It is demonstrated that the combination of the cooling of the I_2-cell for narrowing the linewidth, and longer interaction length (multi pass configuration) for increasing the signal strength would improve the SNR of I_2-saturated absorption lines.

3.4.2 Selection of transition

The wavelength of the fiber-DFB laser can be tuned continuously (without mode hop) for 0.8 nm from 1029.4 nm to 1030.2 nm by controlling the tem-

perature of the gain fiber. 70-linear absorption lines are observed in the tuning range of the second harmonics of the fiber DFB laser at 515 nm (0.4 nm), which is shown in Fig.3.16, and the saturated absorption lines at the linear absorption line are shown in Fig.3.16.
The linear absorption lines and the saturated absorption lines are obtained from BBM (I_2-cell-1) and precision spectroscopy system (I_2-cell-2), respectively. Some linear absorption lines are selected provisionally from the strong linear absorption lines, whose transitions are assigned from the center wavelength of the linear absorption line, as R81(46-0), R32(49-0), P29(43-0) by using the iodine frequency atlas [71]. The saturated absorption lines in the linear absorption lines are observed, whose linewidth are measured precisely. We obtain different HWHM of 410 kHz in R81(46-0), 401 kHz in R32(49-0) and 316 kHz in P29(43-0), which are the narrowest absorption lines in each linear absorption lines. Although it is hard work to define the highest SNR signal in all linear absorption lines a (more than 1600 lines), future thorough search of saturated absorption lines would determine the saturated absorption lines with highest SNR.

3.4.3 The hyperfine structure of the iodine absorption line

In the experiments by using our precision spectroscopy system, we find that the number of the I_2-saturated absorption lines in one linear absorption line is less than that measured in our previous spectroscopy system (BBM). In our previous research, the hyperfine structure of I_2 is clearly distinguish. Because we use free-running laser as a probe laser, and some linear absorption lines are closely located each other and are overlapped. We verify the number of the saturated absorption line at 1 linear absorption line by using our precision spectroscopy system. The obtained lines are shown in Fig.3.17 and Fig.3.18

In Fig.3.17, 42-saturated absorption lines are appeared in one linear absorption line. The blue line indicates the linear absorption profile at the wavelength of 515.0291 nm, and the red line indicates saturated absorption lines. In the case of P, 21-hyperfine components exist in one ro-vibrational transition. Referring the frequency atlas of iodine [71], there stays two ro-

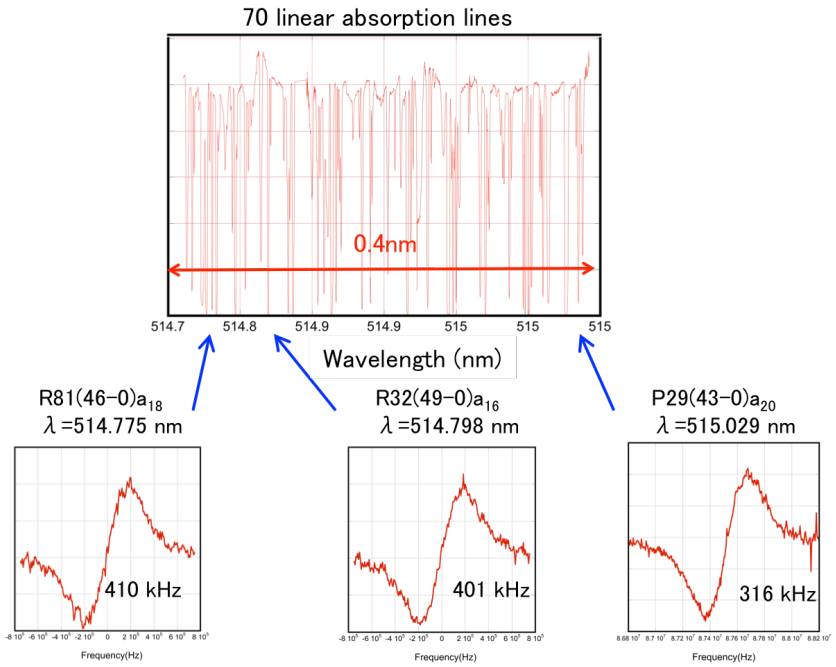

Figure 3.16. Linear absorption lines and saturated absorption lines

vibrational transition of P29(43-0) and P79(53-1) near 515.0291 nm, and Fig.3.17 shows the superposition of these linear absorption lines, which includes 42-saturated absorption lines. On the other hand, in the case of R, 15-hyperfine components exist in one ro-vibrational transition. In Fig.3.18, there is the linear absorption of R72(45-0), and the number of saturated absorption line (15) corresponds to the reference.

In order to obtain the presition line shape, the frequency modulation spectroscopy (FMS) is preferred to modulation transfer spectroscopy (MTS), because the modulation frequency of FMS is higher than that of MTS, and the presision structure of I_2-saturated absorption lines can be obtained [63]. According to [67], the linewidth of I_2-saturated absorption lines at 523-498 nm can be measured by MTS, and we have also used modulation transfer spectroscopy for obtaining 515-nm I_2-saturated absorption lines and evaluated the linewidth. Since we do not eliminate the power broadening effect, the measured linewidth is wider than that measured in previous work. How-

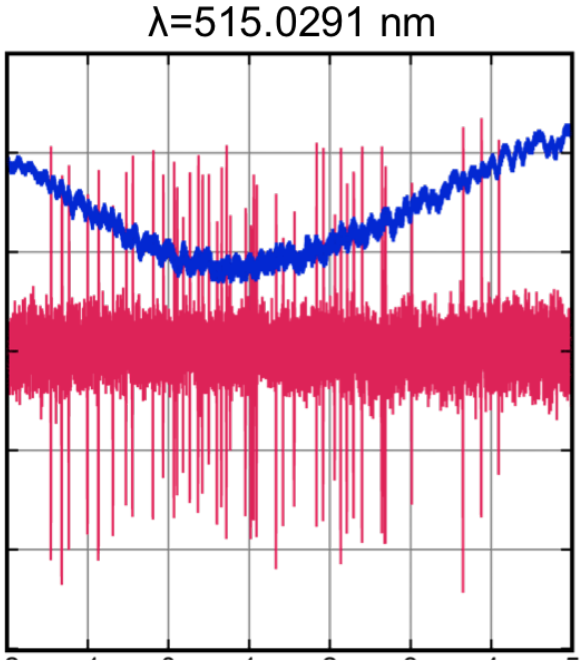

Figure 3.17. Linear absorption line of P29(43-0) and P79(53-1) near 515.0291 nm, and 42-saturated absorption lines.

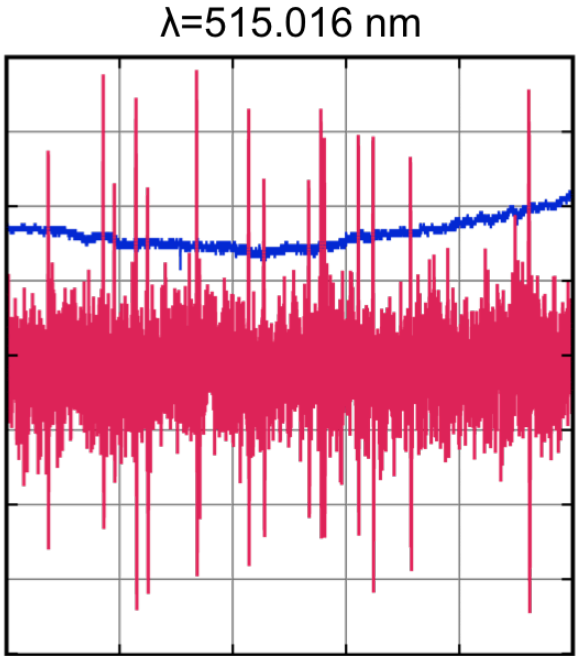

Figure 3.18. Linear absorption signal of R72(45-0), and 15-saturated absorption lines.

ever, our results are measured under actual experimental condition and are useful for estimating the SNR.

4 Development of iodine-stabilized lasers

4.1 Concept of breadboard model

Our light sources have been developed for operating in the spacecraft. Besides high frequency and intensity stability, our lasers also should have additional requirements as space-borne lasers such as compactness, high efficiency, robustness, high tolerance against mechanical vibrations, large temperature fluctuations and cosmic ray exposure, and the maintenance free long-term stable operation. For the prototype breadboard model, we have developed an iodine-stabilized lasers with taking into account that especially compactness, the high efficiency, long-term mechanical stability. The details are described in the following section. We have investigated the tolerance of all electrical and optical parts. Among them, one of the most serious problems is the radiation-darkening of Yb-doped fibers. Recently it is reported that the Yb-doped fibers with co-doping phosphor ions or injecting hydrogen shows the radiation hardening against cosmic ray exposure [72], [73]. The mechanical vibrations at the finger part of the iodine cell is also most serious problem and should be investigated in the future.

4.2 Experimental setup of BBM1 and BBM2

In this section, the details of the breadboard model (BBM) are described. Fig.4.1 is the schematic diagram of our BBM. The light source is a commercial Yb-doped fiber DFB laser (Koheras AdjusteK Y10 [74]) whose center wavelength and the output power are 1030 nm and 20 mW, respectively. The frequency control of the light source is obtained by using a piezo-electric transducer (PZT) attached to the gain fiber, whose control bandwidth is 10 kHz, and the wavelength can be widely tuned for more than 0.8 nm (240 GHz) without mode hopping by a temperature control of the fiber. Its mode-hop-free operation, frequency repeatability, robustness and tolerance against the mechanical vibrations are suitable for space-borne laser, and we chose it as a light source. I have developed an Yb-doped fiber amplifier to amplify the output power of the Yb:fiber DFB laser up to 200 mW. The amplified light is converted into 515 nm by using a ridge-waveguide periodically-polled

lithium niobate (WG-PPLN) crystal (NTT Electronics, WH-0515-000-A-C-C). The conversion efficiency of 26 % is obtained, and more than 46 mW of the second harmonics is generated from the fundamental light. The converted green light is introduced into the breadboard and is divided into the pump and probe beams, whose polarizations are S and P, respectively. The power divided ratio (pump: probe) of the green light is adjusted to 7:2 by using a half wave plate.

The pump beam is phase-modulated at 200 kHz by an electro-optic modulator (EOM) and frequency of the signal beam is shifted by an AOM to avoid the interference between the pump and probe beams. The pump and probe beams are collinearly counter propagated in an iodine cell. The length and the diameter of the iodine cell are 400 mm and 30 mm, respectively, and a Brewster windows are attached at both ends. The body of the glass cell is made by Mitorika, and I asked Dr. Jan Harabina at Institute of Scientific Instruments, Czech Academy of Science to fill the pure iodine into the cell [75]. The purity of the iodine is very severe for our study, and I once asked US company for filling iodine and the saturated absorption signal could not be observed from that US cell. The pump and signal beam is passing through the iodine cell, and multi-pass configuration makes long total interaction length of 2000 mm. Those signal acquisition part is mounted on a 500x350x20-mm aluminum breadboard. After propagating through the I_2-cell, the modulation-transferred signal beam is detected by a photo detector (PD), and is converted into the voltage signal. In order to obtain the frequency discrimination signal, the detected signal is demodulated at 200 kHz, which is the combination of Frequency modulation (FM) method and Modulation transfer (MT) method. The error signal is filtered and is fedback to a PZT driver for controlling the PZT-driven frequency actuator of the Yb:fiber DFB laser to stabilize the frequency of the laser.

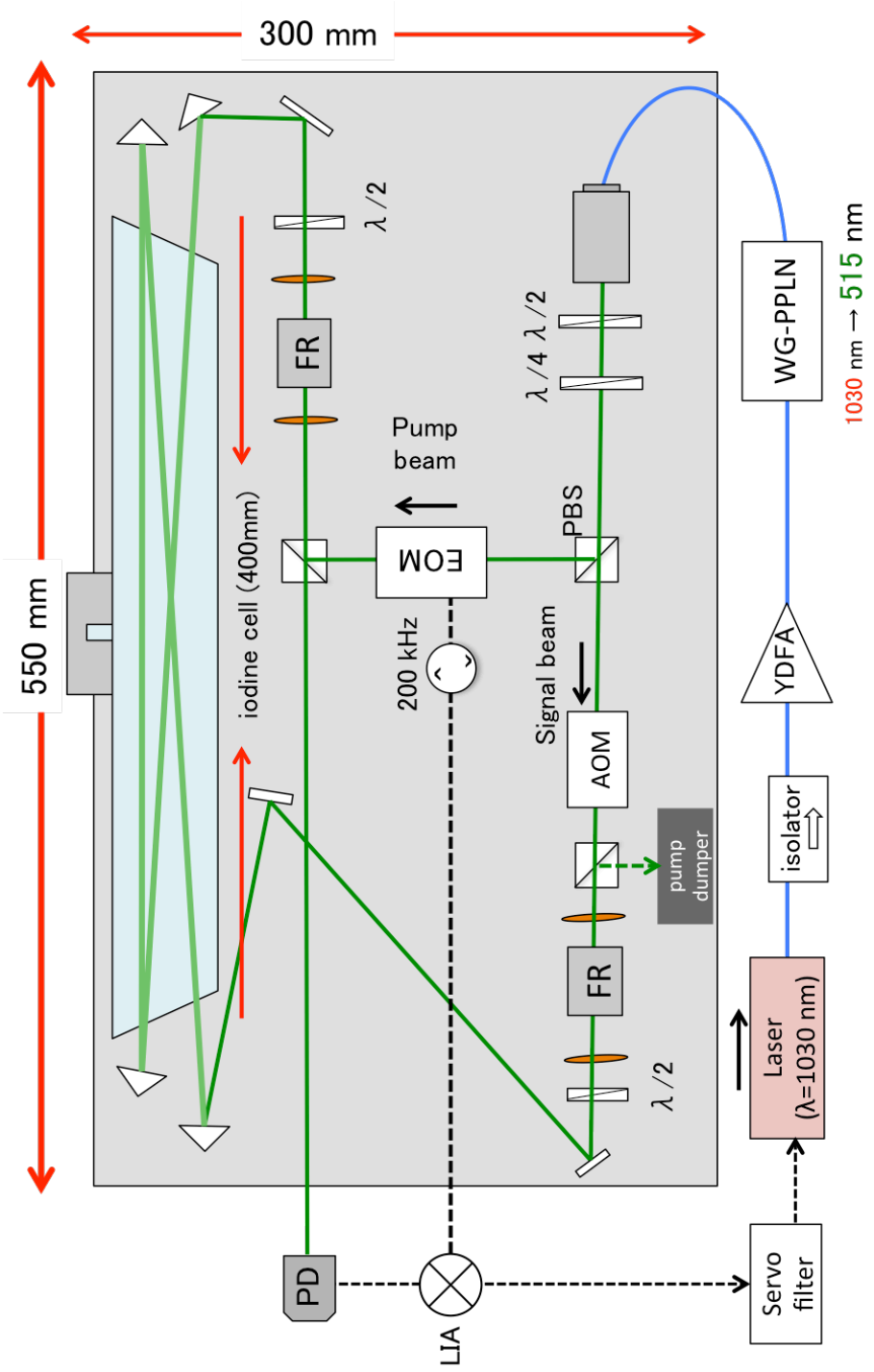

Figure 4.1. Schematic of BBM

Fig.4.2 is the first model of our BBM, which is called BBM1. During 3-years operation, BBM1 is improved for over 2 years (shown in Fig.4.3). The fiber components (inline PBS, inline AOM) are replaced with a bulk-type PBS and a free-space AOM to decrease the optical loss, and beam expanders that consists of a couple of the lenses are inserted into the probe and pump beam paths to suppress the transit time broadening. The number of beam folding in the iodine cell reduces from 5 times to 3 times to improve the contrast between saturated absorption and the linear absorption (Details are described at section 3.4). After development of BBM1, we have developed BBM2, whose configuration is the same as that of BBM1, for evaluating the absolute frequency stability of the lasers.

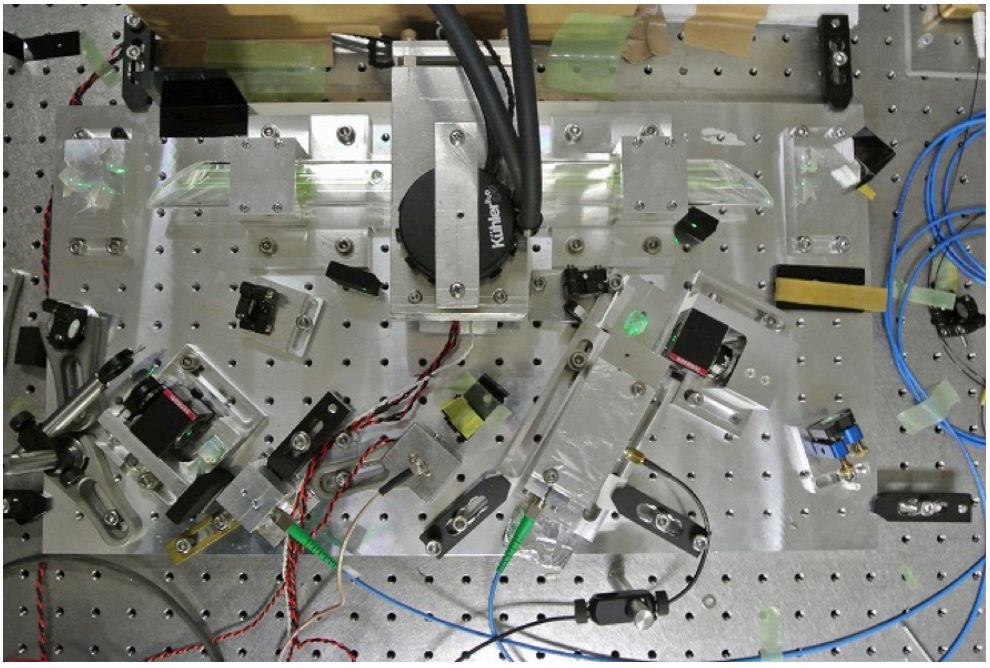

Figure 4.2. BBM1 (first model of BBM)

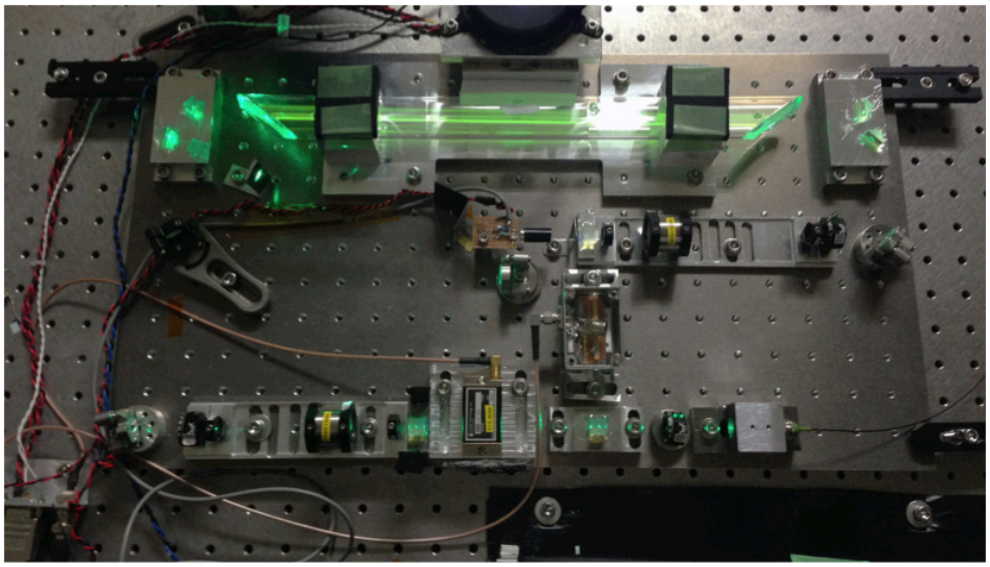

Figure 4.3. BBM2(Improved BBM)

4.3 The performance of the frequency-stabilized laser

In this section, the design of the servo system for the frequency stabilization is described. The open loop transfer function is written as $T_{open} = AG$, where G and A are the transfer function of the electrical servo filter and the other part including the optical detection part, frequency actuators. First, we determine the transfer function of the optical part A from the open loop AG; in the negative feedback loop which is shown in Fig.4.4, frequency is stabilized and the AG is measured.

The measured AG is shown in Fig.4.5. The blue traces and the red traces indicate the characteristics of the gain (left) and phase (right), respectively. The solid and the dashed lines indicate the measured and simulated AG, respectively. In this simulation, the characteristic of G is already identified and the equivalent circuit of A is identified as a quadratic integration circuit.

Total open loop transfer function of our servo system is simulated from the equivalent circuit (A) and the electrical servo filter (G) by using the electrical circuit simulator TINA-TI (Texas instrument Inc.)[76], and the

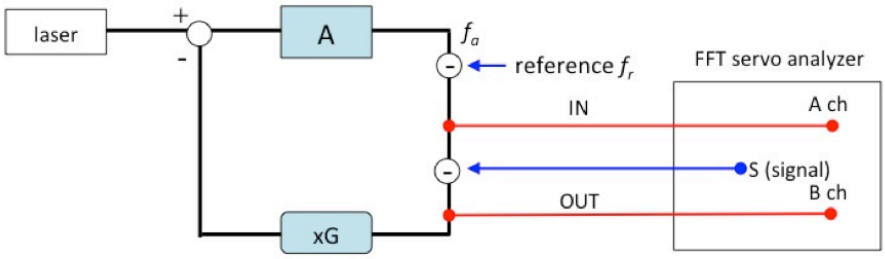

Figure 4.4. Schematic diagram for measurement of the open loop AG

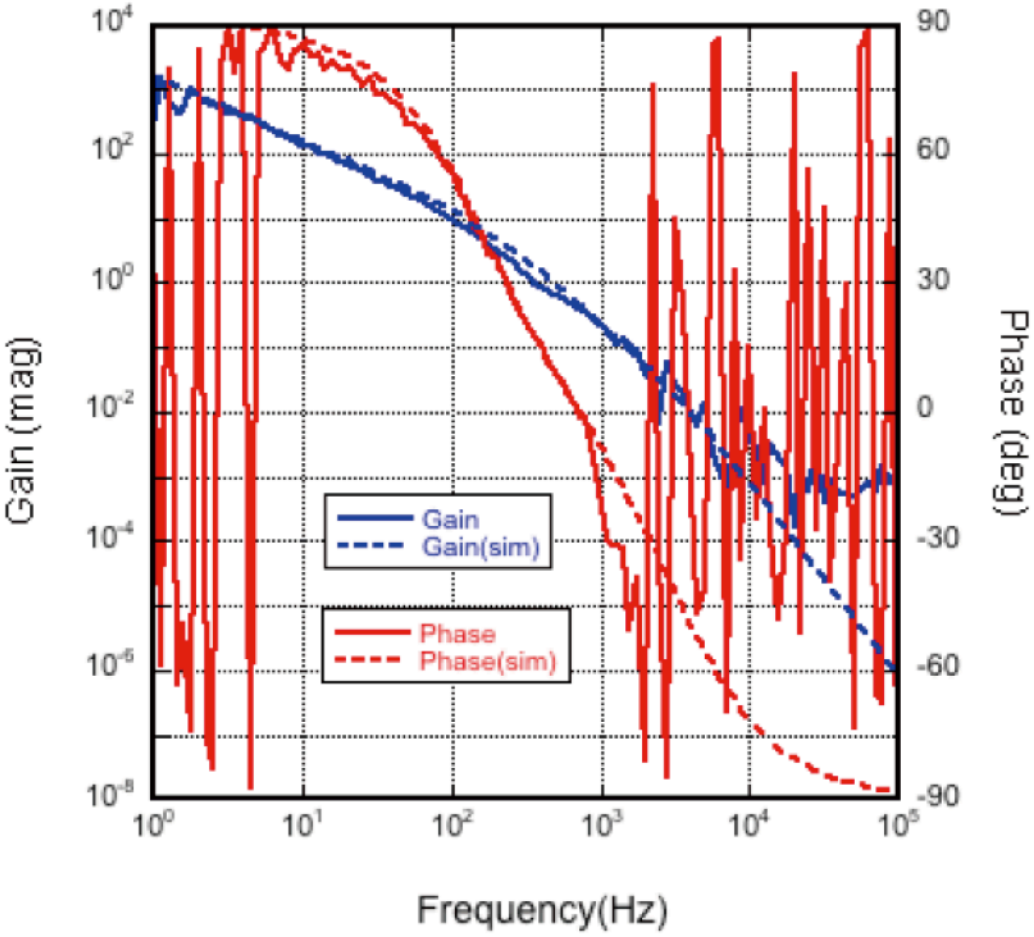

Figure 4.5. Measured total open loop transfer function T_{total}

improved AG for frequency stabilization is shown in Fig.4.6.
We obtain the gain of more than 150 dB at 1 Hz, the control bandwidth of 2 kHz (unity gain frequency), and the phase margin at 200 kHz is 50 degree, which are estimated from the total open loop transfer function $T_{open} = AG$. The equivalent circuit and the servo circuit for the frequency stabilization are shown in AppendixB.

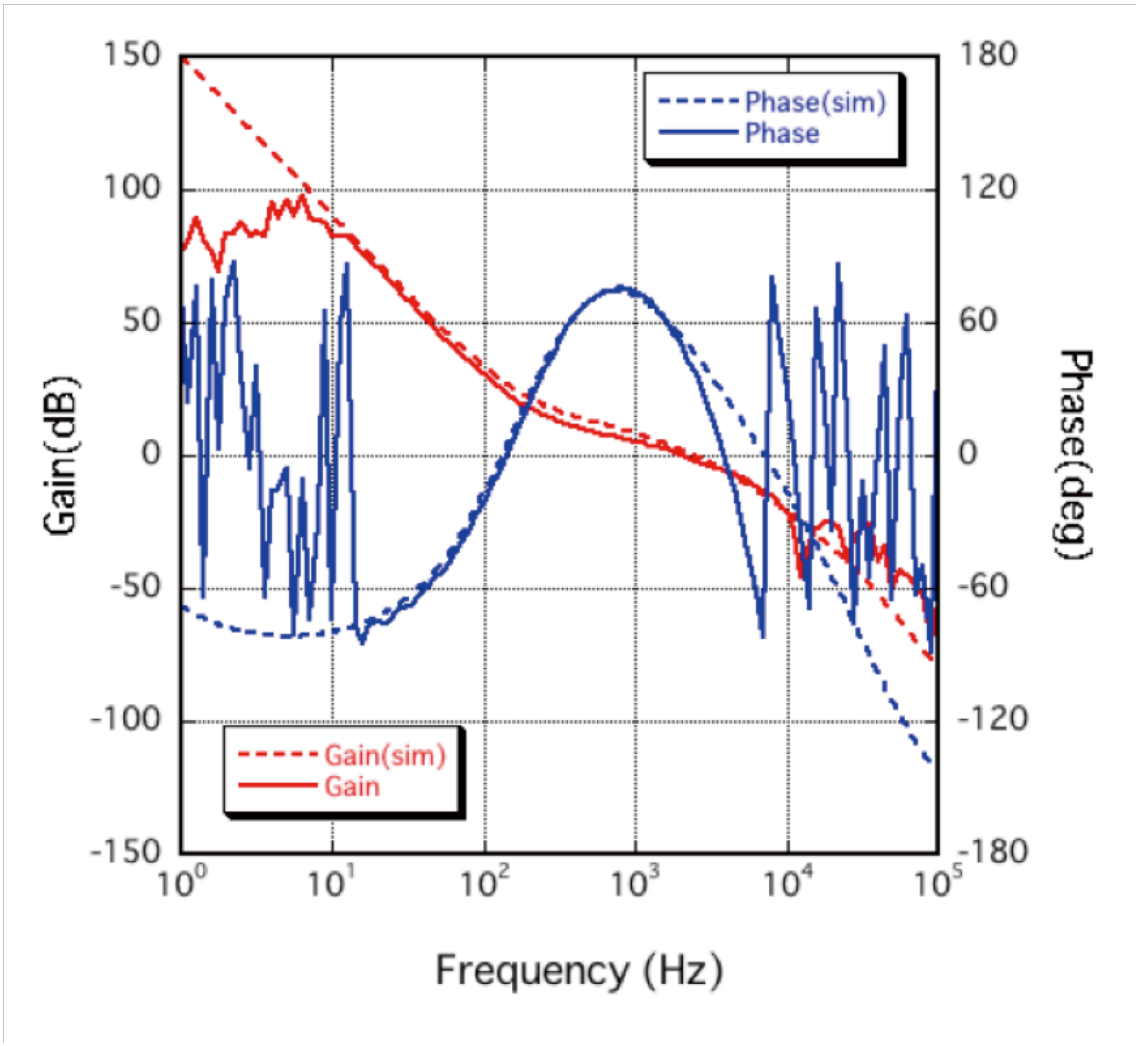

Figure 4.6. Simulated and measured total open loop transfer function Ttota (red: gain-left, blue: phase-right), measured (solid traces) and simulated by using equivalent circuit (dotted traces).

The frequency of the laser is stabilized in reference to a hyperfine component of I_2. Fig.4.7 shows the frequency noise spectra which are evaluated from the error signal (in-loop). In BBM1 (left), the red trace indicates the frequency noise of the laser at free-running state, and blue trace indicates that at stabilized state. The frequency noise was suppressed down to 1 $Hz/\sqrt{Hz}$ below 10 Hz, which satisfies the requirement level of DECIGO and B-DECIGO.

In BBM2 (right), the control servo bandwidth and servo gain at 1 Hz were 2 kHz and 120 dB, respectively. The blue trace indicates the frequency noise of the laser at stabilized state. The frequency noise was suppressed down to 1 $Hz/\sqrt{Hz}$ below 10 Hz. Although both frequency noise levels satisfy the requirement level DECIGO, these frequency noise are in-loop signal, and it means that the electrical servo system satisfies only the necessary condition of DECIGO requirement. As the absolute frequency noise is limited by the stability of the frequency reference, further precision out-of-loop evaluation is necessary and is described in the following section.

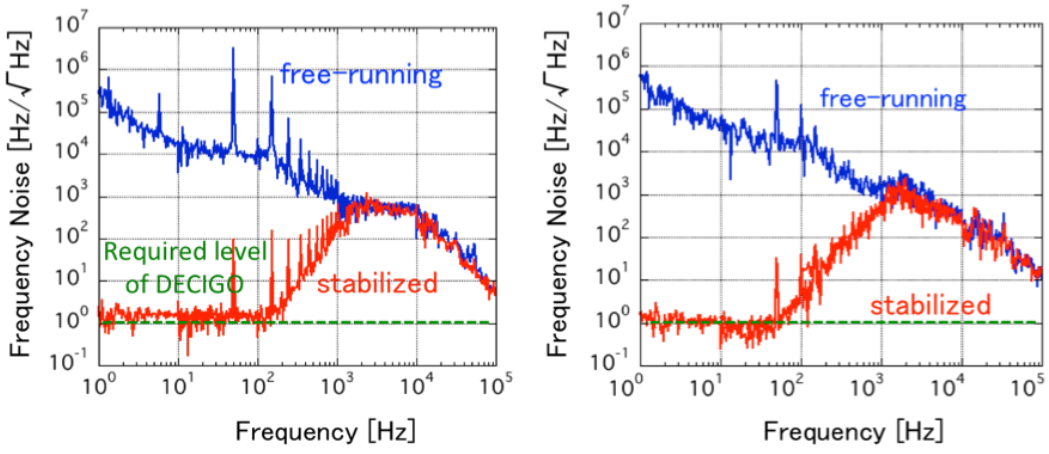

Figure 4.7. Frequency spectra evaluated from the error signal; the blue trace and the red trace indicate the frequency noise at free-running state and at the stabilized state, respectively. (the left is BBM1, the right is BBM2).

4.4 Evaluation of frequency stability

We also evaluate the absolute frequency noise including the stability of the frequency reference. The frequency of two BBMs are stabilized in reference to the same saturated absorption line. When the frequency of the signal beam is shifted at $+f$ by using AOM, the center frequency of the frequency-stabilized laser is shifted by $+(1/2)f$ from the center frequency of the absorption line. The signal beam at BBM1 and BBM2 are frequency shifted at +40 MHz and -40 MHz, respectively (both AOMs are driven from the same microwave source, and +1st and-1st diffraction light are used as each signal beam). Therefore, 40-MHz beat note at 1030 nm is obtained by mixing the frequency-stabilized light from two BBMs, and the absolute frequency is evaluated from the fluctuations of the beat frequency. Since the fluctuations of the AOM driving frequency give influence on the frequency stability of the laser, driving microwave signals (40 MHz) applied to each AOMs are supplied from a common micro wave synthesizer (Asilent E4432B) for cancelling the frequency fluctuations of the AOM driving frequencies, and the frequency of micro wave synthesizer is synchronized to a Rb atomic clock (Stanford Research PRS10). First, the long-term frequency stability is evaluated by measuring temporal variation of the beat note frequency by using a universal counter (Agilent 53132), which is shown in Fig.4.8

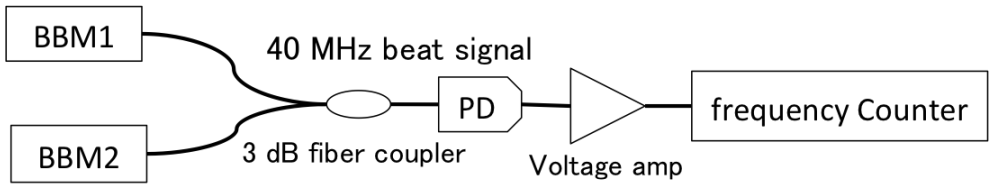

Figure 4.8. Schematic of the absolute frequency evaluation

The absolute frequency stability is measured in May 2017 whose results are shown in Fig.4.9. The green dots and the blue dots indicate Allan-deviation of the 40-MHz beat note frequency at free-running state and stabilized state, respectively. The frequency stability at 1 s and 4000 s are $df/f = 10^{-11}$ at stabilized state. The suppression of the scattering light

improves the frequency stability at the range of all averaging time, and the passive stabilization of EOM temperature decrease RAM (residual amplitude modulation) effect, which improves the long-term frequency stability. The improved frequency stability (measured in September 2017) is also shown in Fig.4.9 by red dots.

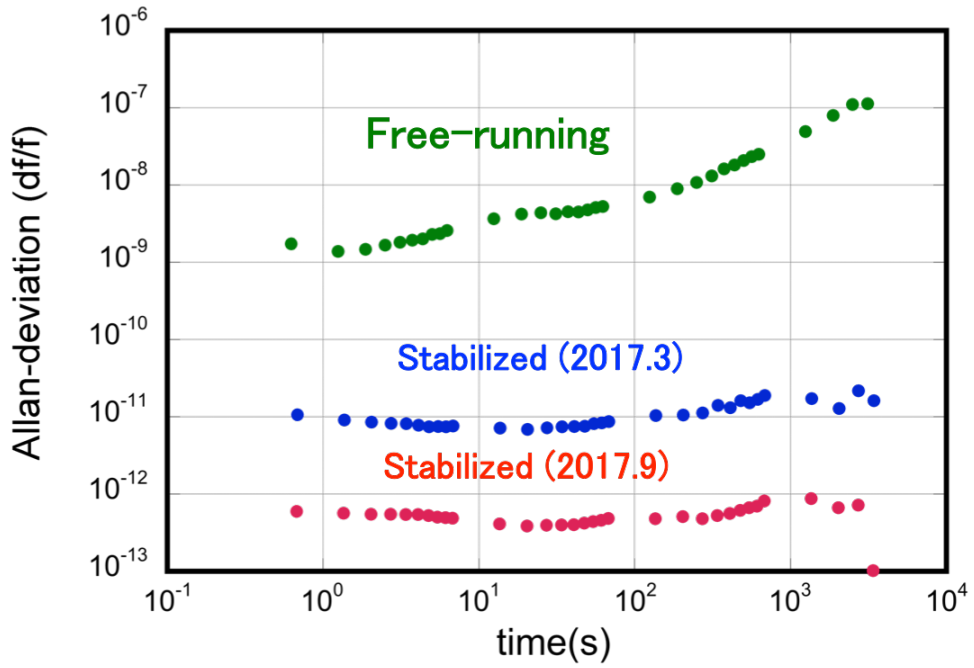

Figure 4.9. Allan-deviation of 40-MHz beat note between two lasers at free-running state (green dots), at stabilized state measured in March 2017 (blue dots) and September 2017 (red dots).

The further improvement of the frequency stability is observed in January 2018, which is shown in Fig.4.10, and the frequency stability reaches 10^{-14} level for longer than 2000 s. In these experiments, Allan deviation does not indicate the real frequency stability especially at short-term range (short averaging time) because of the miscounting of the frequency caused from the low SNR of the beat signal. Therefore, we try to evaluate the short-term frequency stability by using a signal analyzer (Anritsu MS2691A).

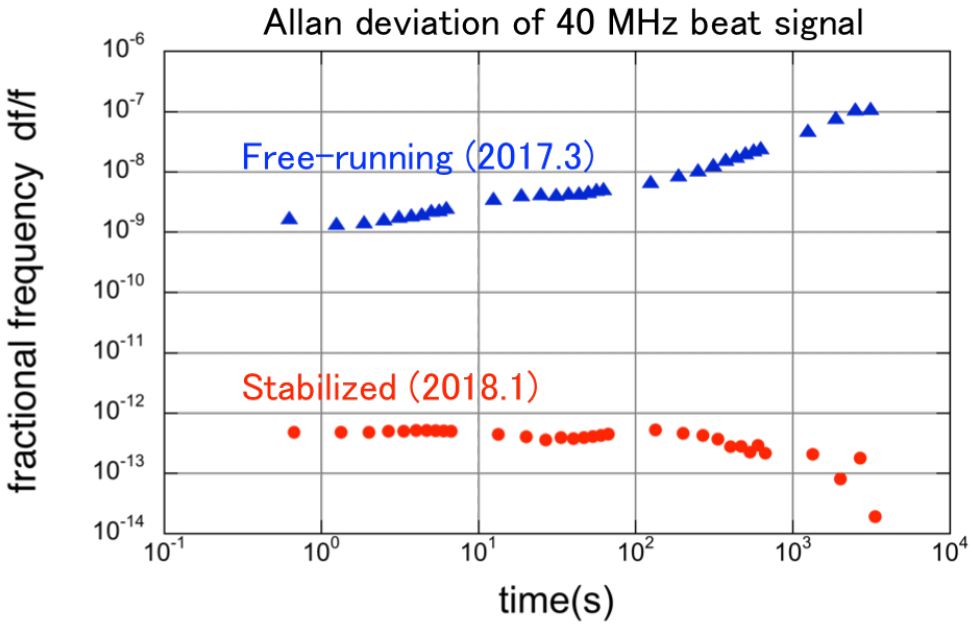

Figure 4.10. Allan deviation of the beat note frequency

The phase noise spectra of the beat signal are measured by using the signal analyzer, and the phase noise spectra of the beat signal is converted into the frequency noise spectra, which is shown in Fig.4.11. Above 500 Hz, the frequency noise spectra is the same as the in-loop frequency noise spectra shown in Fig.4.7, which means that it comes from the residual frequency noise of the frequency stabilized servo. On the other hand, below 500 Hz is flat.

Fig.4.12 shows the intensity noise of the frequency discrimination signal which is converted into frequency noise spectrum by using the slope of the frequency discrimination signal (red trace). And the in-loop frequency noise spectrum is added in this figure (black trace). As can be seen from Fig.4.11 and 4.12 , it is said that at the lower frequency range, the absolute frequency noise is limited by the SNR of the frequency discrimination signal, which reaches 5x10^1 $Hz/\sqrt{Hz}$. This frequency noise level is more than one order of magnitude worse than that of the requirement level, and further improvement would be obtained by improving SNR of the frequency discrimination signal.

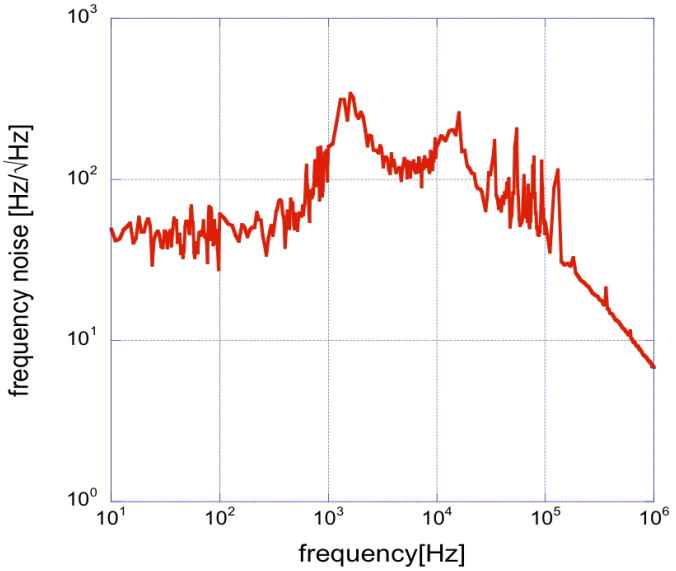

Figure 4.11. Absolute frequency noise spectrum of the frequency-stabilized laser which is evaluated from the beat note between two stabilized lasers, which reaches 50 Hz/$\sqrt{}$ Hz below 500 Hz.

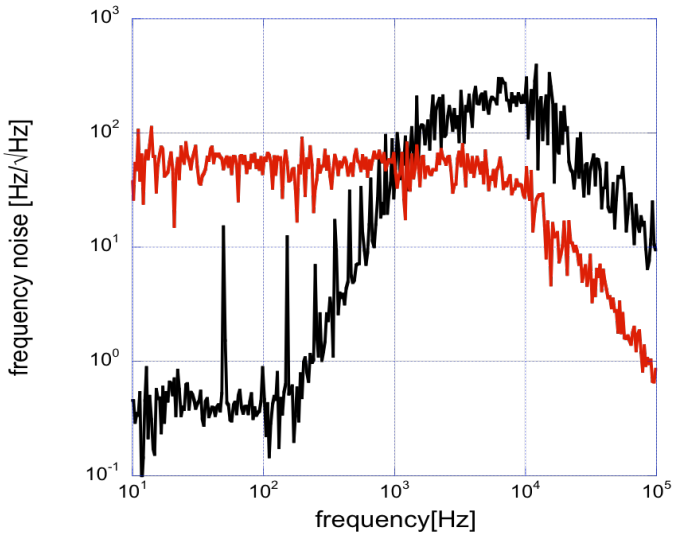

Figure 4.12. Frequency noise level from the noise of the signal which is converted from the intensity noise of the frequency discrimination signal [red]. Black trace indicates the in-loop frequency noise spectrum, and the absolute frequency noise [Fig.4.11] is sum of the SNR and residual frequency noise of the laser.

5 Improvement of the short-term frequency stability

5.1 Intensity stabilization at modulation frequency of 200 kHz

The short-term frequency stability of the laser is limited by the SNR of the frequency reference. We obtain the frequency discrimination signal of the saturated absorption signal by using lock-in detection. The frequency discrimination signal is used as a frequency reference, and whose noise level is limited by the intensity noise of the PD detected signal at the phase modulation frequency. The measured relative intensity noise (RIN) spectra of the light sources (fiber DFB laser, ECLD1, ECLD2) are shown in Fig.5.1.

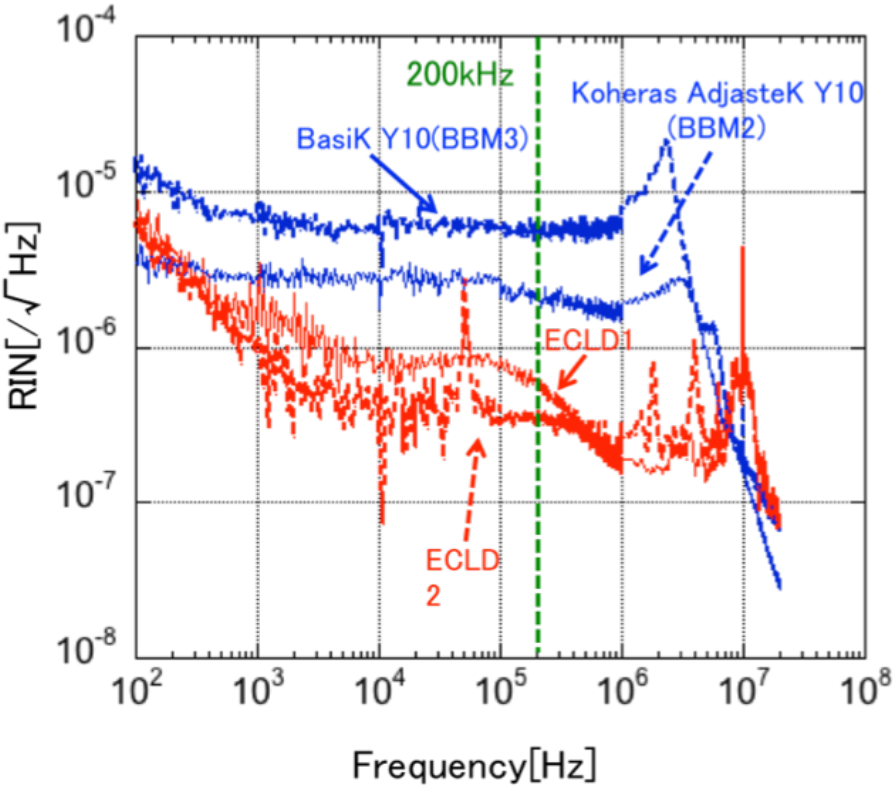

Figure 5.1. RIN of the fiber DFB laser, ECLD1 and ECLD2

In our experiments, the phase modulation frequency is 200 kHz, which is optimized for obtaining strong frequency discrimination signal by using the modulation transfer method. The RIN of the Yb:fiber DFB laser at 200 kHz is much worse than that of the theoretical limit: photon shot noise level which reaches $dI/I = 10^{-8}/\sqrt{Hz}$ level at the detection power of 7 mW, and dominates the intensity noise of the PD detected signal at 200 kHz.
Therefore if the intensity noise of the laser at 200 kHz is suppressed, the SNR of the frequency discrimination signal would be improved, which results in the improvement of the frequency stability. On the other hand, the intensity noise of ECLD at 200 kHz is lower than that of fiber DFB laser, however the mechanical stability of ECLD is much worse than that of fiber DFB laser. Therefore, we choose more stable fiber DFB laser, and have tried intensity stabilization at 200 kHz for improving the SNR of the frequency reference. As is mentioned in the previous section, the absolute frequency stability of our iodine-stabilized laser is limited by SNR of the frequency discrimination signal, and hence, we try to suppress the intensity noise of the laser at 200 kHz for improving the absolute frequency noise of the frequency-stabilized laser around 1 Hz.
The intensity stabilization of the laser at 200 kHz is not so easy because 200 kHz is too high for obtaining enough high noise suppression gain from the feedback control loop. In the first step, we try the active intensity stabilization of the laser at 200 kHz by the feedback method, in which AOM is used as a power actuator.

5.1.1 Intensity stabilization at 200 kHz (normal feed back)

Fig.5.2 is the schematic diagram of the active intensity stabilization of the laser at 200 kHz. After the signal beam in BBM is passing through the AOM, 1^{st} order diffraction light from the AOM is picked off by the mirror in front of the iodine cell. A portion of the 1^{st} order light is detected by PD, and the detected intensity noise signal is filtered into the control signal by the electric servo circuit.
We use a micro wave frequency synthesizer for generating 80-MHz signal for driving AOM (Agilent E4432B). The signal from the a micro wave synthesizer

is amplified by using a microwave power amplifier up to 1W, and the control signal is applied to a voltage-controlled attenuator (VCATT) located before the power amplifier to modulate the applied micro wave power to the AOM. By choosing appropriate power range, the diffraction efficiency of the AOM is proportional to the applied micro wave power, and we can control the intensity of 1^{st} order diffraction light by the control signal.

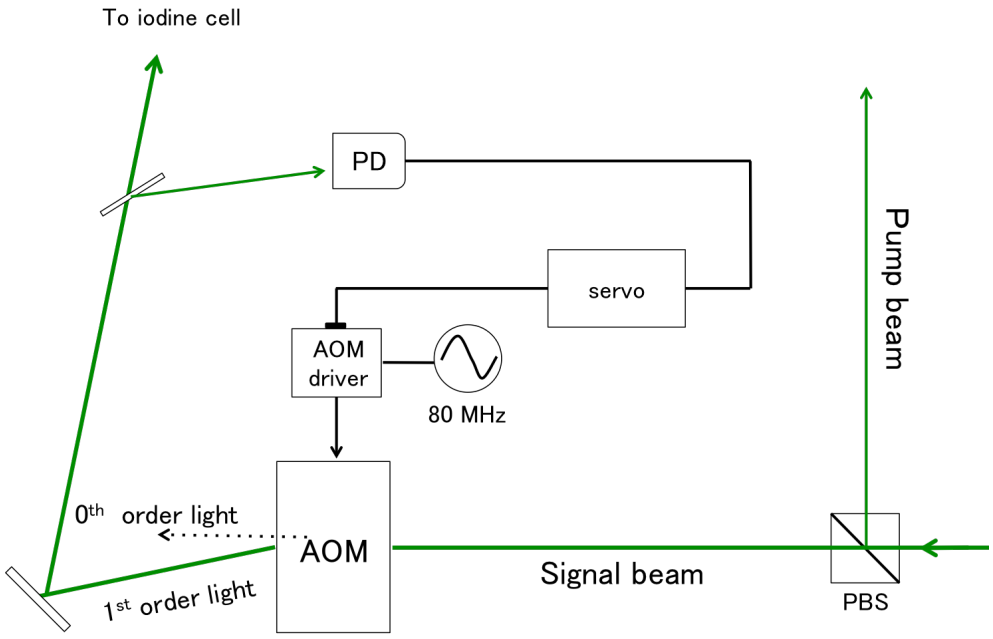

Figure 5.2. Schematic diagram of the active intensity stabilization by using feedback method. AOM driver consist of a voltage-controlled actuator and a power amplifier, and the output power can be controlled by using the applied control signal

Fig.5.3 shows the transfer function of the power actuators from voltage modulation to optical power modulation. I evaluated the transfer function of several commercial voltage controlled attenuators (VCATT), RVA2500, ZFL-1200, ZX73 (Mini-Circuit Inc.), and the commercial AOM driver with a power modulation input (AOMO-125, Crystal Technology Inc.). Among them, the commercial AOM driver is most suitable for intensity stabilization, due to the low phase delay at 200 kHz, although micro wave synthesizer-driven signal source has better frequency stability. In order to make fast feedback loop, the transfer function of operation amplifiers (Op-Amps.) are

measured, which is shown in Fig.5.4. Since the phase margin and the gain of AD829 (Analog devices Inc.) is lager than that of OP27 (Analog devices Inc.) at 200 kHz, we choose AD829 for the electric servo filter. The circuit diagram is shown in Appendix C.

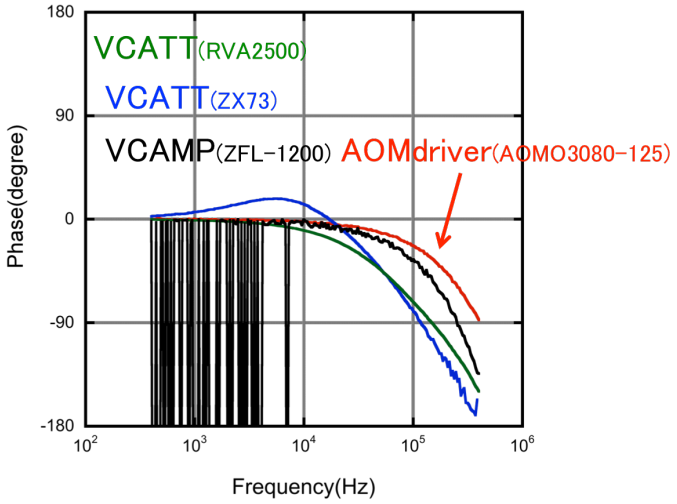

Figure 5.3. Transfer function of the AOM diver and voltage control attenuators (VCATT). Compared with VCATT, the AOM driver shows less phase delay at 200 kHz.

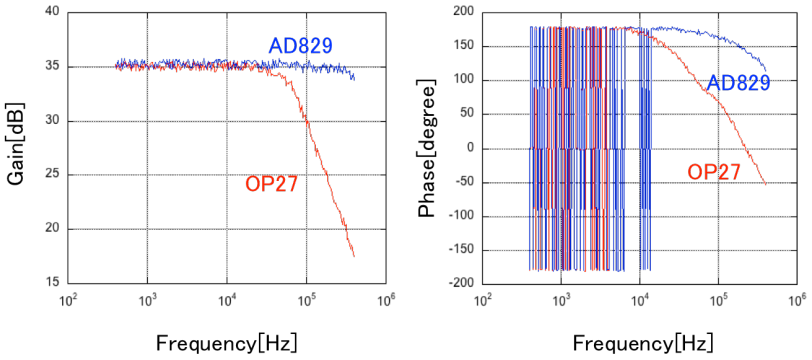

Figure 5.4. Transfer function of the operational amplifier (OP27, AD829)

5.1.2 Experimental result (normal feed back)

The RIN spectra of the signal beam (λ =515 nm) are shown in Fig.5.5. The RIN below 100 kHz is measured by using an FFT analyzer (Advantenst Inc. R9211C), and above 100 kHz is measured by using another wideband FFT analyzer (Yokogawa Inc. SA2400).
The control bandwidth of the intensity stabilization is around 500 kHz which is limited by the control bandwidth of AOM, and the RIN at 200 kHz is suppressed down to 6 dB.

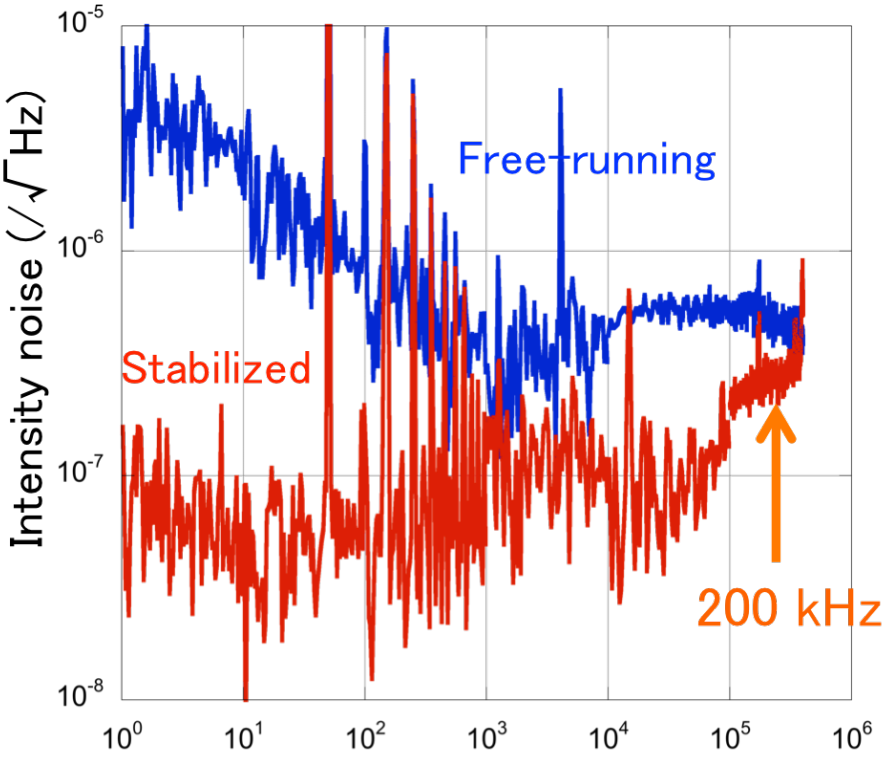

Figure 5.5. RIN of the signal beam at the free-running state (blue) and the stabilized state (red)

As can be seen from the figure, the intensity noise at 200 kHz is suppressed. However the significant improvement cannot be achieved because of its low servo gain at 200 kHz due to the limited control bandwidth.

5.1.3 Intensity stabilization at 200 kHz (forced oscillation)

In order to improve those problems, we have tried another new active intensity stabilization method at 200 kHz. Fig.5.6 shows the schematic diagram of the experimental setup for the intensity stabilization at 200 kHz.

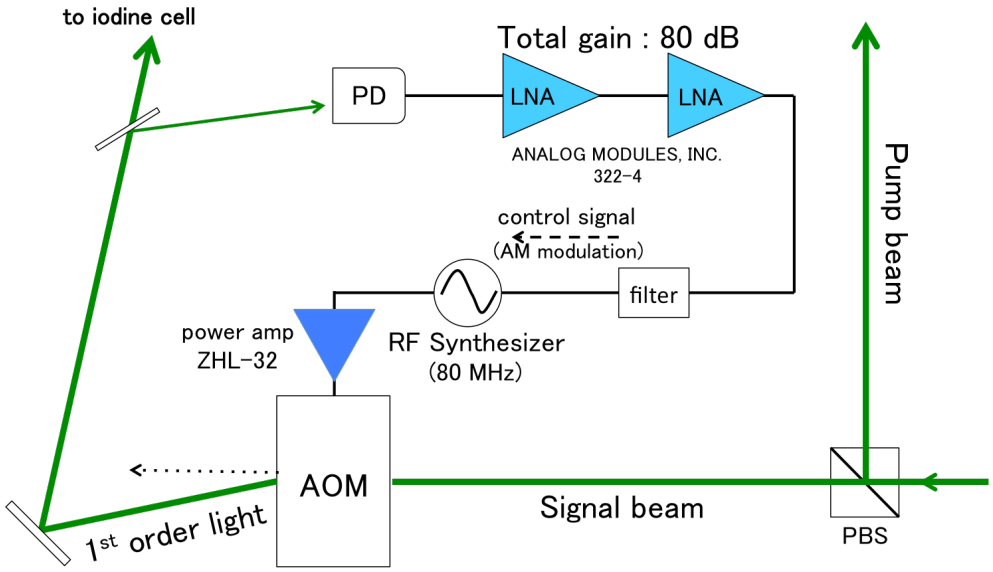

Figure 5.6. Schematic of the intensity stabilization at 200 kHz by using low noise amplifier (LNA)

The intensity noise at 200 kHz is negatively fedback by using two-stage cascade-connected low-noise AC amplifiers (LNA). The LNAs used for this stabilization are ANALOG MODULES. Inc. 322-4, and the total gain at 200 kHz is 80 dB. A portion of the 1st order light is detected by PD and the detected voltage signal is amplified by two LNAs. After amplified, the control signal is directly applied to the AM wideband modulation terminal of the micro wave synthesizer (Agilent E4432B) without servo filter.

5.1.4 Experimental result (self-oscillation)

The RIN spectra are shown in Fig.5.7. The RIN at 800 kHz is forced to oscillate by feedback control from the phase delay of more than 180 degree

at the unity gain frequency. Though this scheme does not follow the normal feedback theory, RIN at 200 kHz is successfully suppressed because this oscillation absorbs the intensity noise around the oscillation frequency. The demodulated intensity noise of the frequency discrimination signal is also measured which is shown in Fig.5.8.

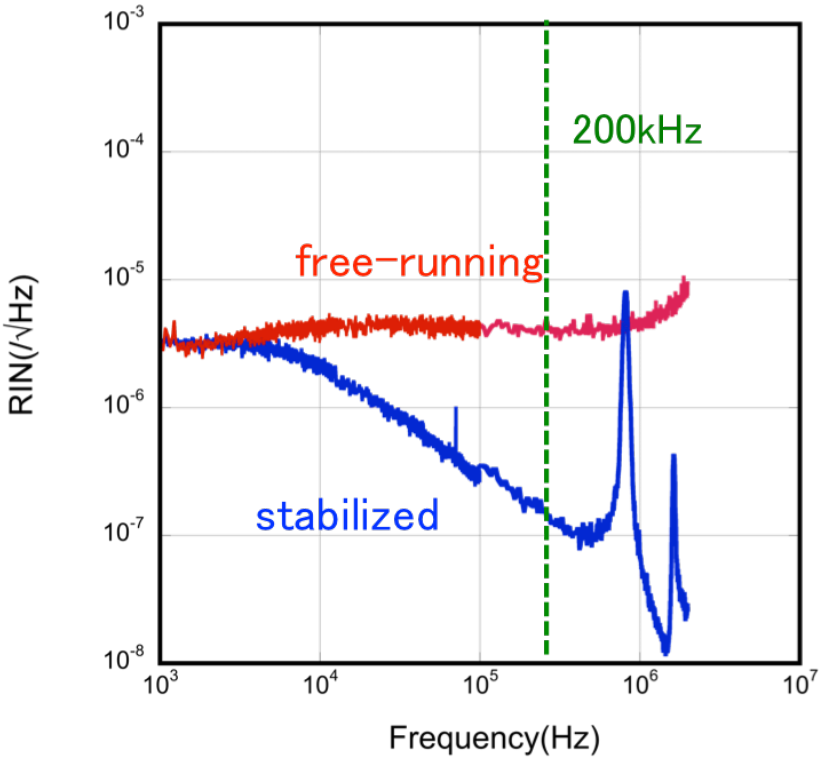

Figure 5.7. RIN spectrum; the blue and the red lines indicate the stabilized state and free-running state, respectively. At 800 kHz the servo system is oscillated, and the intensity noise suppression around this oscillation peak is observed.

The blue line and the red line indicate the stabilized state and free-running state, respectively, and the intensity noise at demodulated signal is suppressed by 20 dB up to 100 kHz. The corner frequency of 1 kHz comes from the low-pass filter in the lock-in amplifier.

The steep peak appeared at 200 kHz is the down-converted oscillation peak in the intensity noise spectrum.

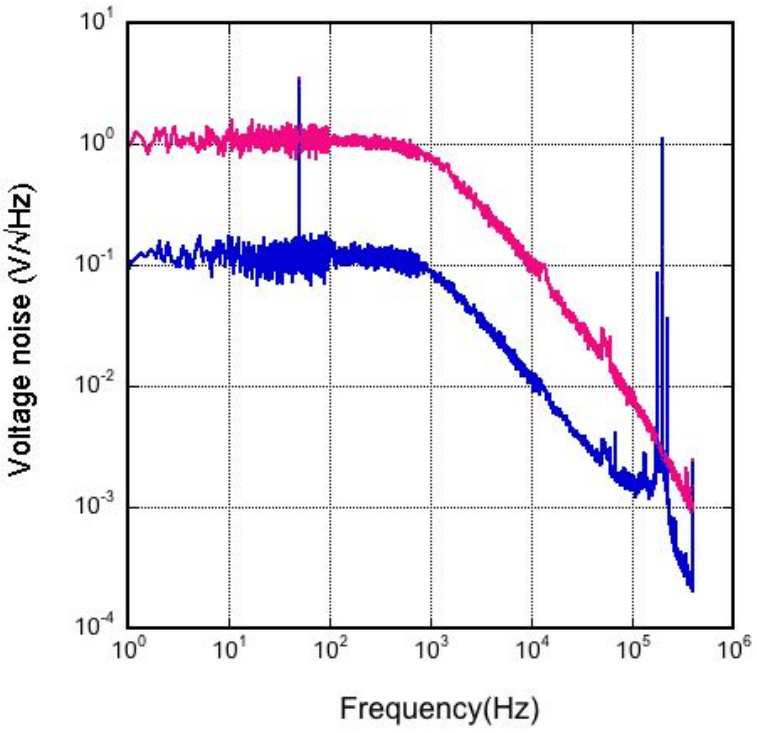

Figure 5.8. Demodulated RIN spectrum; the blue and the red lines indicate the stabilized state and free-running state, respectively.

As is seen from Fig.5.8, the noise level of the demodulated signal is successfully suppressed. However, the signal strength of the frequency discrimination signals is also decreased, and hence, the SNR of the frequency discrimination signal cannot be improved. We first try to apply this oscillation control method to the intensity noise suppression, and the intensity noise of the demodulated signal is successfully suppressed. However we do not fully understand the mechanism of signal decreasing yet, and further investigation is required for realizing these phenomena.

Following those experimental results, we have tried another way to decrease the intensity noise of the laser with keeping the signal strength of the frequency discrimination signal which are described in next subchapter.

5.1.5 Intensity stabilization at 200 kHz (feed forward)

We also try the intensity stabilization at 200 kHz by using feed forward method. Compared with feedback method, feed forward cannot obtain large noise suppression gain. In feed forward control, the servo bandwidth is not limited by the phase delay or mechanical resonance of the loop, and no resonant oscillation is occurred during servo control. Therefore, the feed forward loop can be obtained by only adjusting the gain and phase of the loop, and no precision and complex filter design are necessary. Fig.5.9 shows the schematic diagram of the intensity stabilization of feed forward method. For the intensity stabilization, AOM which is inserted in the signal beam path, is used for the intensity actuator.

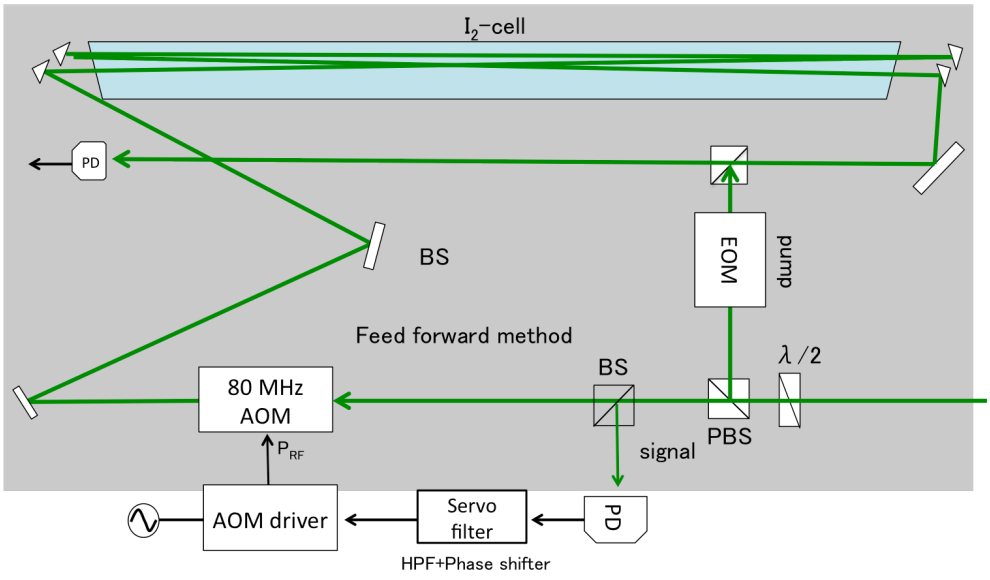

Figure 5.9. Schematic diagram of intensity stabilization at 200 kHz by feed forward method

A part of the signal beam is picked off by a non-polarized beam split-

ter (NBS), and the detected intensity noise is filtered and is applied to the AOM located next to NBS for suppressing the intensity noise at 200 kHz. For optimizing the suppression of the intensity noise by using feed forward method, the gain of the loop should be adjusted precisely unity at the suppression point. The gain of the loop is precisely controlled by the electrical attenuator consisted of a multi-turn potentiometer.
And phase of the feedback signal should be also adjusted to $(2n+1)\pi$ radian for negative feed forward. The phase of the control signal is controlled by using a hand-made electric phase shifter, whose circuit diagram is shown in Appendix **??**. Transfer function of the phase shifter is shown in Fig.5.10.

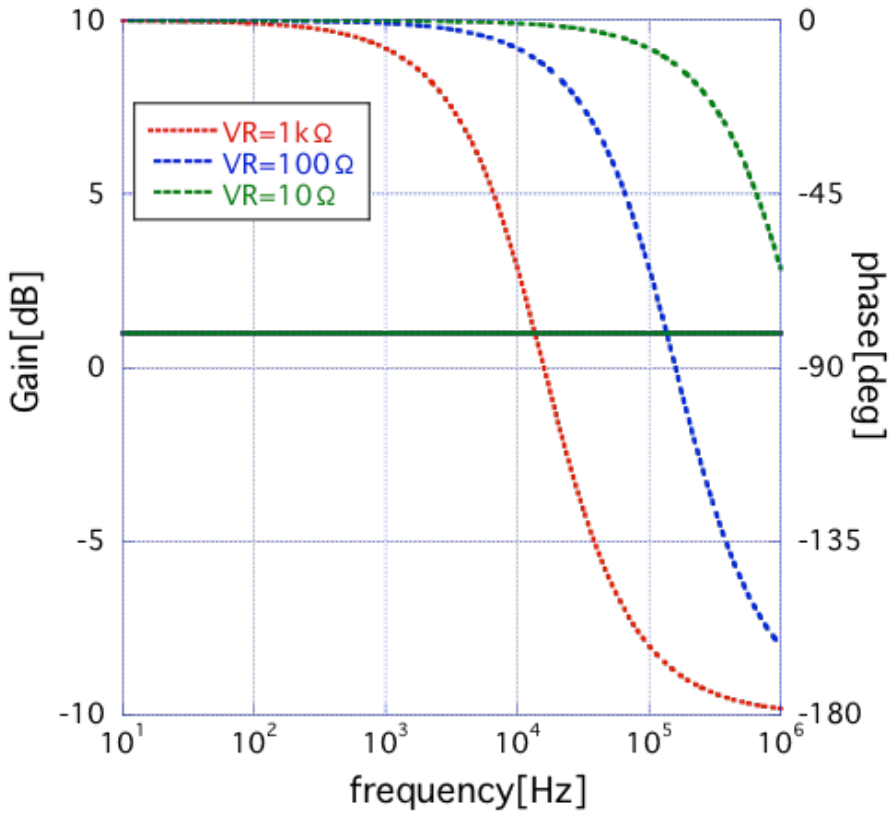

Figure 5.10. Transfer function of the two stage phase shifter

Solid traces and dashed traces in Fig.5.10 indicate gain (left) and phase (right), respectively. Increasing the resistance of a 1-kΩ variable resister

(VR1k) as 10Ω (green) 100Ω (blue), 1kΩ (red) result in the phase delay of the transfer function without gain variation. Therefore the phase at 200 kHz can be adjusted from -20 degree to -160 degree by changing the resistance of VR1k. Fig.5.11 shows the gain (solid trace, left) and phase (dashed trace, right) of our hand made phase-shifter under the maximum phase shifted condition. The blue traces indicate transfer function of one phase shifter, and maximum phase at 200 kHz (red bar) is -100 deg, which is insufficient for adjusting the phase to -180 degree. Therefore we use two-stage cascaded phase shifter (red traces) whose maximum phase shift -430 degree, and can be adjusted to -180 degree.

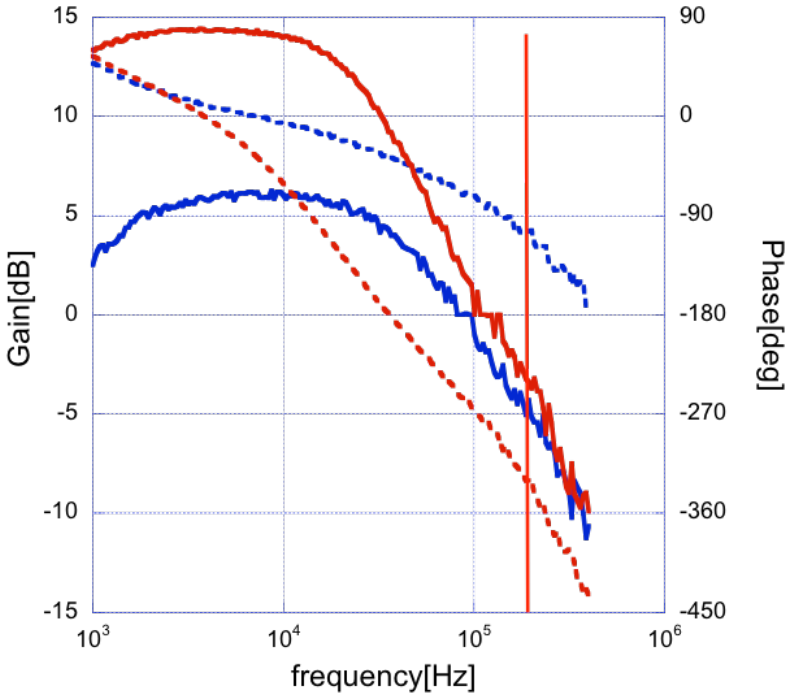

Figure 5.11. Measured open loop transfer function of our hand-made phase shifter. The solid and dashed traces indicate gain and phase, respectively, and blue lines represent those of 1 phase shifter, and red lines represent those of 2-stage phase shifter. Red bar indicates the frequency at 200 kHz.

5.1.6 Experimental result (feed forward)

The relative intensity noise spectra of the laser are shown in Fig.5.12. The intensity noise is measured by the wideband FFT analyzer (Yokogawa Inc. SA2400) and is successfully suppressed by 10 dB at 200 kHz. RIN at free-running state (black trace) is suppressed by feed forward servo without phase shifter, which is indicate by green trace. In that case, although RIN around 10 kHz is suppressed, that at 200 kHz is still the same level. As the phase of the control signal is shifted by our two-stage phase shifter, the noise suppression peak is increasing (blue trace), and by adjusting the phase appropriately, the RIN at 200 kHz is suppressed by more than 15 dB.

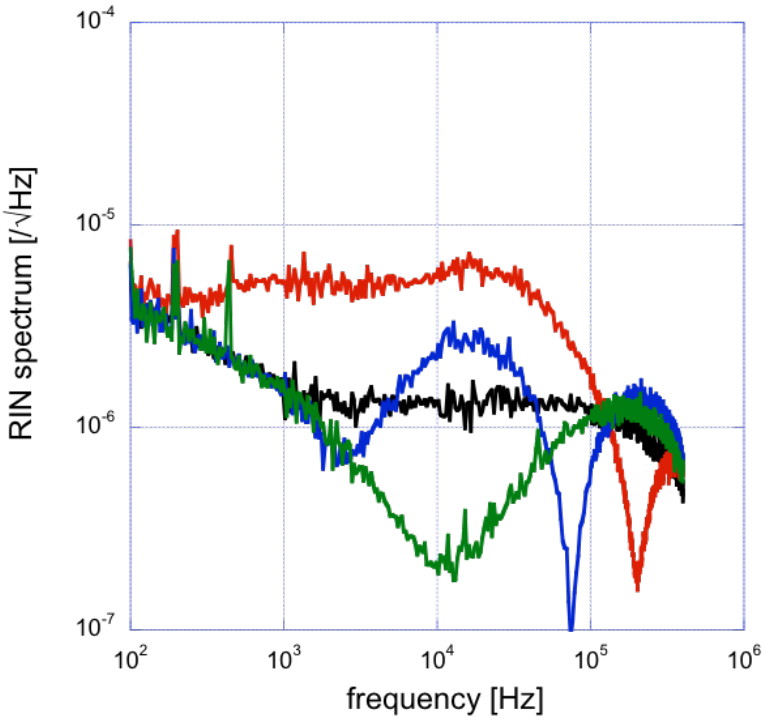

Figure 5.12. Intensity noise spectra of the laser at feed forward control; free running (black), and feed forward controlled as the shifted phase is increasing (green to blue), and at the appropriate phase (red), RIN at 200 kHz (red bar) is narrowly suppressed by mode than 15 dB.

In this feed forward scheme, the intensity noise can be suppressed around the target frequency with narrow bandwidth, and at other frequency range, the intensity noise becomes worse because the noise is positively feedback at theses frequency range. The intensity noise spectra of the demodulated frequency discrimination signal is shown in Fig.5.13. The intensity noise at free-running state (blue trace) is suppressed and is suppressed down to 5 dB at 1 Hz (red trace), which are measured by an FFT analyzer (ADVANTEST Inc. R9211). The noise suppression ratio of the demodulated signal is smaller than that of the intensity noise under the feedforward control, which comes from the leak of the 200 kHz signal from the function generator that drives EOM, whose 200 kHz peak is appeared in the RIN under the feedforwad control.

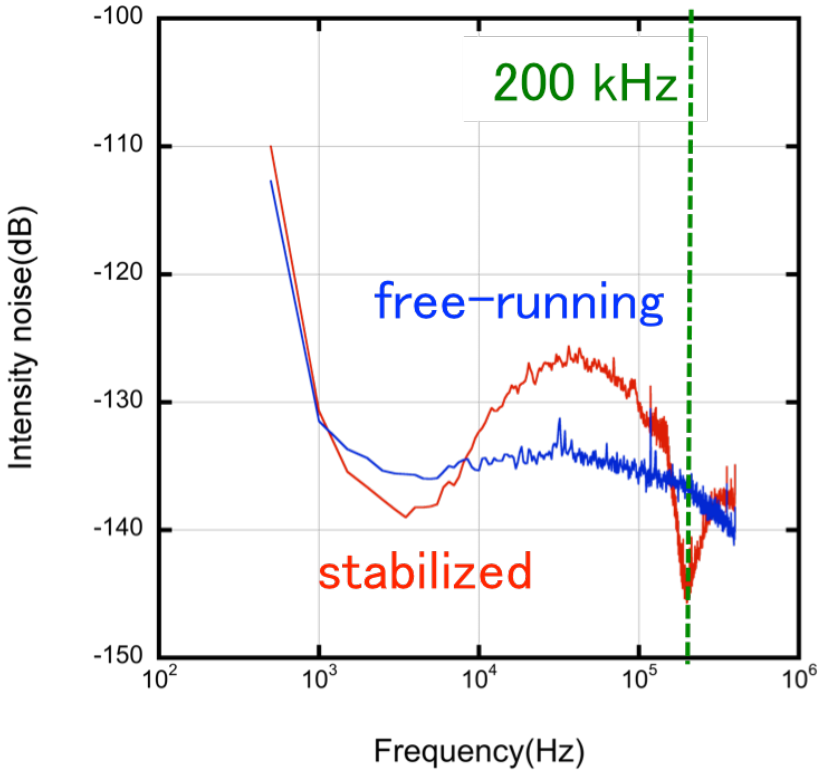

Figure 5.13. Intensity noise spectra in the demodulated frequency discrimination signal; blue and red indicate the intensity noise at the free-running and the stabilized state, respectively.

Since the demodulated intensity noise at 1 Hz is suppressed, the SNR of frequency discrimination signal is also improved with keeping the signal strength. The expanded frequency discrimination signals are shown in Fig.5.14 and Fig.5.15, which are measured by a digital oscilloscope (Iwatsu DS-5352). The yellow trace indicates the expanded demodulation signal, and the blue trace indicates the applied voltage to the PZT driver for the laser, which is proportional to the swept laser frequency.

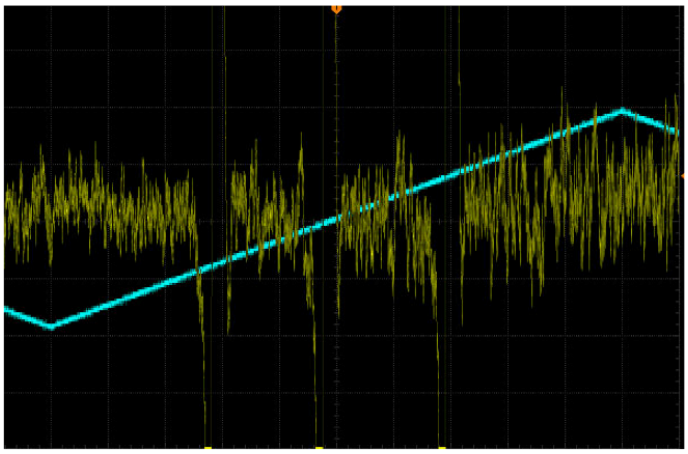

Figure 5.14. Expanded frequency discrimination signals at free-running state (yellow trace) Blue trace indicates the applied voltage to the PZT terminal of the laser.

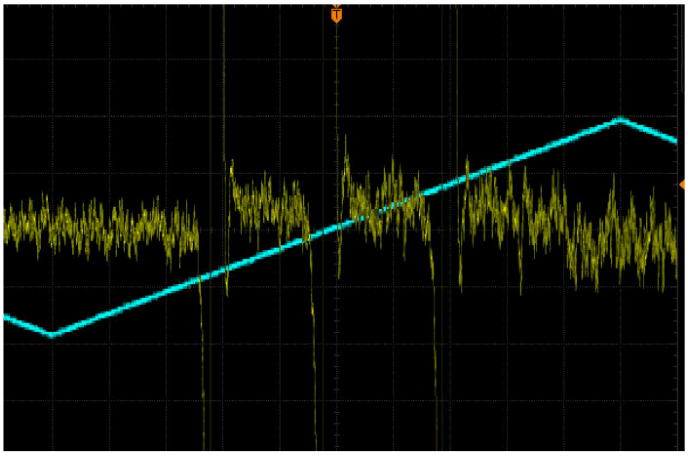

Figure 5.15. Expanded frequency discrimination signals at stabilized state

5.2 Balanced detection

In the subsection5.1, we have tried active intensity stabilization at 200 kHz, and the intensity noise at 200 kHz is suppressed by using active noise suppression methods. In this subsection, we try the passive intensity noise cancellation by using a balanced photo detector (PD), and improve the SNR of the frequency discrimination signals.

The principle of the intensity noise cancellation is that; since the intensity noise of the laser stays both beams before and after passing through the iodine cell and acts as a common mode noise, two detected beams are subtracted electrically to cancel the laser intensity noise components from the detection signal, and the SNR of the demodulated frequency discrimination signal would be improved. Fig.5.16 shows the schematic of our passive intensity noise cancellation system.

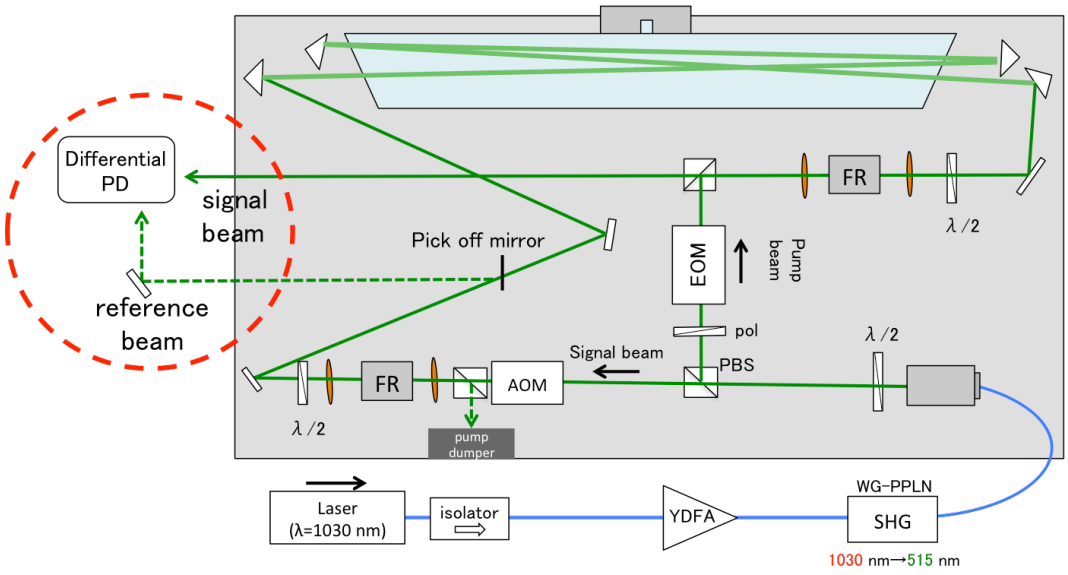

Figure 5.16. Schematic of the passive intensity noise cancellation system

The beams before and after passing through the iodine cell, which are picked off by a beam sampler, are called the reference beam and the signal beam, respectively. Each beam are detected by separate photo detectors in our hand-made differential PD, and photocurrent from each photo detectors

are directly subtracted. For maximizing noise canceling effects, the DC power balance of the two detected signals should be severely identical. Therefore auto DC balance mechanism is installed in our balanced detector, which is called an auto-balanced differential PD based on ref.[77]. The configuration of the electrical circuit is attached in Appendix E.

First, we tested the characteristic of the auto-balanced detector. Fig.5.17 shows the intensity noise spectrum obtained from the output of the auto-balanced detector, where the input power to the signal PD is 0.5 mW. The red trace indicates the detected intensity noise spectrum without reference beam input (free-running). For working auto-balance system properly, the power of the local beam should higher than that of the signal PD.

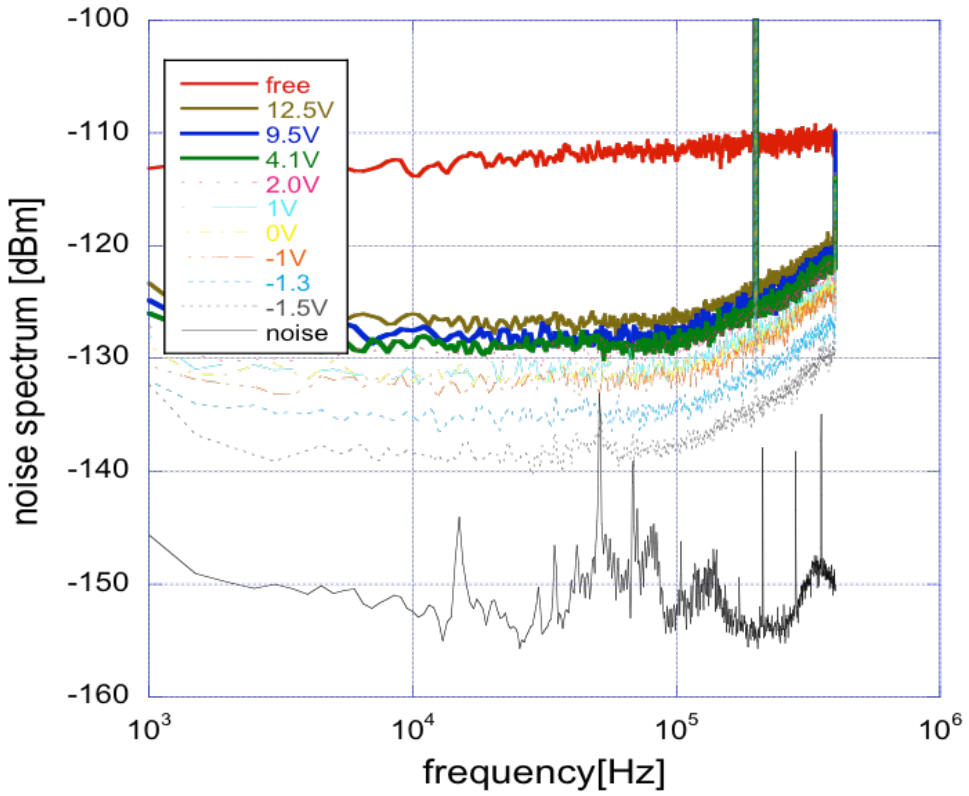

Figure 5.17. Intensity noise spectrum obtained from the auto-balanced PD with various local powers. As the local power increases (V_{mon} decreases), the noise suppression ratio increases up to 25 dB.

As the power of the reference beam increases, the monitor voltage, V_{mon}, decreases from 15 V. Seen from Fig.5.17, the intensity noise spectrum is suppressed as the local power increase (V_{mon} decreases), and the noise suppression reaches 25 dB when the V_{mon} is -1.5 V. In Fig.5.17, the intensity noises are detected at the laser frequency is off-resonance to the iodine.
When the laser frequency is tuned at on resonance of the iodine, the noise suppression ratio decrease, which is shown in Fig.5.18. The noise spectrum from the auto-balanced PD without local beam (black trace), local in with off resonance (blur trace), and local in with on resonance (red trace).

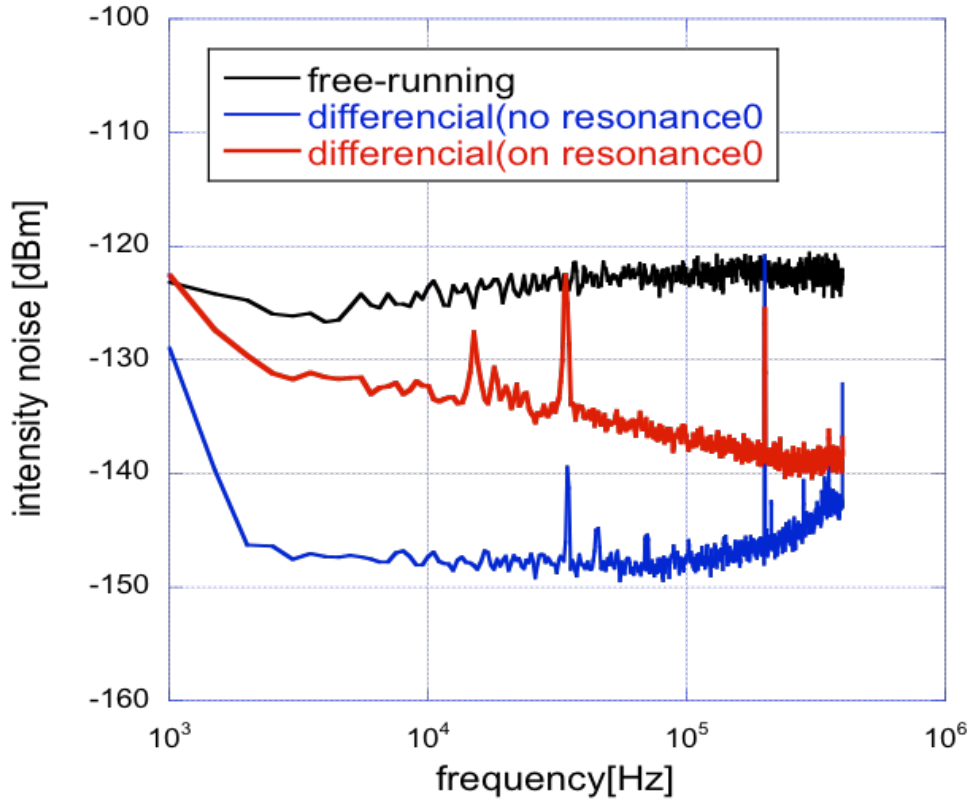

Figure 5.18. Noise spectrum from the auto-balanced PD without local beam (black trace), local in with off resonance (blur trace), and local in with on resonance (red trace)

It is considered that the noise from fluorescence is added to the signal beam, which results in decreasing noise suppression effect.

5.2.1 Experimental result of balanced detection

The noise spectrum of the demodulated signal from the auto-balanced PD are shown in Fig.5.19. The noise level of the demodulated signal from the single PD (blue trace) is improved at the all the frequency range by 10 dB (red trace), whose suppression ratio is little bit lower than that of the balanced-detected RIN in Fig.5.18, and signal to noise ratio of the discrimination signal improves.

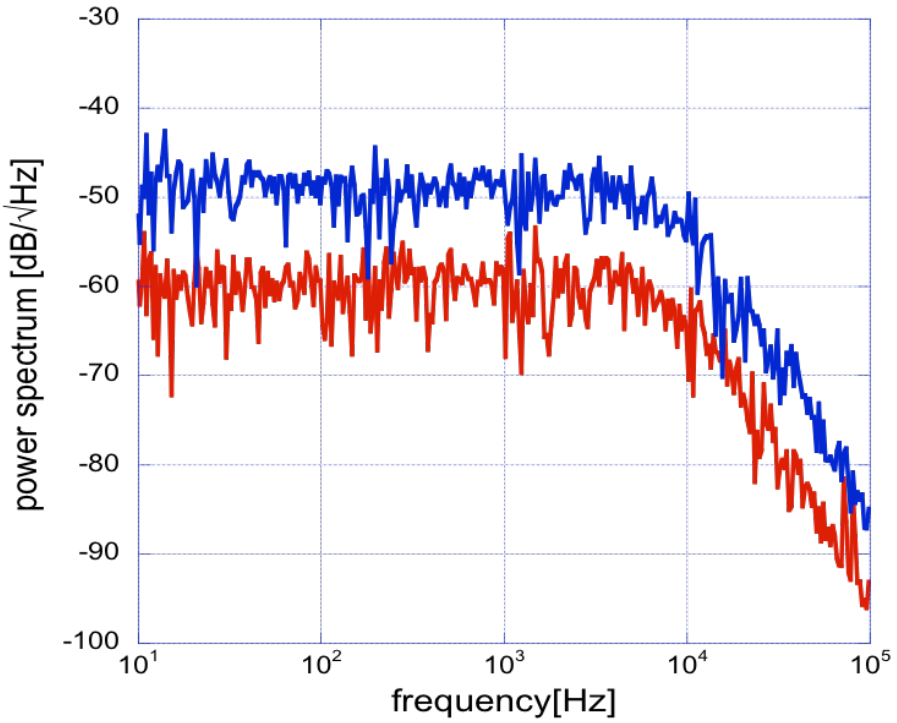

Figure 5.19. Demodulated signal from the single PD (blue) and from the auto-balanced PD

Finally we evaluated the improvement of the frequency stability of the iodine-stabilized lasers. Fig. 5.20 shows the absolute frequency noise evaluated from the beat note between two lasers, details of which are described in section 4.4 . The frequency of two lasers are locked to the same saturated absorption line of I_2, and the frequency noise spectrum from the single PD (blue trace) at lower frequency range is improved by using the auto-balanced

PD (red trace), and reaches 1.7x10^1 $Hz/\sqrt{Hz}$ below 200 Hz. Assuming that both BBMs are the same frequency stability in frequency stabilizing operation, the frequency stability of each laser is smaller by $1/\sqrt{2}$, and the absolute frequency stability of both lasers is estimated to reach 1.2x10^1 $Hz/\sqrt{Hz}$ below 200 Hz. As conclusions, we stabilized frequency of the laser in reference to the iodine saturated absorption, and the short term frequency stability of 12 $Hz/\sqrt{Hz}$ is obtained in both BBMs below 200 Hz by improving the SNR of the frequency discrimination signal. This frequency noise level is worse than that of the requirement for DECIGO by 1 order. RIN of the laser at the modulation frequency still far from the theoretical noise limit (shot-noise limit), and the frequency noise level of our laser would reach the requirement level of DECIGO by further suppressing the intensity noise at 200 kHz or replacing the laser with that which have low intrinsic intensity noise such as ECLD.

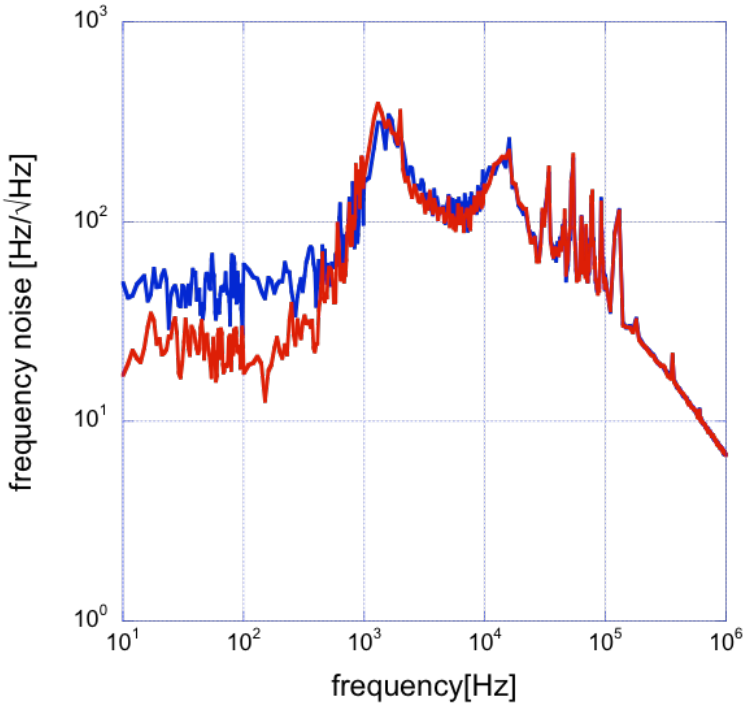

Figure 5.20. Frequency noise of the beat signal between two BBMs. By using the auto-balanced detector (red trace) the frequency noise is improved from the single PD detection (blue)

6 Intensity stabilization at observation band

In the case of a space GW detector such as DECIGO, the strain sensitivity of the interferometer at lower frequency is limited by the radiation pressure noise in which the light pressure from the laser fluctuates the test mass mirrors. Therefore laser power stabilization at the observation band around 1 Hz is necessary to improve the strain sensitivity of DECIGO, however, there are unknown noise below few hundred Hz which limits the intensity stability, and the intensity stabilization below few hundred Hz is extremely difficult [78]. Hence, the approaches for the unknown-noise suppression should be devised to improve the intensity stability at low frequency.

Fig.6.1 is the schematic of the light source of BBM. The light source consists of an Yb-doped fiber DFB laser and an Yb-doped fiber amplifier (YDFA), which is called Master Oscillator Fiber Power Amplifier (MOFPA) system. Therefore we have tried the intensity-stabilization of this MOFPA with negative feedback system, whose power actuator is a pump power of YDFA, because the intensity noise of MOPA system is dominated by that of a power amplifier which has been already investigated in our previous study.

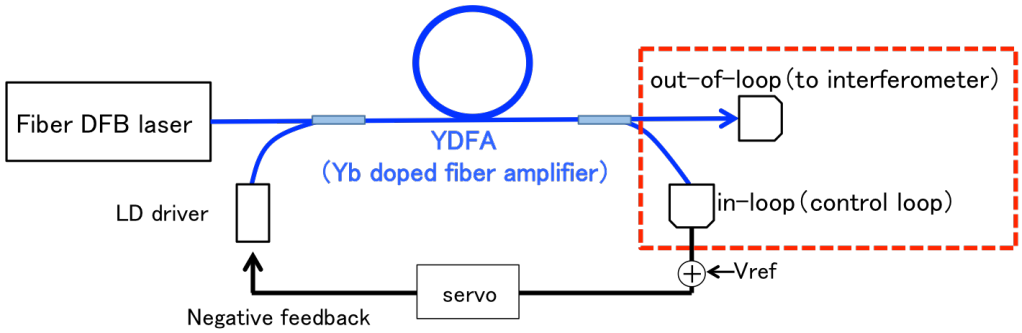

Figure 6.1. Schematic diagram of our intensity-stabilization system at the observation band around 1 Hz.

After the output power is amplified by YDFA, the amplified output is divided into two beams, one is used for intensity stabilization called in-loop (control loop) and the other is used for the main interferometer, and also for

evaluation of the out of loop. The voltage signal detected from an in-loop PD current is compared with the stable voltage reference, and the differential error signal is converted into error signal by a servo circuit. After filtered into the control signal, the error signal is applied into a modulation terminal of the LD driver. The in-loop intensity stability of the light source is evaluated from the error signal in the servo loop, and the out-of-loop intensity stability of the light source is evaluated by using the out-of-loop PD.

We have tried two approaches of how to divide a portion of the amplified beam (surrounded by red dashed square in Fig.6.1); by using a non-polarized beam splitter (NBS) in free-space, and by using an in-line fiber coupler. The former approach is called free-space experiment, and the latter is called fiber component experiment. In both approaches, the most critical point to improve the out-of-loop stability is the stabilization of the divided ratio of two beams, which are described in this section.
The open loop transfer function of the servo system consists of G (electrical servo filter) and A (the other part including optical part, optical to electric or reverse part), and described as $T_{open} = AG$. First, we measured the transfer function of the optical part A; from the modulation input of the LD driver to the PD detected voltage, and estimated the equivalent circuit of A. The transfer function A of simulated results from the equivalent circuit and measured are shown in Fig.6.2. The red traces and the blue traces indicate the characteristics of the gain (right) and phase(left), respectively. The solid and the dashed lines indicate the measured and simulated A, respectively. In this simulation, the equivalent circuit of A is identified as a quadratic integration circuit whose cutoff frequency is 3 kHz.

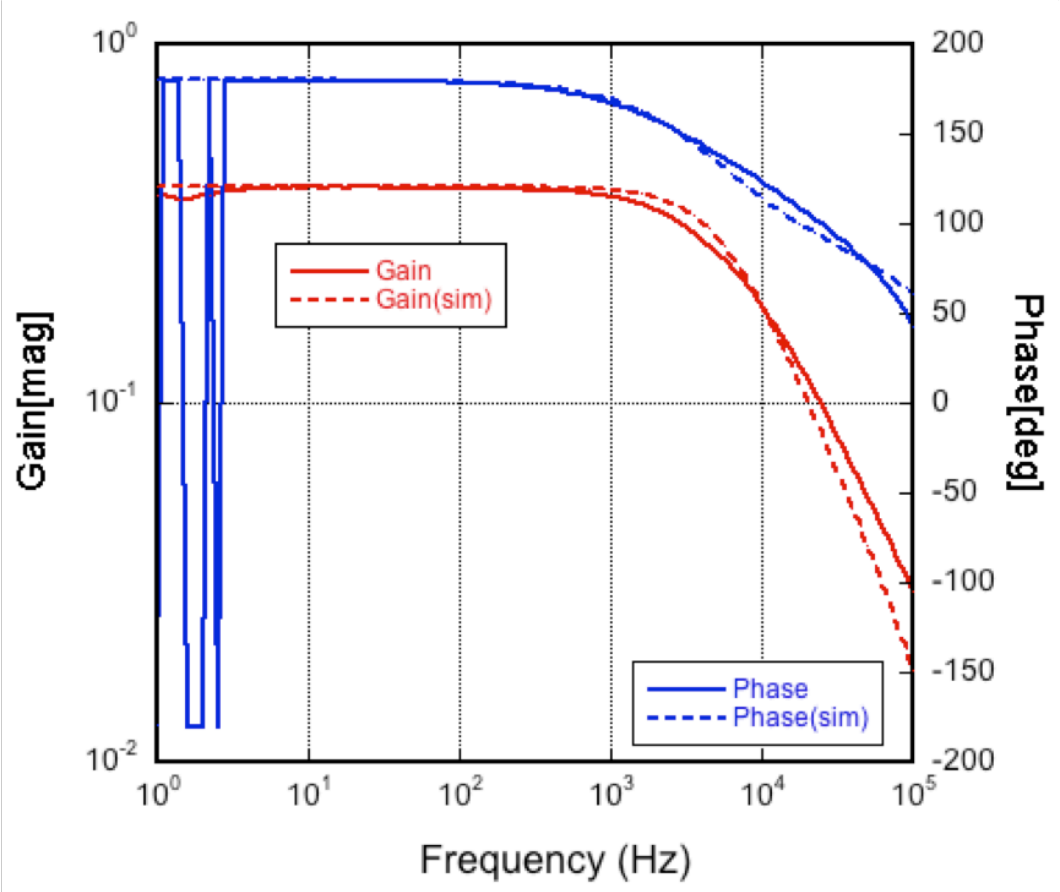

Figure 6.2. Transfer function of A (red: gain-left, blue: phase-right), measured (solid traces) and simulated by using equivalent circuit (dotted traces)

Total open loop transfer function of our servo system is simulated from the equivalent circuit (A) and the electrical servo filter (G) by using the electrical circuit simulator TINA, which is shown in Fig.6.3.
We obtained the gain of more than 140 dB at 1 Hz, and the control bandwidth of 20 kHz (unity gain frequency) which can be expanded up to 100 kHz by optimizing the servo gain, which is estimated from the total open loop transfer function $T_{open} = AG$. The servo circuit for the intensity stabilization is shown in Appendix F.

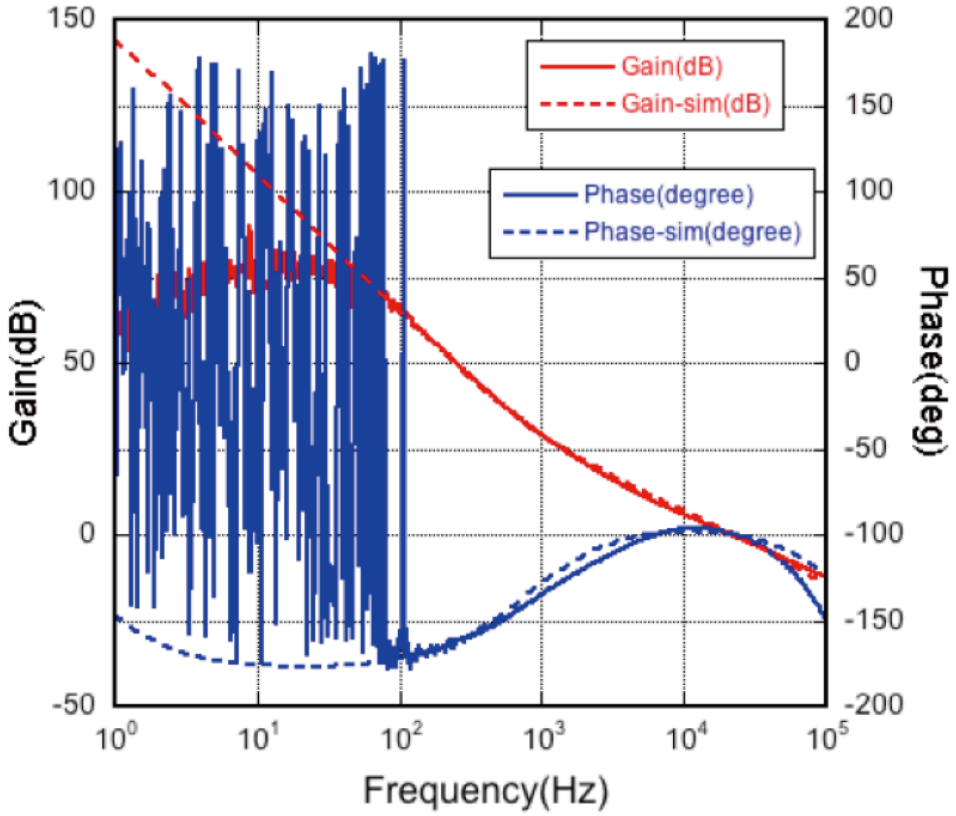

Figure 6.3. Total open loop transfer function $T_{open} = AG$

6.1 Free-space experiment

The amplified 1030-nm beam from YDFA is divided by using a 10 − dB fiber coupler and a small portion of the amplified beam extracted from a fiber collimator is passing through a polarizer (pol) and a 50:50 NBS to divide into the in-loop and the out-of-loop (shown in Fig.6.4). In order to make the photon shot noise reach $dI/I = 10^{-8}/\sqrt{Hz}$ level, the detected power of PDs should be more than 7 mW in all experiments. The photo diode used for PD is G12180-005A (Hamamatsu Photonics Inc.), and the thermal noise of the load resistance and PD dark current noise level is lower than that of the required shot noise level. We use LTC6655 (Linear Technology Inc.) as a stable voltage reference.

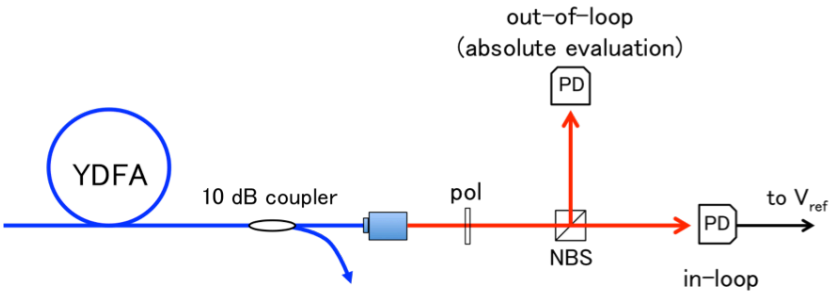

Figure 6.4. Experimental set up of the free-space intensity-stabilization by using NBS

Fig.6.5 is the relative intensity noise (RIN) evaluated from the in-loop (green line), that evaluated from the out-of-loop at free-running state (blue line), and that evaluated from the out-of-loop at stabilized state.

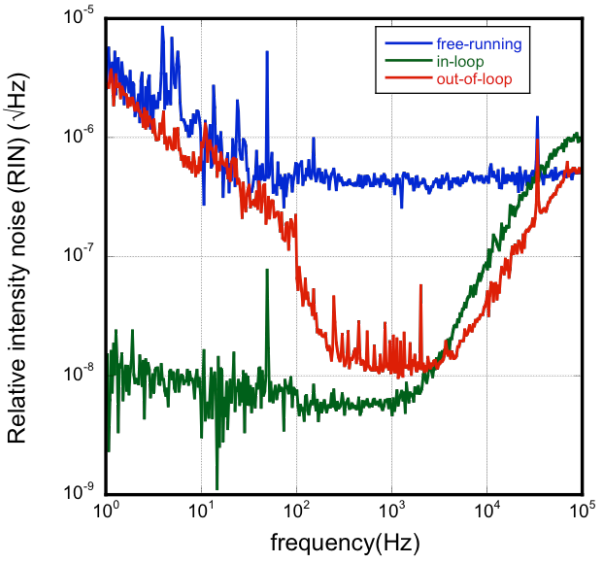

Figure 6.5. Intensity spectra of RIN at free-running state (blue trace), at the stabilized state evaluated from in-loop (green trace) and from out-of-loop (red trace)

The detected power at both in-loop and out-of-loop PDs are higher than 7 mW. The RIN evaluated from in-loop (in-loop RIN) is successfully suppressed down to $dI/I = 10^{-8}/\sqrt{Hz}$ level. However, the out-of-loop RIN at stabilized state is worse than that of the in-loop below 100 Hz, and reaches the level of that at free-running state at 1 Hz. In this experimental configuration, the divided ratio of NBS fluctuates, which comes from the coupling of polarization fluctuate of the amplified power and the polarization dependency of the NBS power divided ratio at 1030 nm.
The polarization dependency of the NBS transmittance is shown in Fig.refBSP. The transmittance of P-polarized light is 41 % and that of S-polarized light is 38 %. The reflectance of P-polarized light is 59 % and that of S-polarized light is 62 %, respectively.

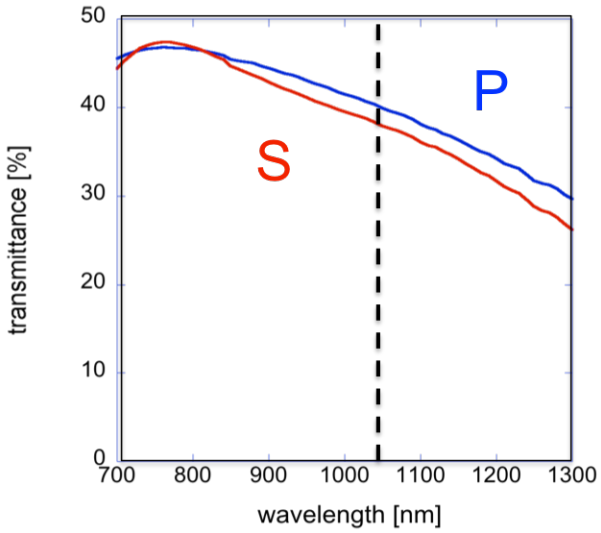

Figure 6.6. Polarization dependency of NBS (originated from the datasheet of Thorlab Inc

In order to improve the RIN evaluated from out-of-loop (out-of-loop RIN), the transmittance of the P-polarized light and the reflectance of the S-polarized light at NBS should be identical. The polarization dependency of NBS reflectivity is reduced by tilting NBS (Fig.6.7) so as to have the same transmittance of the P-polarized light and S-polarized light, (50 : 50),

which improves the out-of-loop intensity stability (Fig.6.8). The purple line indicates the out-of-loop intensity stability which is improved by tilting the NBS. In this way, the RIN below 100 Hz is suppressed, and we obtain the out-of-loop stability of $dI/I = 1.4 \times 10^{-7}/\sqrt{Hz}$. The RIN at 1 Hz is limited by the stability of the voltage reference, which is shown in Fig.6.8.

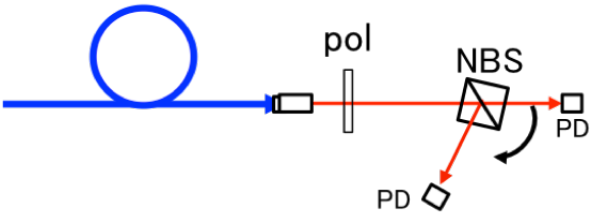

Figure 6.7. Tilting the incident angle of NBS to have equal reflectance for both p and s polarized light

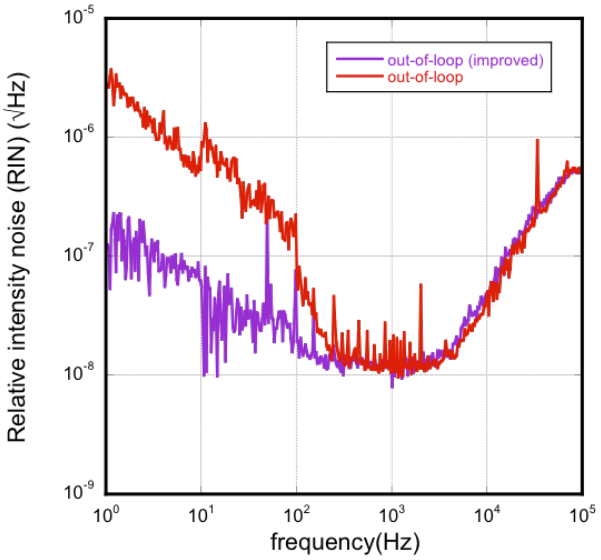

Figure 6.8. Out-of-loop RIN at free-space experiment ; red line: before improving , purple line: improved by tilting NBS

6.2 Fiber components experiment

We also tried to divide a portion of the amplified power into 50:50 by using a 3 dB-fiber coupler. Fig.6.9 is the schematic of the fiber components experiment. The amplified beam is divided by a 10-dB fiber coupler, and a portion of the beam is additionally divided into in-loop beam and out-of-loop beam by using a 3-dB fiber coupler. Two beams are detected by two PDs directly to avoid from a contaminant of a stray light.

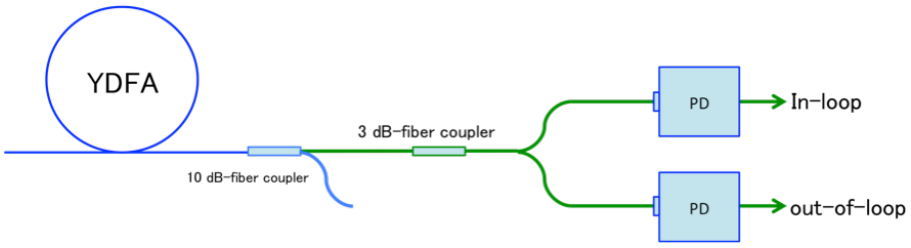

Figure 6.9. Schematic of the intensity stabilization by using a 3-dB fiber coupler

At first, all the fiber components in this configuration are fixed by using ordinary adhesive tapes. However, these adhesive tapes fix fibers insufficiently and the fibers are vibrating slightly by acoustic oscillation and seismic vibrations from the ground. These fiber vibrations give slight and differential optical loss to the fibers, and cause the degradation of the out-of-loop stability (Fig.6.11).
It might be difficult to suppress the acoustic oscillation and seismic vibration completely. However, if they give the same perturbations to both in-loop and out of-loop fibers, the out-of-loop excess intensity noise can be cancelled as a common mode noise applied to both fibers in the intensity-stabilization process. As a next step, we try to fix whole 3-dB fiber coupler by using epoxy resin and the divided beams are directly coupled to two PDs, which is shown in Fig.6.10. In Fig.6.11., the black line indicates the power spectrum of RIN evaluated from the in-loop, the red line indicates that evaluated from the out-of-loop (not fixed), the blue line indicates that evaluated from out-of-loop (fixed by epoxy resin), the dashed purple line indicates the stability of the voltage reference (LTC6655).

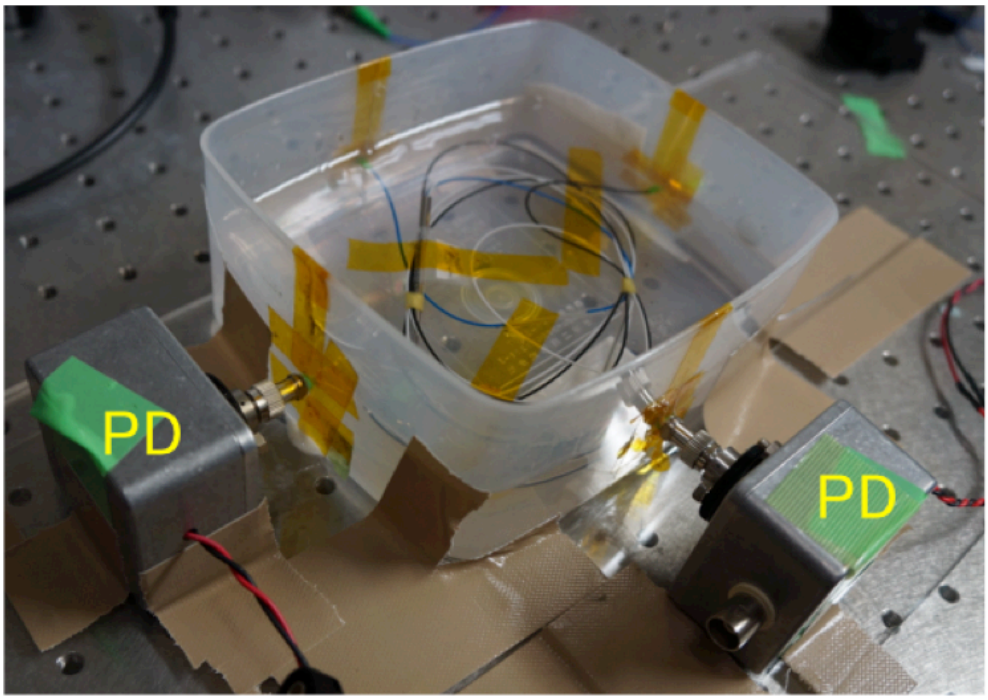

Figure 6.10. Picture of the intensity stabilization by using a 3-dB fiber coupler

This experimental result shows that the vibration of the fibers is successfully suppressed which caused from that the external perturbations act as the common mode to different fiber tails and the excess differential noise is completely cancelled, and the RIN evaluated from out-of-loop below 100 Hz is dramatically improved. We obtain the RIN of $dI/I = 1.2 \times 10^{-7}/\sqrt{Hz}$ at 1 Hz which is equal to the stability of the voltage reference.

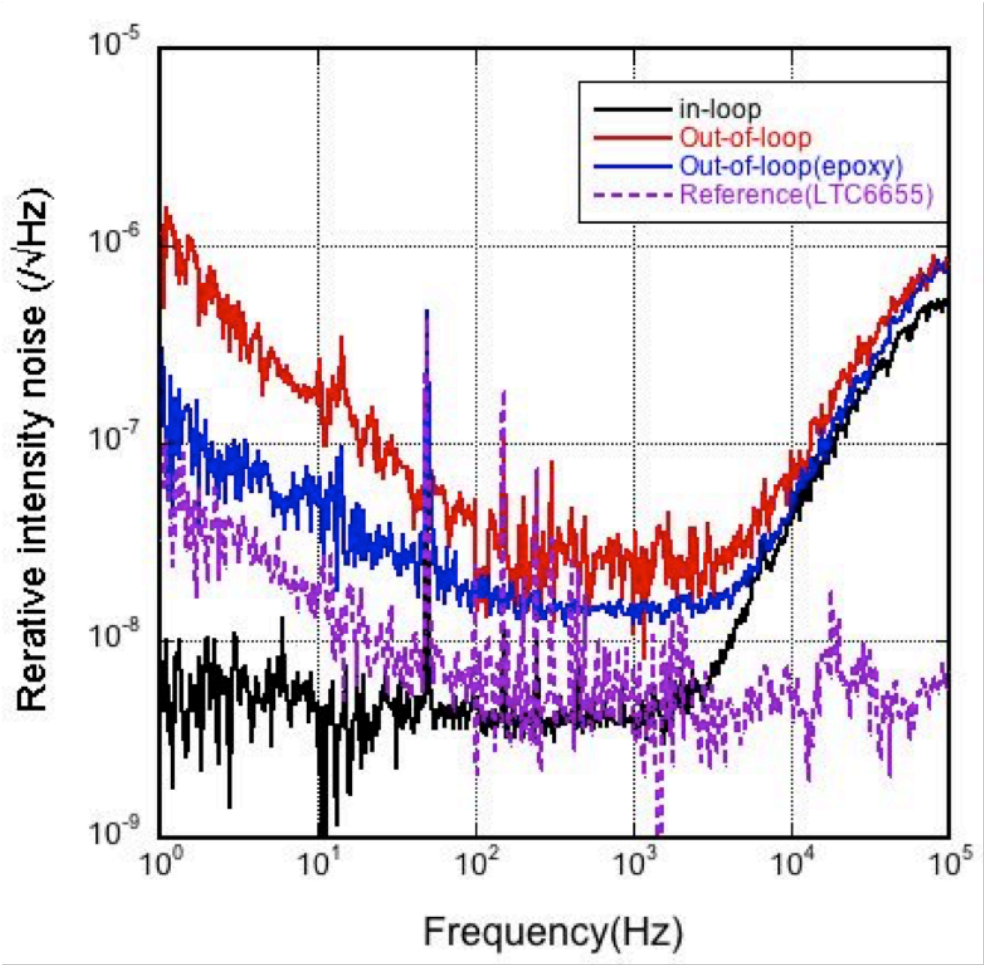

Figure 6.11. RIN spectra obtained from fiber components experiments; the black line indicates the RIN evaluated from in-loop, the red line indicates that evaluated from out-of-loop (not fixed), the blue line indicates that evaluated from out-of-loop (fixed by epoxy), the dashed purple line indicates the stability of the voltage reference (LTC6655)

Finally, we try further improvement in the fiber components experiment. In this experimental setup (see Fig.6.12), the vibrations to the different fibers become common mode noise, however the vibrations itself are also suppressed by covering all the optical components concerning the intensity stabilization with polystyrene box and by putting a 5-kg aluminum board as a weight on the box, which suppresses the vibration of this setup and protect from acoustic oscillation and the temperature variations.

In order to improve the RIN at 1 Hz, the voltage reference is replaced to more stable voltage reference. These trials improve the out-of-loop RIN at 1 Hz (shown in Fig.6.13). The blue line indicates the RIN evaluated from the in-loop, and the red line indicates the out-of-loop, which is improved. The out-of-loop RIN between 100 Hz and 1 kHz is limited by the photon shot noise level, and between 10 Hz and 100 Hz is limited by the noise from the vibration, at 1 Hz is limited from the stability of the voltage reference.

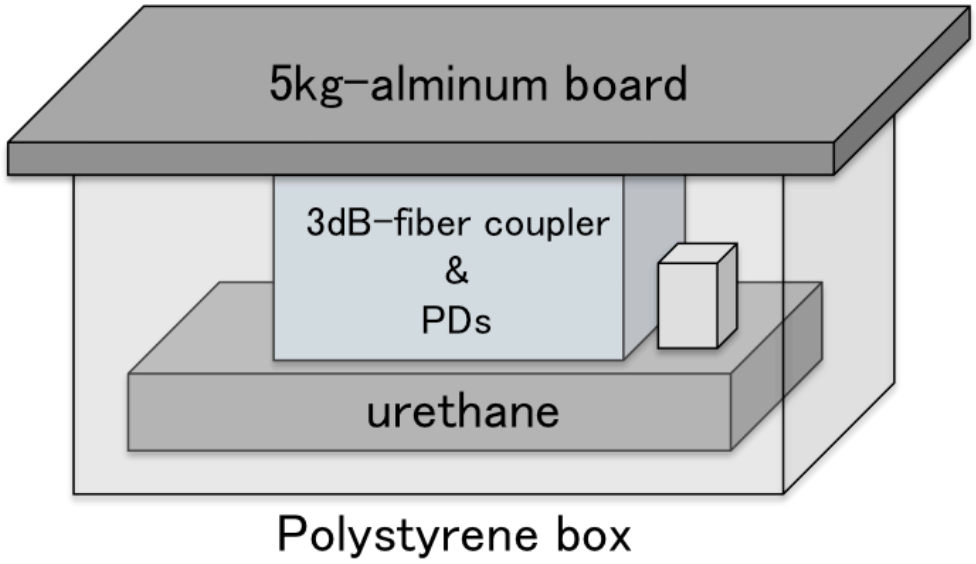

Figure 6.12. Schematic of the experimental setup which is covered by a polystyrene box, and a 5 kg-aluminum board is put as a weight on the box.

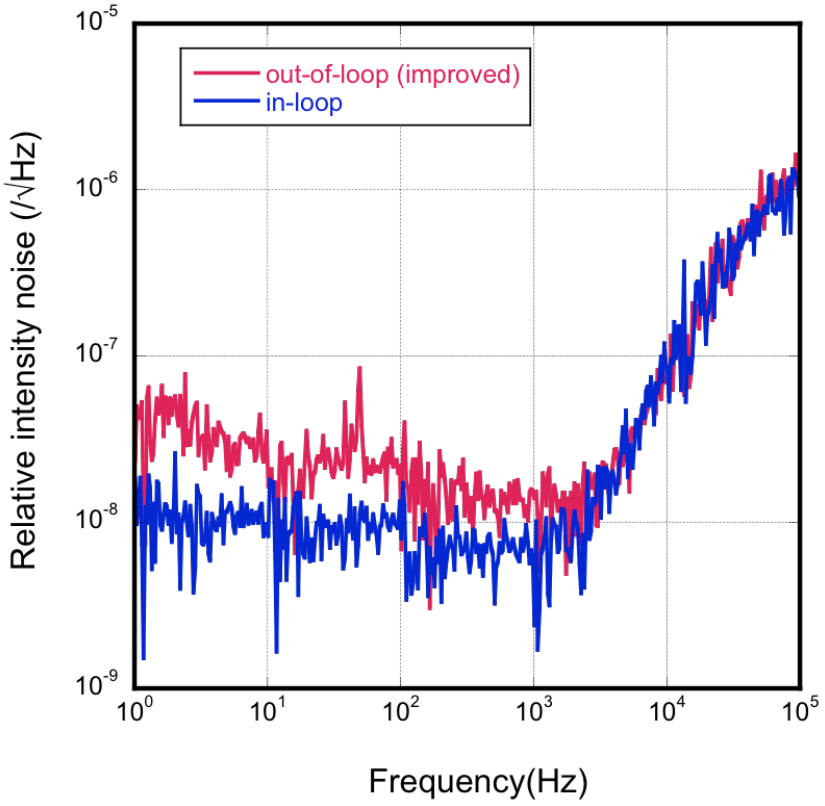

Figure 6.13. Improved RIN spectra obtained from the fiber components experiments. The blue line: the RIN evaluated from the in-loop, the red line: the RIN evaluated from out-of-loop whose experimental setup is covered by the box, and whose voltage reference is replaced to more stable reference.

Highly intensity stabilization of the lasers has been studied by terrestrial gravitation wave detection groups around 1 kHz ([79], [80]). However, the intensity stabilization at lower frequency range is much difficult because at lower frequency range, the intensity noise of the out-of-loop laser output is very sensitive to the external perturbations, and hard to reach highly intensity stabilized level in out-of-loop evaluation. We successfully suppress the out-of-loop intensity noise to $10^{-8}/\sqrt{Hz}$ level which is lowest record at around 1 Hz. As the next step, we should try to stabilized intensity noise of 515 nm green light for DECIGO.

7 Further improvement of frequency stability

We have tried frequency stabilization and intensity stabilization at 200 kHz in the section 4-5, and obtain the short-term frequency stability of df =13 $Hz/\sqrt{Hz}$. In order to improve the short-term frequency stability, we have managed to detect higher SNR frequency reference by using new signal detection method. In addition to the modulation transfer (MT) technique, frequency modulation (FM) technique at higher phase modulation is also installed to the signal detection method. Fig.7.1 is the schematic diagram of the experimental setup for the improvement of the short-term frequency stability.

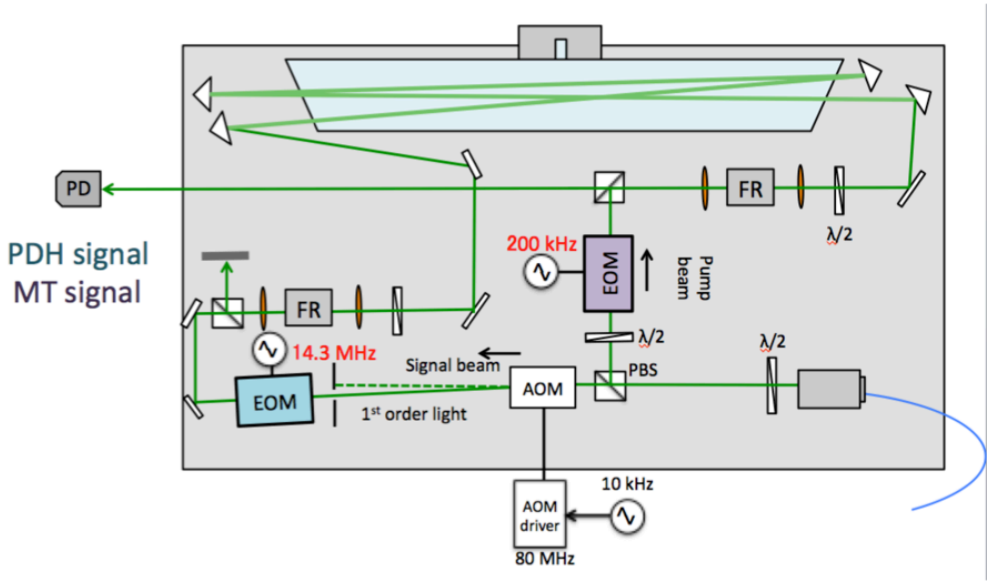

Figure 7.1. Experimental setup for the combination of FM and MT

In addition to the phase modulation of the pump beam at 200 kHz, the signal beam is directly phase-modulated at 14.3 MHz by using the additional EOM (blue rectangle), and the intensity-modulated at 10 kHz by using AOM. In this setup, both offset-free MT signal and PDH signal can be obtained.

Fig.7.2 shows MT and PDH signal which are detected synchronously. The characteristics of two signals; since MT signal is offset-free signal, it has good long-term stability, but due to low SNR comes from the intensity

noise at 200 kHz, the short-term stability is not so good. On the other hand, since PDH signal is phase-modulated at higher frequency where the intensity noise of the laser falls to near the shot-noise-limited level, the demodulated signal has better SNRwhich would result in the good short-term stability. However, PDH signal is not offset-free signal, the long-term stability is not good which comes from DC offset drift. Therefore, the frequency of the laser is stabilized in reference to both signals by using nested servo loop, and the laser stability follows PDH signal at lower frequency range and MT signal at lower frequency range.

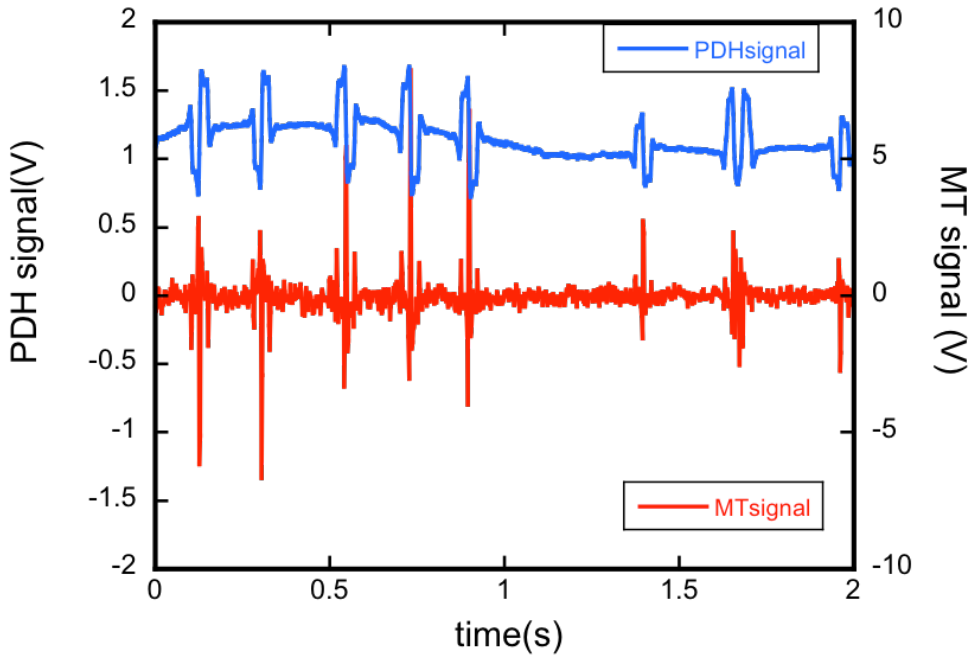

Figure 7.2. Frequency discrimination signals obtained from MT technic and FM technic which are detected synchronously

8 Conclusion

We have developed the iodine-stabilized lasers as a light source for Japanese space gravitational wave detector:DECIGO, and whose frequency is stabilized in reference to the iodine saturated absorption signal at 515 nm. Since the short-term frequency stability of the iodine-stabilized laser is worse than that of the cavity-stabilized laser, both the long-term stability and the short-term stability of iodine-stabilized laser have not been pursued. Our work is the first trial to realize the long-term and the short-term stability of the iodine-stabilized laser.

In order to select narrower linewidth to improve the short-term frequency stability of the iodine-stabilized laser, we have developed a new precision spectroscopy system based on frequency-stabilized laser and AOM, and confirm that the linewidth at 515 nm of iodine saturated absorption signal is narrower than that at 532 nm, and the condition of the pressure-broadening effect. We have developed two breadboard models (BBM1, BBM2) of the iodine-stabilized laser in which the compactness, high efficiency, mechanical stability and robustness are taken into considerations as a space-born laser. The frequency stability of two BBMs are evaluated from the error signal (in-loop), and obtain the frequency stability of higher than 1 $Hz/\sqrt{Hz}$ at 1 Hz in both BBMs, which satisfies the required level of DECIGO.

The absolute frequency stability of our frequency-stabilized lasers are evaluated from the beat note between them, and the absolute frequency stability of df =30 $Hz/\sqrt{Hz}$ is obtained from frequency spectrum at 1 Hz. Since we use lock-in detection method to obtain the frequency reference, the short-term frequency stability is limited by the modulation frequency of 200 kHz. Therefore we try the intensity stabilization at 200 kHz by using active and passive intensity-stabilization. By the feed forward intensity stabilization and auto-balanced detection, the frequency stability of two BBMs are improved to 12 $Hz/\sqrt{Hz}$ at 1 Hz. After applying the residual amplitude modulation (RAM) control to EOM, the long-term frequency stability of the lasers are also improved and the frequency stability of $df/f = 10^{-14}$ level over 2000 s, which is evaluated from Allan-deviation. Compared with other groups, the long-term frequency stability is worse than that in [49], which comes from RAM

effect and the interference noise from scattering. And short-term frequency stability of our lasers is comparable with that of [53]. In order to improve the strain sensitivity of the DECIGO, the intensity noise at observation band is also stabilized in the free-space experiment and the fiber-components experiment. RIN at 1 Hz is suppressed down to $\Delta I/I = 1.4 \times 10^{-7}/\sqrt{Hz}$ and $\Delta I/I = 5 \times 10^{-8}/\sqrt{Hz}$ from the free-space experiments and fiber-components experiment, respectively.

9 Future prospects

Further improvements of the frequency stability and the intensity stability are required to operate as a light source for DECIGO.
The short-term frequency stability might be improved by following trials; (i) frequency modulation method, whose modulation frequency is higher than 10 MHz and the intensity noise reaches shot-noise limited level, would improve SNR of the frequency reference and the short-term frequency reference. However, the offset of the signal obtained from frequency modulation degrading the long-term frequency stability. Therefore, now we try to detect frequency modulation signal and modulation transfer signal simultaneously from one BBM, and the laser frequency is stabilized from both signal with nested servo loop (ii) The light source is replaced with a lab-made external-cavity laser diode (ECLD) at 1030 nm whose intensity noise at 200 kHz is much lower than that of the currently-used Yb-fiber DFB laser. The long-term frequency stability should be improved by the active control of RAM by applying DC voltage to EOM crystal. These trials are now under developed to realize the frequency stability of $df/f = 10^{-15}$.
The intensity noise stabilization at 1 Hz obtained from the fiber-components experiment which I described in this paper can be applied to the relatively low-power fiber-coupled light source as the light source for B-DECIGO. However, further intensity stability obtained from the free-space experiments is required for high power source for DECIGO whose required power is 10 W. In order to improve the intensity stability of the free-space experiments, the voltage reference should be replace with more stable voltage reference and differential noise between in-loop and out-of-loop should be suppressed. In addition to them, the intensity noise of high-power green light at 515 nm should be evaluated.
The combination of the fiber power amplifier and coherent addition system is now under developed in our laboratory. In our previous study, it is found that a few tens W class high power light source in MOPA configuration keeps the frequency stability of the maser laser.

In my paper, the frequency and intensity stabilization for the space-borne

laser is reported. For realizing DECIGO project, we have developed many key technologies whose difficulty should be overcome. Though, my laser cannot reach the requirement level of DECIGO, the highest short-term frequency stability is obtained as the iodine-stabilized laser, and, I hope, my those trials can be applied to other space project or precision measurement before DECIGO will be launched at mid 2030s.

appendix

A The investigation of breadboards for BBM

As a candidate of breadboard used for BBMs, a carbon breadboard is considered. Michelson interferometers are installed on both carbon and conventional aluminum breadboards and the variations of the interference fringe on each Michelson interferometers are measured to compere the distortion of 2 breadboards.
The picture of the breadboards which is used for this experiment are shown in Fig.A.1 and Fig.A.2, and size and weight are listed in Table 4

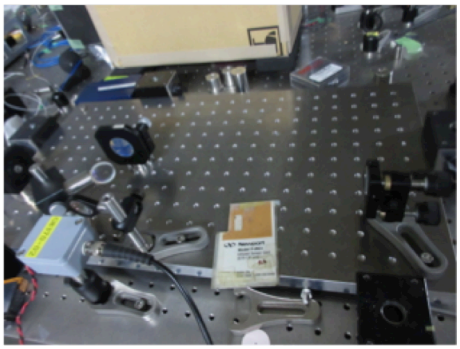

Figure A.1. Aluminum breadboard

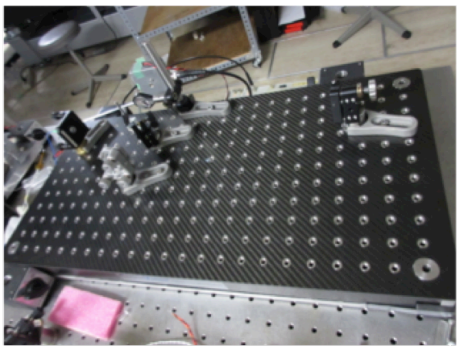

Figure A.2. Carbon breadboard

Table 4: Carbon and aluminum breadboards

Material of breadboard	size [mm]	Weight [kg]
Aluminum	$550 \times 200 \times 20$	8.7
Carbon	$600 \times 300 \times 60$	5.3

As mentioned in Table 4, the carbon breadboard is lighter than the aluminum breadboard since the carbon breadboard is honeycomb structure.
The schematic of the asymmetric Michelson interferometers installed on each breadboard is shown in Fig.A.3.

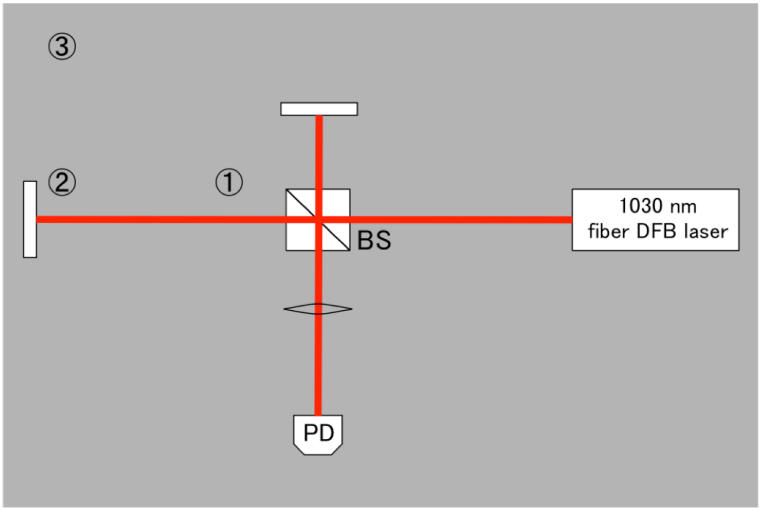

Figure A.3. Experimental setup of the asymmetric Michelson interferometer

A load by the 1.98-kg copper weight is applied to each breadboards on the point 1 3 in Fig.A.3 for a few seconds.

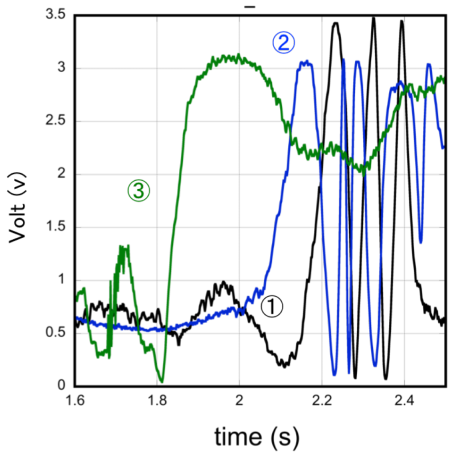

Figure A.4. Temporal variations of the interference fringe (aluminum breadboard)

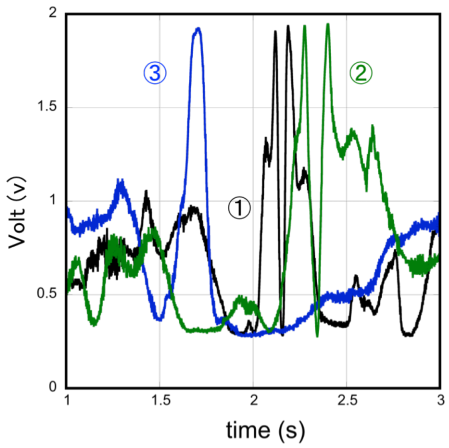

Figure A.5. Temporal variations of the interference fringe (carbon breadboard)

Seen as Fig.A.4 and Fig.A.5, the distortion is appeared by the copper weight on both breadboards, and the temporal variations of the interference fringe are measured. In both breadboards, in the case of point 1 or 2, the variations of the interference fringe is lager than that of point 3 because the

point 1 or 2 is near the arm of the interferometer. In point 1, the variations are 3λ and $2/3\lambda$ in the aluminum breadboard and the carbon breadboard, respectively. Therefore, the relative variations $\Delta L/L$ are 5.2×10^{-5} (aluminum breadboard) and 2.6×10^{-6} (carbon breadboard), and the distortion of the carbon breadboard is approximately half than that of aluminum breadboard. I also measure the variations of the interference fringe which is caused from the thermal expansion of the breadboard and the thermal linear expansion coefficients are determined. In the experimental setup of Fig.A.6, each breadboards are heated by the ribbon heater, and the ribbon heater is covered by aluminum foil to avoid the disturbance of air.

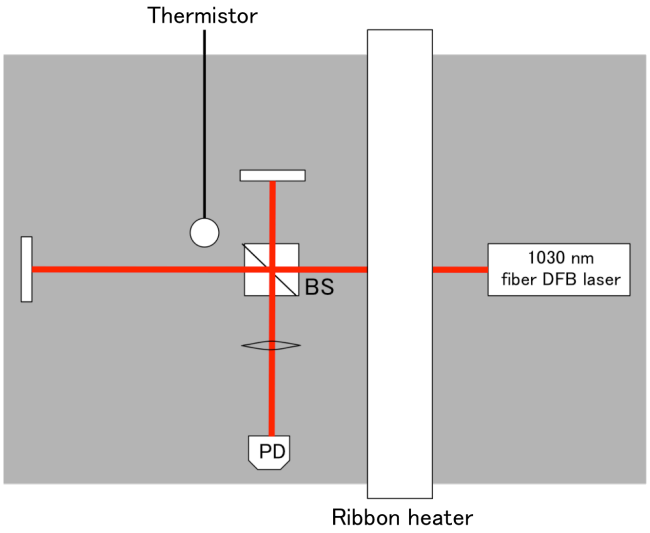

Figure A.6. Experimental setup of the asymmetric Michelson interferometer heated by the ribbon heater

The temporal variations of the interference fringe and the thermistor resistance are synchronously remoted. The experimental results are shown in Fig.A.7 and Fig.A.8.

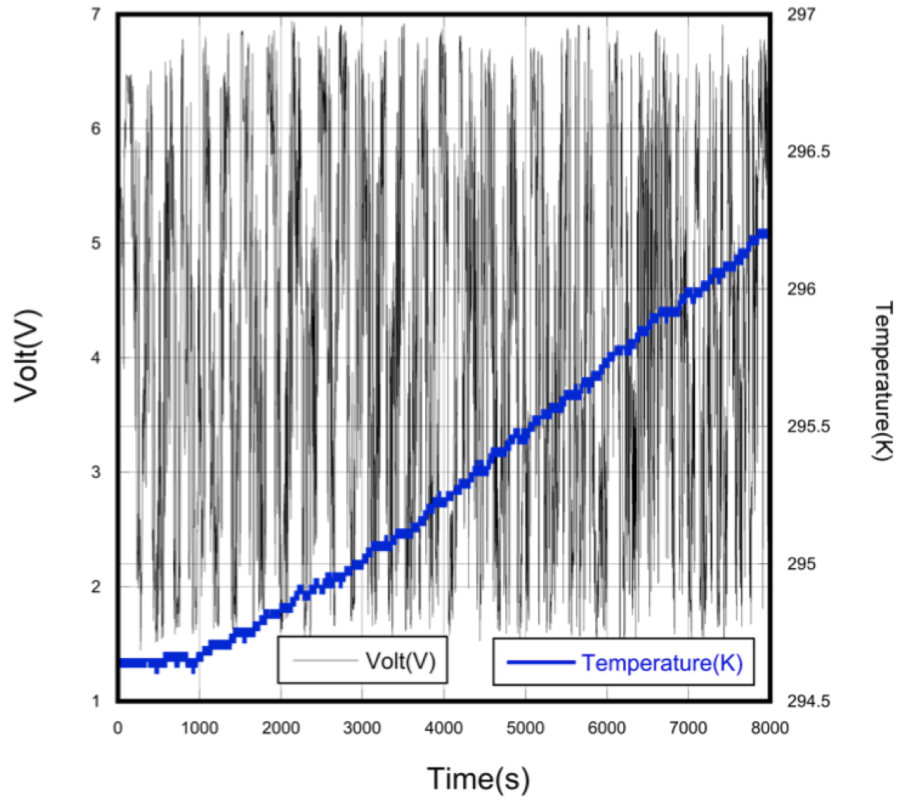

Figure A.7. Thermal variations of the interference fringe (aluminum breadboard)

As is the case in previous experiments, the relative variations $\Delta L/L$, and the thermal linear expansion coefficients $\Delta L/L/K$ from the variations of the interference fringe and the thermal variations. The linear expansion coefficients $\Delta L/L/K$ of the aluminum breadboard and the carbon breadboard are 23.9×10^{-6}[1/K] and 8.6×10^{-6}[1/K], respectively. Since the measured linear expansion coefficients of the aluminum breadboard is almost same as previous work [81].

It is demonstrated that the carbon breadboard has lower distortion and the thermal expansion than the aluminum breadboard, and the potential candidate for a next-generation BBM or EM.

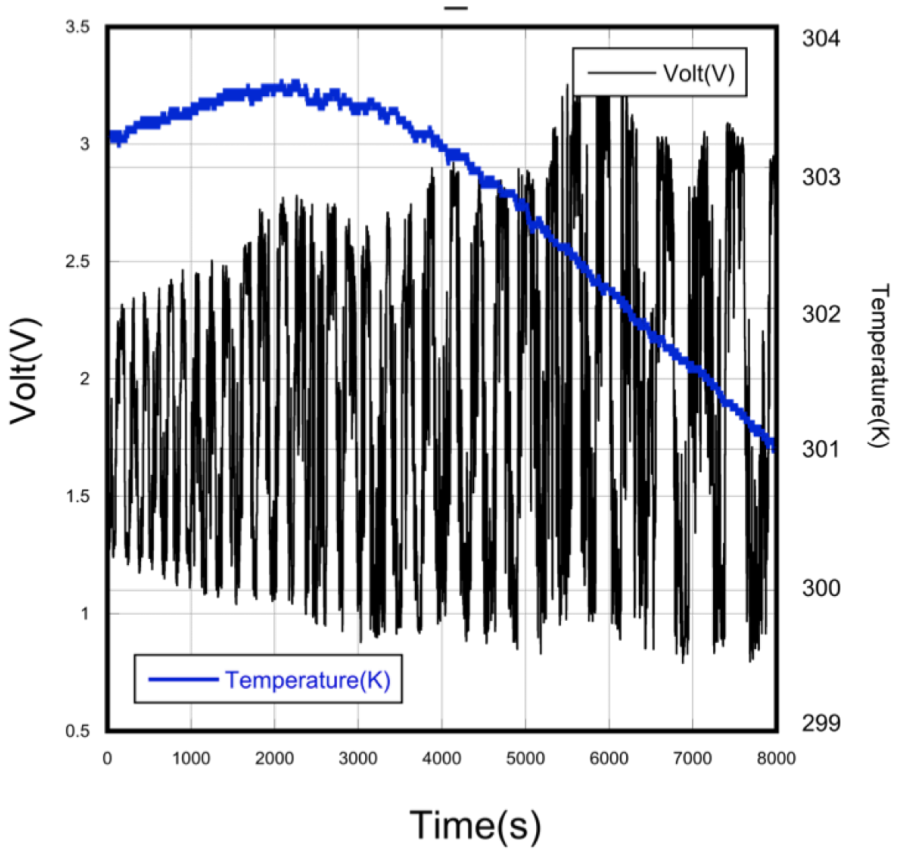

Figure A.8. Thermal variations of the interference fringe (carbon breadboard)

B Servo circuit for the frequency stabilization

A: equivalent circuit of optical part

G: electrical servo filter

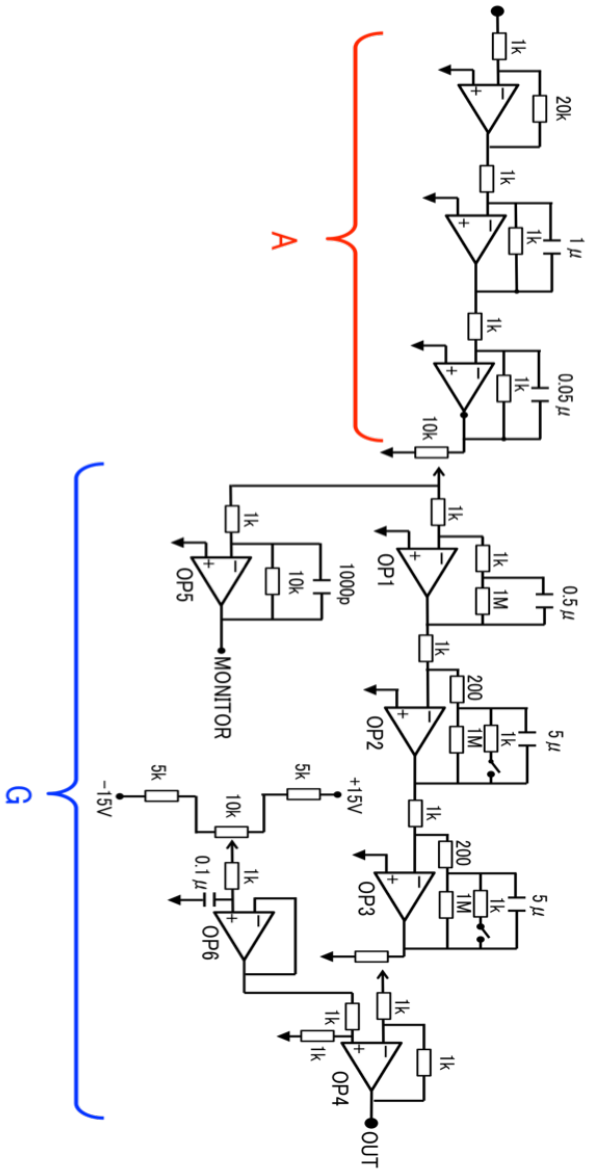

C Servo circuit for intensity stabilization at 200 kHz by using normal feedback

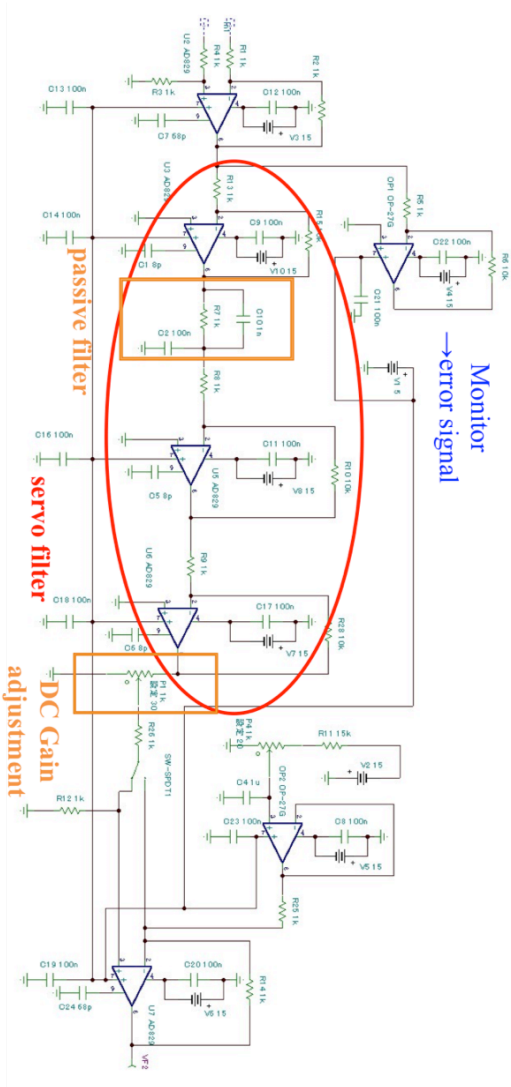

D Phase shifter of the feedforward servo for intensity stabilization at 200 kHz

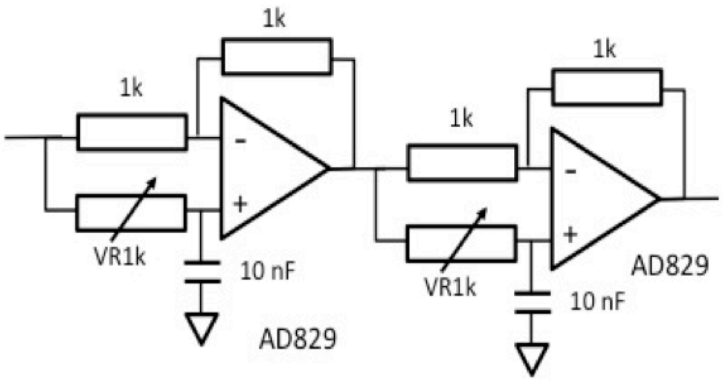

E Electrical circuit of the auto-balanced detector

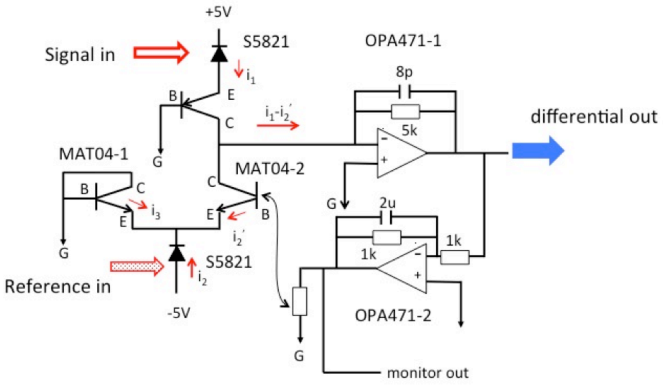

Figure E.1. Electrical circuit of the auto-balanced detector

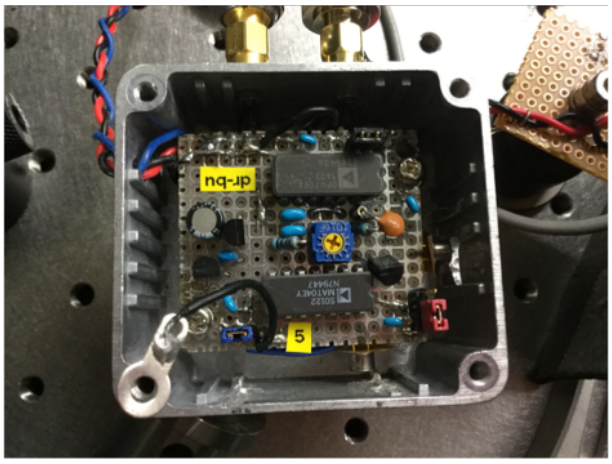

Figure E.2. The picture of the auto-balanced detector

F Electric servo filter for the intensity stabilization of the laser at 1 Hz

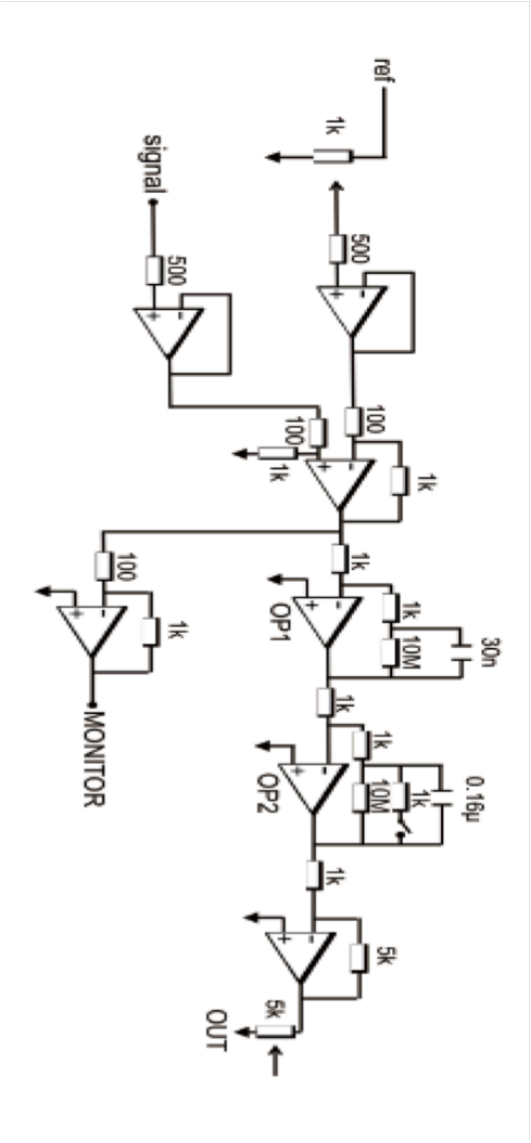

References

[1] G.R.Hanes, K.M.Baird and J.DeRemigis ‘ Stability, Reproducibility, and Absolute Wavelength of a 633-nm He – Ne Laser Stabilized to an Iodine Hyperfine Component ’ , Appl. Opt. vol.12, pp.1600 (1973)

[2] T.Baer, F.V.Kowalski, and J.L.Hall ‘ Frequency stabilization of a 0.633-¨ µ m He-Ne longitudinal Zeeman laser ’ Appl. Opt., Vol.19, pp.3173-3177 (1980)

[3] K.Nakagawa and A.Onae ‘ Development of an acetylene optical frequency standard at 1.5 µ m and its applications ”, Proc. SPIE vol.4269, pp.41 (2001)

[4] M.Eickhoff and J.L.Hall ‘ Optical frequency standard at 532 nm ’ IEEE Trans. Meas. Vol.44, pp.155 (1995)

[5] A. Arie and R.L.Byer ‘ Frequency stabilization of the 1064-nm Nd:YAG lasers to Doppler-broadened lines of iodine ’ Appl.Optics vol.32, pp.7382 (1993)

[6] F-.L. Hong et.al ‘ Portable I_2-stabilized Nd:YAG laser for international comparisons ’ , IEEE Trns. Instrum. Meas, vol.50, pp.486 (2001)

[7] S. Haefner et.al ‘ $8\times10-17$ fractional laser frequency instability with a long room-temperature cavity ’ Opt. Lett. Vol.40. pp.2112 (2015)

[8] I.Ushijima, M.Takamoto M.Das, T.Ohkubo and H.Katori ‘ Cryogenic optical lattice clocks ’ Nature Photonics, vol.9, pp.185 (2015)

[9] J-P. Uzan ‘ The fundamental constants and their variation: observational and theoretical status ’ Rev. Modern Physics, vol.75, pp.403 (2003)

[10] Y.Michimura etr.al ‘ Optical cavity limits on high order Lorentz invariance ’ , Phys. Rev.D vol.88. pp.111101 ® (2013)

[11] M.E.Gertsenshtein, V.I.Pustovoit ‘ On the detection of low frequency gravitational waves ’ J. Experimental Theoretical Physics. 43, pp.605 – 607 (1962)

[12] M.Musha, K.Nakagawa and K.Ueda ‘ Wideband and high frequency stabilization of an injection-locked Nd:YAG laser to a high-finesse Fabry-Perot cavity ’ Opt.Lett vol.22, pp.1177 (1999)

[13] M.Musha et.al ‘ Measurement of frequency noise spectra of frequency-stabilized LD-pumped Nd:YAG laser by using a cavity with separately suspended mirrors ’ Opt. Comun., Vol.140, pp.323-330 (1997)

[14] M.Musha et.al ‘ Intensity and frequency noise characteristics of two coherently-added injection-locked Nd:YAG lasers ’ Appl. Phys B. vol.73, pp.209-214 (2001)

[15] K.Arai et.al ‘ Recent progress of TAMA300 ’ J.Physics: Conference series, vol.120, pp.032010 (2008)

[16] Yoichi Aso et.al ‘ Interferometer design of the KAGRA gravitational wave detector’ Phys. Rev. Lett. vol.88, pp.043007 (2013)

[17] N.Seto, S.Kawamura and T.Nakamura ’ Possibility of direct measurement of the acceleration of the universe using 0.1 Hz band laser interferometer gravitational wave antenna in space ’ , Phys.Rev.Lett. vol.87,pp.221103 (2001)

[18] A.Einstein ‘ Die Grundlage der allgemeinen Relativit ä tstheorie ’ Annalen der Physik ’ vol.49, pp.769-822 (1916)

[19] ME Gertsenshtein ‘ Wave resonance of light and gravitional waves ’ Sov Phys JETP,Vol.14, pp.84 (1962)

[20] A.Weinstein ‘ Advanced LIGO optical configuration and prototyping effort ’ Class. Quantum. Grav., vol.19, pp.1575-1585 (2002)

[21] F.Acernese, P.Amico, M.Alshourbagy et.al. ‘ The Virgo 3 km interferometer for gravitational wave detection ’ J. Opt. A, vol.10, pp.064009 (2008)

[22] J.Hough et.al ‘ GEO600 ’ Max-Planc fur Quantumphysik Technical Report No.VIR-0517A-15 (1989)

[23] S.Miyoki‘ Development of a 100-meter Delay-Line Laser Interferometer ’ University of Tokyo Ph.D Thesis (1996)

[24] B.P.Abbott et.al. ‘ Observation of Gravitational Waves from a Binary Black Hole Merger ’ Phys. Rev. Lett. vol.116, pp.061102 (2016)

[25] B.P.Abbott et.al. ‘ GW151226: Observation of Gravitational Waves from a 22-Solar-Mass Binary Black Hole Coalescence ’ Phys. Rev. Lett. vol.116, pp.24113 (2016)

[26] B.P.Abbott et.al. ‘ GW170104: Observation of a 50-Solar-Mass Binary Black Hole Coalescence at redshift of 0.2 ’ Phys. Rev. Lett. vol.118, pp.221101 (2017)

[27] B.P. Abbott et al. ‘ A Three-Detector Observation of Gravitational Waves from a Binary Black Hole Coalescence ’ Phys. Rev. Lett. vol.119, pp.110411

[28] B.P.Abbott et.al ‘ GW170817: Observation of Gravitational waves from a binary neutron star inspiral ’Phys. Rev.Lett. vol.119, pp.161101 (2017)

[29] Kuroda, K., et.al.: The status of LCGT. Class. Quantum. Grav., vol.23, S215-S221 (2006)

[30] A.Sesana, J.gair, I.mandel, A.vecchio Ap.J., Vol.693 L129-L132 (2009)

[31] T.L.Smith et.al Phys. Rev. D vol.79, pp.103501 (2009)

[32] P.Amaro-Seoane et.al. ‘ Low-frequency gravitational-wave science with eLISA/NGO ’ Class. Quantum. Grav. vol.29, pp.124016 (2012)

[33] Shuichi Sato1, Seiji Kawamura, Masaki Ando, Takashi Nakamura, Kimio Tsubono, Akito Araya, Ikkoh Funaki, Kunihito Ioka, Nobuyuki Kanda, Shigenori Moriwaki ‘ The status of DECIGO ’ J.Phys., Vol.840 pp.012010

[34] M.Musha, DECIGO working group ‘ Space gravitational wave antenna DECIGO and B-DECIGO ’ Spacej.Vol.9 pp.371-377 (2017)

[35] M.Armano et.al. ‘ Sub-femto-g free fall for space-based gravitational wave observatories: LISA Pathfinder results ’ Phys. Rev. Lett. vol.116, pp.231101 (2016)

[36] W.Kokuyama ‘ Spaceborne rotating torsion-bar antenna for low-frequency gravitational-wave observations ’ Dissertation of Ph.D thesis, Department of Physics, University of Tokyo (2012)

[37] M.Ando, S.Kawamura, N.Seto et.al ‘ DECIGO pathfinder ’ Class. Quantum Grav. vol.26, pp.094019 (2009)

[38] A.Suemasa. M.Musha ‘ Highly frequency-stabilized laser for space gravitational wave detector DECIGO/DPF ’ Proceeding of ICSO 2014, Tenerife Spain (2014)

[39] S.Kawamura, et.al. ‘ The Japanese space gravitational wave antenna DECIGO ’ Class Quantum Gravity vol.28, pp.094011 (2011)

[40] S.Kuroyanagi, T.Chiba, N.Sugiyama ‘ Precision calculations of the gravitational wave background spectrum from inflation. Phys. Rev. D vol.79, pp.103501 (2009)

[41] T.Nakamura, et.al. ‘ Pre-DECIGO can get the smoking gun to decide the astrophysical or cosmological origin of GW150914-like binary black holes ’ Prog. Theory Exp. Phys. 2016, 093E01

[42] V.Leonhardt et.al. ‘ Laser frequency stabilization to molecular resonances for TPF-C, LISA, MAXIM ’ Proc.SPIE 6265 (2006)

[43] T.Leveque et al ‘ A laser setup for rubidium cooling dedicated to space applications ’ Appl. Phys B. vol.116, pp.997 (2014)

[44] B.Argence, et.al. ‘ Prototype of an ultra-stable optical cavity for space applications ’ Opt. Exp. vol.20, pp.25409-25420 (2012)

[45] 中村卓史、三尾典克、大橋正健 ‘ 重力波をとらえる ’ 京都大学学術出版会，第 6 章 (1998)

[46] T.Akutsu ‘ The internal report of DECIGO working group ’ (Sep.2012)

[47] S.O.Rice ‘ Mathematical analysis of random noise ’ Bell system Tech. J., vol.23, pp.46 (1945)

[48] V.Leonhardt, B.Camp ‘ Space interferometry application of laser frequency stabilization with molecular iodine ’ Appl. Opt., Vol.45, pp.4142-4146, (2006)

[49] Thilo Schuldt et.al., ‘ Development of a compact optical absolute frequency reference for space with 10 − 15 instability ’ Appl. Opt., Vol.56, pp.1101-1106 (2017)

[50] Katrin Dahl et.al. ‘ A New Laser Technology for LISA ’ Proceeding of ICSO 2018, Creta Greek (2018)

[51] V.Schkolmik, K.doeringshoff, et.al. ‘ JOKARUS-design of a compact optical iodine frequency reference for a sounding rocket mission ’ EPJ.Quantum technology 4:9 (2017)

[52] Redfern Integrated Optics (RIO)-OptaSense Inc. HP, *http* : *//www.rio − lasers.com/_products/index.html*

[53] J. Barbarat et.al. ‘ Compact and Transportable Iodine Frequency-Stabilized Laser ’ Proceeding of ICSO 2018, Creta Greek (2018)

[54] W.R.Benett ‘ Hole-burning effect in a optical maser ’ Phys. Rev. Lett. Vol.126, pp.580 (1962)

[55] R.A.Macfaren, W.R.Benett, W.E.Lamb Jr. APL 2 pp.189 (1963)

[56] T.W.Haensche, M.D.Levenson, A.L.Schawlow, PRL 26, 946 (1971)

[57] G.C.bjorklund, and M.D.Levenson, M.Lenth, C.Ortiz ‘ Frequency Modulation (FM) Spectroscopy ’ Appl. Phys. B32, pp.145-152, (1983)

[58] J.L.Hall, L.Hollberg, T.Baer, and H.G.Robinson ‘ Optical Heterodyne saturation spectroscopy ’ Appl. Phys.Lett., Vol.39, pp.680-682 (1981)

[59] R.W.P.Drever, J.L.Hall, F.V.Kowalski, J.Hough, G.M.Ford, A.J.Munley, and H.Ward ‘ Laser phase and frequency stabilization using an optical resonator ’ Appl. Phys. B31, pp.97 (1983)

[60] R.V.Pound ‘ Electric frequency stabilization of microwave oscillators ’ Rev. Sci.I nstrum. 17, 490 (1946)

[61] Gary C. Bjorklund ‘ Frequency-modulation spectroscopy: a new method for measuring weak absorptions and dispersions ’ Opt. Lettl vol.5, pp.15-17 (1980)

[62] J.H.Shirley ‘ Modulation transfer processes in optical heterodyne saturation spectroscopy ’ Opt. Lettl vol.7, pp.537-539 (1982)

[63] E.Jaatinen ‘ Theoretical determination of maximum signal levels obtainable with modulation transfer spectroscopy ’ Opt. Commun. vol.120, pp.91-97 (1995)

[64] J.J. Snyder, R.K. Raj, D. Bloch, and M. Ducloy ‘ High-sensitivity nonlinear spectroscopy using a frequency-offset pump ’ Opt. Lettl vol.5, pp.163-165

[65] J.Vigué, M.Broyer, and J.C.Lehmann ‘ Ab Inutuo Calculation of Hyperfine and Magnetic Parameters in the I2 B State ’ Phys. Rev. Lett. Vol.42, pp.883-887 (1979)

[66] R.K. Raj, D. Bloch, J.J.Snyder et.al. ‘ High-Frequency Optically Heterodyned Saturation Spectroscopy Via Resonant Degenerate Four-Wave Mixing ’ Phys. Rev. Lett. Vol.44, pp.1251-1254, (1980)

[67] W.Cheng, L.Chen, T.H.Yoon, J.L.Hall, J.Ye ’ Sub-Doppler molecular-iodine transitions near the dissociation limit (523-498 nm) ‘ Opt. Lett. vol.27, pp.571-573 (2002)

[68] R.J.Jpnes, W.Cheng, K.W.Holman, L.Chen, J.L.Hall, J.Ye ‘ Absolute-frequency measurement of the iodine-based length standard at 514.67 nm ’ Appl. Opt. B 74, pp.597-601 (2002)

[69] T.J.Kane, A.C.Nilsson, R.L.Byer ‘ Momolithic unidirectional single-mode Nd:YAG ring laser ” Opt. Lett., vol.12, pp.175 (1987)

[70] W.Demtroeder ‘ Lase Spectroscopy forth edition ’ vol.2 pp.61 (Springer, Germany 2008)

[71] Atlas Du Spectre D ’Absorption de la Molecule D ’Iodine , CNRS (1985)

[72] S.Girard et.al.‘ Radiation hardening techniques for Er/Yb doped optical fibers and amplifiers for space application ’ Opt. Exp. vol.20, pp.8457-8465

[73] Y.Kobayasi, E.H.Sekiya, K.Saito, R.Nishimura, K.Ichii and T.Araki ‘ Effects of Ge co-doped radiation-induced absorption in Er/Yb-doped optical fibers for space applications ’ J. of Lightwave electron. vol.36, pp.2723-2729 (2018)

[74] NKT Photonics Inc.HP,$https : //www.nktphotonics.com/lasers - fibers/product/koheras-adjustik-low-noise-single-frequency-lasers/$

[75] Institute of Scientific Instruments, Czech Academy of Science HP, $https : //www.isibrno.cz/en/coherent - lasers - and - interferometry$

[76] Texas instrument Inc. HP, $http : //www.ti.com/tool/tina-ti?jktype = recommendedresults$

[77] P.C.D.Hobbs‘ Ultrasensitive laser measurements without tears ’Applied Optics vol.36, pp.903-920 (1997)

[78] Frank Seifert, Patrick Kwee, Michèle Heurs, Benno Willke, and Karsten Danzmann ’Laser power stabilization for second-generation gravitational wave detectors’ Opt. Lett., vol.31, pp.2000-2002 (2006)

[79] R.S.Abbott and P.J.King ’Diode -pumped Nd:YAG laser intensity noise suppression using a current shunt ”, Rev.of Scientific Instruments 72, pp. 1346-1349 (2001)

[80] P.Kwee, B.Willke and K.Danzmann ‘ Shot-noise-limited laser power stabilization with a high-power photodiodes array ’ , Opt. Lett. vol.34, pp. 2912-2914 (2009)

[81] National Astronomical Observatry (1992) 「Chronological Scientific Tables」 (Maruzen Co., Ltd.) pp.484